



**HAL**  
open science

# Development of dynamic MRI to study the musculoskeletal system during motion

Karim Makki

► **To cite this version:**

Karim Makki. Development of dynamic MRI to study the musculoskeletal system during motion. Image Processing [eess.IV]. Ecole nationale supérieure Mines-Télécom Atlantique, 2019. English. NNT : 2019IMTA0151 . tel-02414706

**HAL Id: tel-02414706**

**<https://theses.hal.science/tel-02414706>**

Submitted on 16 Dec 2019

**HAL** is a multi-disciplinary open access archive for the deposit and dissemination of scientific research documents, whether they are published or not. The documents may come from teaching and research institutions in France or abroad, or from public or private research centers.

L'archive ouverte pluridisciplinaire **HAL**, est destinée au dépôt et à la diffusion de documents scientifiques de niveau recherche, publiés ou non, émanant des établissements d'enseignement et de recherche français ou étrangers, des laboratoires publics ou privés.

# THESE DE DOCTORAT DE

L'ÉCOLE NATIONALE SUPERIEURE MINES-TELECOM ATLANTIQUE  
BRETAGNE PAYS DE LA LOIRE - IMT ATLANTIQUE  
COMUE UNIVERSITE BRETAGNE LOIRE

ECOLE DOCTORALE N° 601  
*Mathématiques et Sciences et Technologies  
de l'Information et de la Communication*  
Spécialité : *Signal, Image, Vision*

Par

**Karim MAKKI**

## **Développement de l'IRM dynamique pour l'étude de l'appareil musculo-squelettique en mouvement**

Thèse présentée et soutenue à Brest, le 04/10/2019  
Unité de recherche : LATIM U1101 INSERM  
Thèse N° : 2019IMTA0151

### **Rapporteurs avant soutenance :**

Marie-Odile Berger, Directrice de recherche, INRIA Villers les Nancy  
Vincent Noblet, Ingénieur de recherche, CNRS Illkirch

### **Composition du Jury :**

Président :	Antoine Nordez	Professeur, Université de Nantes
Examineurs :	Marie-Odile Berger Vincent Noblet Maxime Bourgain François Rousseau Douraid Ben Salem	Directrice de recherche, INRIA Ingénieur de recherche, CNRS Illkirch Enseignant-chercheur, EPF Sceaux Professeur, IMT Atlantique Professeur d'université, CHRU Brest
Dir. de thèse :	François Rousseau	Professeur, IMT Atlantique
Co-dir. de thèse :	Douraid Ben Salem	Professeur d'université, CHRU Brest



## Acknowledgments

I WOULD like to express my sincerest thanks and appreciation to all the members of the ITI department for welcoming me to this wonderful institution of higher learning. I have met many people inside and outside the work sphere that made the Ph.D an enjoyable adventure.

I am deeply grateful to my supervisors, Prof. François ROUSSEAU and Prof. Douraid BEN SALEM, for their invaluable advice, kindness, encouragements, patience and support during these three years. Their profound scientific knowledge, invaluable insight and experience have had a great impact on the success of the thesis. There is no doubt in my mind that without their comments, criticisms and guidance, my Phd will not be accomplished. I am also indebted to them for giving me the opportunity to improve my research background and experience. I am very lucky to have had the opportunity to work with them. It was always a pleasure to share an unforgettable moments rich with new results.

A special thanks to Dr. Bhushan BOROTIKAR, Prof. Sylvain BROCHARD, and Dr. Marc GARETIER for their efforts for subject recruitment and for data acquisition at the CHRU of Brest, and also for prolific discussions and interactions between the engineering and medical communities.

Furthermore, I also wish to thank the committee members, Prof. Marie-Odile BERGER, Dr. Vincent NOBLET, Prof. Antoine NORDEZ, and Dr. Maxime BOURGAIN for reviewing my thesis and enhancing my manuscript with their valuable comments.

I thank all my colleagues and friends who have accompanied me throughout my thesis, they made my life more enjoyable and less difficult in Brest. I warmly thank HASSENE, MUSAB and SALWAN for the precious advice and all the fruitful discussions. Thanks are due also to my wonderful officemates: CHI-HIEU, CARLOS, XIAOYU, EBTISSEM for the nice company and the good times.

Last but not least, the whole acknowledgment is dedicated to my family for their unlimited support, guidance and help. I am unable to count their graces and without them and their unselfish love, and kindness, and tenderness, and affection, I have not been come thus far and achieved my thesis. I would like to thank my wife INSAF for encouragement and love.



# List of Figures

1.1	Bones of ankle joint. Source: <a href="https://www.howtorelief.com/ankle-joint-anatomy-overview/">https://www.howtorelief.com/ankle-joint-anatomy-overview/</a> . . . . .	7
1.2	Medial ligaments and tendons of ankle joint. Source: <a href="https://www.memorangapp.com/flashcards/67023/012C+-+Lower+Limb/">https://www.memorangapp.com/flashcards/67023/012C+-+Lower+Limb/</a> . . . . .	8
1.3	Lateral ligaments and tendons of ankle joint. Source: <a href="https://www.memorangapp.com/flashcards/67023/012C+-+Lower+Limb/">https://www.memorangapp.com/flashcards/67023/012C+-+Lower+Limb/</a> . . . . .	9
1.4	Motion analysis laboratory at the CHRU Morvan and an example of a typical set-up for reflective marker placements on a healthy child. .	10
1.5	T1-FFE images of ankle joint during motion. The sequence is composed of 15 time frames, with a spatial resolution of $0.56 \times 0.56 \times 8mm$ .	13
1.6	Static VS dynamic MRI: the left image corresponds to the dense high-resolution static image, while the right image corresponds to a sparse low-resolution time frame from a T1-FFE dynamic MRI sequence. .	14
1.7	ODE integration: (a) a synthetic deformation field (velocity vector field) over a regular grid; example of a single clockwise rotation (rotation angle of $-50$ degrees around the origin), (b) infinitesimal displacement of one velocity vector ; in particular we have zoomed a single point trajectory between the source and target positions in order to show the temporal evolution of the associated velocity vector ( <i>i.e.</i> the elementary tangent vectors along the integral point trajectory).	19
	20figure.caption.11	
1.9	Example of screw motion through the z-axis. . . . .	22
1.10	Interpolation of smooth motions on $SE(3)$ : consistent interpolation of a simulated 3D rigid transformation $T$ that maps the blue ellipsoid (initial pose) to the red one (final pose), transformation parameters are: $t_i = 0mm$ , $t_j = 0mm$ , and $t_k = 0mm$ ; $r_i = 0^\circ$ , $r_j = 0^\circ$ , and $r_k = 30^\circ$ . 5 secondary rigid transformations $T^\alpha$ were interpolated between the identity and $T$ , giving a smooth trajectory of the rigid body between two poses in function of $\alpha$ ( $\alpha = \{n/6\}_{n \in \{1..5\}}$ in Eq 3.7).	23
2.1	Orthotic fixture specially designed to acquire MRI data on pediatric ankle joint. The entire fixture is made out of MRI-compatible material. Guide wires helped the technician to control and operate the passive plantar-dorsi flexion movements of the ankle joint while rest of the limb is fixed using straps at foot, tibia and mid thigh locations. Position of the ankle rest can be adjusted based on the limb length. Knee angle can be adjusted from full extension to $45^\circ$ flexion. Cushioned ankle rest supports the foot to be imaged. . . . .	36

2.2	Bones of interest: calcaneus (red), talus (green) and tibia (cyan). (a): Mid-sagittal image from the high-resolution static scan; (b): Mid-coronal image from the high-resolution static scan ; (c): Three dimensional rendering of segmented bones. . . . .	38
2.3	Proposed pipeline for ankle motion estimation: Bones of interest are segmented in the high-resolution static image. This high-resolution MR image is globally (and rigidly) registered to each MR image of the dynamic sequence (1.), and the position of each bone is refined thanks to a local rigid registration using bone segmentations (2.). This allows to identify the dynamic MR image which is closest to the high resolution image and which will serve as a starting point for the motion estimation within the dynamic sequence. Last, local and rigid registrations are conducted from the reference towards the sequence first and last images. . . . .	39
2.4	Anatomical coordinate systems for one subject's calcaneus (a), talus (b), and tibia(c) as per ISB. . . . .	41
2.5	Tracking of the tibia for one subject using Algorithm 1, only one out of two slices has been segmented in the static image ( <i>i.e.</i> , spatial resolution reduction). . . . .	44
2.6	3D normative kinematics of the calcaneal-tibial complex using the proposed image processing method. The kinematics of the calcaneus are represented relative to the tibial coordinate system defined in neutral position. Average rotation and translation were computed for both passive and active motion for the studied ankles. Standard deviation above and below the average line are shown (dotted shaded area for passive motion and green shaded area for active motion). . .	47
2.7	3D normative kinematics of the talocrural (talar-tibial) joint using the proposed image processing method. The kinematics of the talus are represented relative to the tibial coordinate system in neutral position. Average rotation and translation were computed for both passive and active motion for the studied ankles. Standard deviation above and below the average line are shown (dotted shaded area for passive motion and green shaded area for active motion). . . . .	48
2.8	3D normative kinematics of the subtalar joint using the proposed image processing method. The kinematics of the calcaneus are represented relative to the talar coordinate system in neutral position. Average rotation and translation were computed for both passive and active motion for the studied ankles. Standard deviation above and below the average line are shown (dotted shaded area for passive motion and green shaded area for active motion). . . . .	49

2.9	3D DICE coefficients between manual and automatic bone segmentation maps for the six subjects of the pilot study taking account of the whole set of bone trajectories. Results for passive (left column) and active motion (right column) are separated. A dice value of 1 indicates perfect geometric alignment between automatic and ground truth segmentations. . . . .	50
2.10	Temporal evolution of the root-mean-square error (RMSE in voxels) between manual and automatic bone segmentations for studied ankles. Errors are represented using error bars. The average is shown with a dotted line with one standard deviation above and below this line. Results for passive (left column) and active motion (right column) are separated. . . . .	51
2.11	High-resolution temporal reconstruction of the ankle joint for one subject (subject 6: passive motion). First row: original dynamic images, second row: corresponding high-resolution reconstructed images, downsampled to resemble to the original low-resolution images in order to validate the reconstruction accuracy. Each column corresponds to one time frame. Contours of the first time frame show the reconstruction accuracy (column 1) and the joint motion (columns 2 to 4). . . . .	52
2.12	Jacobian map of the joint deformation field that maps $D_1$ to $D_2$ for subject 4. The Jacobian determinant $J(x)$ at a voxel $x$ measures how the voxel volume changes after the diffeomorphic registration. It indicates a volume increase if $> 1$ , and a volume decrease if $< 1$ . The Jacobian determinant is equal to 1 inside bone segmentations (indicating no voxel volume changes) as bones only perform linear rigid transformations (rotations and translations). . . . .	53
3.1	sInteractive sequences: these sequences are very sensitive to motion artifacts which may lead to misregistration when using intensity-based algorithms. . . . .	58
3.2	Movie clear sequences: these sequences are less sensitive to motion artifacts and thus are more suitable for intensity-based methods despite the presence of noise. . . . .	59
3.3	Joint forward-tracking. From up to down, from left to right: $D_1$ , $D_4$ , $D_6$ , $D_9$ , $D_{12}$ , and $D_{14}$ . Individual bone segmentation have been propagated separately. . . . .	61
3.4	Interpolation of smooth motions on $SE(3)$ : Consistent interpolation between two rigid-body poses (blue and red ellipsoids, respectively), transformation parameters are: $t_i = 0mm$ , $t_j = 0mm$ , and $t_k = 0mm$ ; $r_i = 0^\circ$ , $r_j = 0^\circ$ , and $r_k = 30^\circ$ . 3 secondary rigid transformations $T^\alpha$ were interpolated between the identity and $T$ , giving a smooth trajectory of the rigid body between two poses in function of $\alpha$ ( $\alpha = \{n/4\}_{n \in \{1..3\}}$ in Eq 3.7). . . . .	65

3.5	Repeated evaluation of matrix exponential over a three dimensional grid. This figure shows that the trajectories of all the points of the grid are computed simultaneously. . . . .	67
3.6	Euclidean distance map, from left to right: binary mask of the calcaneus; associated Euclidean distance map. . . . .	68
3.7	Normalized weighting functions: from up to down, from left to right: for the calcaneus; for the talus; for the tibia; and the associated high-resolution static image. . . . .	69
3.8	Temporal evolution of the mean RMSE across the five sequences for A.tendon tracking using different weight functions. Orange curve: when using the weight functions defined in Equation (3.11) with $\alpha = 0.5$ and $\beta = 1$ ; green curve: when using the weight functions defined in Equation (3.11) with $\alpha = 0.5$ and $\beta = 2$ ; green curve: when using our weight functions defined in Equation (3.12) with $\gamma = 0.4$ . . . . .	71
3.9	Interpolation of missing time frames using the proposed forward tracking method: $D_k$ is the $k^{th}$ acquired time frame; while $D_{k,k+1}$ is the time frame half way between $D_k$ and $D_{k+1}$ (i.e. $\delta k = 0.5$ in Eq (3.9)). for $k = 1...3$ . . . . .	73
3.10	Effects of weighting functions on estimated deformation fields: (a) Target image; (b) Reconstructed image using the weighting functions defined in Equation (3.11) with $\alpha = 0.5$ and $\beta = 1$ ; (c) Reconstructed image using the weighting functions defined in Equation (3.11) with $\alpha = 0.5$ and $\beta = 2$ ; (d) Reconstructed image using our weighting functions defined in Equation (3.12) with $\gamma = 0.4$ . The contours of bones (magenta) and of Achilles tendon (white) have been drawn in the target image to show the reconstruction accuracies when changing the weighting functions. Despite the fact that all the used weighting functions conserve bone topologies (this was validated by checking that the Jacobian of the deformation field is equal to 1 over bone segmentations), the reconstructed image is more accurate for non-rigid structures such as the Achilles tendon when using our proposed weighting functions (d). . . . .	74
3.11	Jacobian maps of the joint deformation fields. From left to right: the deformation field that maps $D_1$ to $D_{1,2}$ ; and the deformation field that maps $D_1$ to $D_2$ where: $D_1$ is the $1^{st}$ acquired time frame while $D_{1,2}$ is the time frame half way between $D_1$ and $D_2$ . these maps estimate the local volume percentage difference of the targets with respect to the source time frame. A positive Jacobian determinant values reflect that there is no folding in the deformation field. . . . .	74

3.12	Consistent interpolation of a simulated affine map ( <i>i.e.</i> , the transformation that maps the blue ellipsoid to the red one), transformation parameters are: Translations: $t_i = 0mm$ , $t_j = 0mm$ , and $t_k = 0mm$ ; Rotations: $r_i = 0^\circ$ , $r_j = 0^\circ$ , and $r_k = 10^\circ$ ; Shearings: $g_i = 0$ , $g_j = 0$ , and $g_k = 0$ ; Scalings: $s_i = 1.5$ , $s_j = 1.5$ , and $s_k = 1.5$ . 4 secondary transformations $T^\alpha$ were interpolated between the identity and $T$ , giving a smooth affine trajectory of the ellipsoid between two instants in function of $\alpha$ ( $\alpha = \{n/5\}_{n \in \{1..4\}}$ in Eq 3.7). . . . .	75
4.1	<b>Problems related to thickness estimation: the actual thickness (green); and the calculated thickness using the method proposed in [142] (red).</b> . . . . .	80
4.2	Overestimation of the thickness $W = L_0 + L_1$ when initializing the boundary conditions for computing $L_0$ and $L_1$ at 0. The real thickness value is equal to 6 while the estimated thickness value is 7. . . . .	84
4.3	Estimation of the thickness $W = L_0 + L_1$ , in the case of isotropic resolution (voxel size of $1 \times 1 \times 1mm$ ), when initializing the boundary conditions for computing $L_0$ and $L_1$ according to [41]. . . . .	85
4.4	Computation of thickness for a circular annulus $C_a$ (white region in the top left) with inner radius of 50 voxels, and outer radius of 65 voxels. The theoretical thickness value should be equal to 15 inside $C_a$ ( <i>i.e.</i> the difference between the two radius). The obtained values using the Eulerian computational framework are effectively around $15.1 \pm 0.2$ voxels. . . . .	87
4.5	Three-dimensional solution of Laplace's equation (that gives the <i>harmonic interpolant</i> ) inside the synthetic sphere $S$ ( <i>i.e.</i> between its center $c$ and its surfaces) using the Jacobi iterative method (1000 iterations within 37sec). The initial Dirichlet boundary conditions are set as follows: $u(c) = 0$ and $u(\bar{S}) = 100$ . This experience aims to verify later, that the thickness value at each point $p = (x_p, y_p, z_p)$ inside the sphere is exactly equal to the sphere radius $r$ . Seven cross slices (between 15 and 111) are presented in this figure showing the solution of the Laplace equation inside $S$ . . . . .	89
4.6	The harmonic function $u$ and the corresponding <i>smooth</i> tangent field $\vec{N} = \frac{\nabla u}{\ \nabla u\ }$ inside a synthetic sphere. The harmonic function is obtained by solving the Laplace equation inside the sphere. Note that we have inverted the two boundaries here. So that the initial Dirichlet boundary conditions are set as follows: $u(c) = 100$ and $u(\bar{S}) = 0$ . This experience shows the heat propagation from the sphere center or nucleus to its external surfaces. . . . .	90
4.7	3D thickness map inside the simulated sphere (in $mm$ ). . . . .	91
4.8	Talar width in voxels . . . . .	92

4.9	Segmentation of the tibiotalar joint. Regions of interest are: tibia (green), talus (red), tibiotalar joint space (cyan). (a): Mid-coronal image from the high-resolution static image; (b) Three dimensional rendering of the joint. . . . .	93
4.10	Calculation of 3-D width of the tibiotalar joint space. (a) Harmonic function $u_1$ . (b) Length $L_0$ . (c) Length $L_1$ . (d) width ( $L_0 + L_1$ ): expressed in $mm$ from one sagittal slice of the first reconstructed time frame ( <i>i.e.</i> for $k = 1$ ). . . . .	94
4.11	Temporal evolution of the JSW: (a) Location of the centroid of the joint space mesh points ( $P_1$ ); (b) temporal evolution of the JSW around $P_1$ . The average across healthy subjects is shown as a solid line with one standard deviation above and below this line (grey shaded area). . . . .	96
4.12	Spatio-temporal evolution of the tibiotalar JSW during motion. The first row is composed of a set of dynamic anatomical images from one healthy subject: bone contours in neutral position show the joint motion across time. Width values were projected on each bone contact surface (the second row corresponds to the tibial plafond while the third row corresponds to the talar superior contact surface). . . . .	97
5.1	High-resolution reconstruction of one time frame using the proposed method. From up to down, from left to right: low-resolution time frame; reconstructed time frame; jacobian map of the deformation field from the static image to the acquired time frame. . . . .	100
5.2	T1-FFE sequence of the finger joint during motion. . . . .	101
A.1	Computation of 3D neonatal cortical thickness: (a) cortical gray matter segment (orange label, inside which the thickness will be computed); (b) white matter segment (green label, which will be considered as Dirichlet inner boundary); (b) complementary segment (purple label, which will be considered as Dirichlet outer boundary). Segmentations of cortex and white matter are performed using a fully automated processing pipeline [91], from a T2-weighted neonatal brain MRI. The voxel size of the image is $0.5 \times 0.5 \times 0.5mm$ . . . . .	103
A.2	Three-dimensional cortical thickness estimation. Thickness values are expressed in $mm$ . As recommended in [70] for data with $0.5 \times 0.5 \times 0.5mm$ resolution, the total number of iterations for solving Laplace's equation is set to 200 (performed within 36sec on a regular grid of $290 \times 290 \times 203$ ), giving very accurate thickness values inside the cortex in a bijective fashion. Three axial slices are shown to display the hidden information. . . . .	104

# List of Tables

3.1	3D DICE scores (for bones) and RMSE (for Achilles tendon contours) between manual segmentations of each structure of interest from the acquired data and segmentations of the same structures automatically-propagated onto the reconstructed data. Results are presented for several time frames across all subjects. . . . .	72
-----	--	----

## Acronyms

**MR** magnetic resonance

**MRI** magnetic resonance imaging

**JSW** joint space width

**ODE** ordinary differential equation

**cine PC** cine phase contrast

**fast PC** fast phase contrast

**FFE** fast field echo

**SE(3)** special Euclidean group

**SO(3)** special orthogonal group

**DOF** degree of freedom

**LEPF** log Euclidean polyaffine framework

**FFT** fast fourier transform

**ROI** region of interest

**LAPACK** linear algebra package

**PDE** partial differential equation

**PCA** principal component analysis

**ANTs** advanced normalization tools

**FLIRT** FMRIBs linear image registration tool

**FNIRT** FMRIBs non-linear image registration tool

**FSL** FMRIB software library

**RAM** Random-access memory

**TR** repetition time

**TE** echo time

**RMSE** root mean square error

**NIFTI** neuroimaging informatics technology initiative

**CT** computed tomography

**ISB** international society of biomechanics

**FOV** field of view

**OA** osteoarthritis

**IRB** institutional review board

**GE** gradient echo

**FA** flip angle

**CP** cerebral palsy

**ICP** iterative closest point

## List of Publications

### Journal Papers

- Makki, K., Borotikar, B., Garetier, M., Brochard, S., Ben Salem, D., Rousseau, F. (2019). In vivo ankle joint kinematics from dynamic magnetic resonance imaging using a registration-based framework. *Journal of biomechanics*, 86, 193-203.

### Conference Papers

- Makki, K., Borotikar, B., Garetier, M., Brochard, S., Ben Salem, D., Rousseau, F. (2018, April). High-resolution temporal reconstruction of ankle joint from dynamic MRI. In *2018 IEEE 15th International Symposium on Biomedical Imaging (ISBI 2018)* (pp. 1297-1300). IEEE.
- Makki, K., Borotikar, B., Garetier, M., Brochard, S., Ben Salem, D., Rousseau, F. (2019, July). Temporal resolution enhancement of dynamic MRI sequences within a motion-based framework. In *2019 Annual International Conference of the IEEE Engineering in Medicine and Biology Society (EMBC 2019)* . IEEE.
- Makki, K., Borotikar, B., Garetier, M., Acosta, O., Brochard, Ben Salem, D., Rousseau, F. (2019, July). 4D in vivo quantification of ankle joint space width using dynamic MRI. In *2019 Annual International Conference of the IEEE Engineering in Medicine and Biology Society (EMBC 2019)* . IEEE.

### Abstracts

- Makki, K., Borotikar, B., Garetier, M., Brochard, S., Ben Salem, D., Rousseau, F. High-Resolution MR Image Reconstruction for Ankle Joint Motion Analysis [abstract]. In: *Proceedings of the 8th World Congress of Biomechanics; 2018 July 8-12; Dublin, Ireland: WCB; 2018. P1076.*
- Makki, K., Borotikar, B., Garetier, M., Acosta, O., Brochard, S., Ben Salem, D., Rousseau, F. 4D in vivo non-invasive quantification of ankle joint space width using dynamic MRI [abstract]. Scheduled for oral presentation in the *XXVII Congress of the International Society of Biomechanics (ISB2019)*, held in conjunction with the *43rd Annual Meeting of the American Society of Biomechanics (ASB2019)*; 2019 July 31-Aug 4; Calgary, Canada: ISB/ASB; 2019.
- Makki, K., Borotikar, B., Garetier, M., Brochard, S., Ben Salem, D., Rousseau, F. In vivo ankle joint kinematics from dynamic MRI using a registration-based framework: towards spastic equinus deformities [abstract]. Oral presentation in the *31st EACD conference*; 2019 May 23-25; Paris, France: EACD; 2019.

# Contents

List of Figures . . . . .	ii
List of Tables . . . . .	ix
<b>1 Introduction</b>	<b>5</b>
1.1 Overview . . . . .	6
1.2 Clinical context . . . . .	6
1.2.1 Spastic Equinus deformity . . . . .	6
1.2.2 Anatomy of the ankle . . . . .	7
1.2.3 Gait analysis . . . . .	8
1.2.4 Management of spastic equinus . . . . .	9
1.2.5 Ankle biomechanics and spastic equinus . . . . .	10
1.2.6 From conventional static to dynamic imaging techniques . . . . .	11
1.2.7 Dynamic MRI . . . . .	11
1.2.8 <i>In Vivo</i> ankle joint biomechanics . . . . .	13
1.3 Image registration . . . . .	14
1.3.1 Rigid image registration . . . . .	14
1.3.2 Non-rigid image registration . . . . .	16
1.4 Mathematical tools for Dynamic MRI data post-processing . . . . .	18
1.5 Temporal evolution of nonlinear dynamical systems . . . . .	18
1.5.1 Ordinary differential equations ODEs . . . . .	18
1.5.2 Lie groups . . . . .	19
1.5.3 Group of 3D homogeneous rigid transformations $SE(3)$ . . . . .	19
1.5.4 Diagonalizability of the $4 \times 4$ homogeneous transformation matrices . . . . .	21
1.5.5 Linear interpolation on $SE(3)$ . . . . .	21
1.5.6 Log Euclidean Polyrigid Framework . . . . .	22
1.5.7 Some applications of the LEPF . . . . .	24
1.6 Matrix exponential . . . . .	25
1.6.1 The scaling and squaring method . . . . .	25
1.6.2 The eigendecomposition method . . . . .	26
1.6.3 The principal matrix logarithm . . . . .	27
1.6.4 Applications . . . . .	27
1.7 Rotations and quaternions . . . . .	28
1.8 Contributions summary . . . . .	29
1.9 Conclusion . . . . .	30
<b>2 In vivo Ankle Joint Kinematics from Dynamic Magnetic Resonance Imaging using a Registration-based Framework</b>	<b>33</b>
2.1 Introduction . . . . .	33
2.2 <i>In vivo</i> ankle joint biomechanics . . . . .	34

2.3	Materials and methods . . . . .	35
2.3.1	Subject recruitment . . . . .	35
2.3.2	Data Acquisition . . . . .	35
2.3.3	Motion estimation . . . . .	37
2.3.4	FSL-FMRIB's Linear Image Registration Tool: FSL-FLIRT . . . . .	38
2.3.5	Computation of temporal dense deformation fields . . . . .	40
2.3.6	Determination of ankle joint biomechanics . . . . .	41
2.3.7	Method evaluation . . . . .	42
2.4	Results . . . . .	43
2.5	Discussion . . . . .	43
<b>3</b>	<b>Temporal resolution enhancement of dynamic MRI sequences within a motion-based framework</b>	<b>55</b>
3.1	Introduction . . . . .	55
3.2	State of the art . . . . .	56
3.3	Motion artifacts in dynamic MRI sequences . . . . .	57
3.4	Methods . . . . .	58
3.4.1	Skeleton-tracking algorithm . . . . .	59
3.4.2	Smooth interpolation on $SE(3)$ : interpolation methods based on the exponential map . . . . .	60
3.4.3	Spatio-temporal Log-euclidean polyrigid framework: . . . . .	64
3.4.4	Redefinition of weighting functions . . . . .	67
3.4.5	Jacobian of the estimated deformation fields . . . . .	68
3.4.6	Combining the LEPF with the FSL registration tool . . . . .	69
3.5	Results . . . . .	70
3.6	Discussion . . . . .	73
3.7	Conclusion . . . . .	76
<b>4</b>	<b>4D in vivo non-invasive quantification of ankle joint space width using dynamic MRI</b>	<b>77</b>
4.1	Introduction . . . . .	77
4.2	State of the art . . . . .	78
4.2.1	From stationary to non-stationary data . . . . .	78
4.2.2	Related works . . . . .	79
4.2.3	Computation of soft tissue thickness . . . . .	80
4.2.4	Proposed pipeline . . . . .	81
4.3	A computational method: Eulerian framework for measuring soft tissue thickness . . . . .	81
4.3.1	Fast Eulerian PDE approach . . . . .	82
4.3.2	Experiments . . . . .	86
4.4	Spatio-temporal evolution of the JSW . . . . .	88
4.4.1	Temporal tracking of joint space area . . . . .	89
4.4.2	Computation of temporal joint space width . . . . .	91
4.5	Validation . . . . .	92

<b>Contents</b>	<b>3</b>
<hr/>	
4.6 Results . . . . .	93
4.7 Conclusion . . . . .	95
<b>5 Conclusions &amp; Perspectives</b>	<b>99</b>
<b>A Cortical thickness estimation</b>	<b>103</b>
A.1 Computation of neonatal cortical thickness . . . . .	103



# Introduction

## Contents

<b>1.1 Overview</b>	<b>6</b>
<b>1.2 Clinical context</b>	<b>6</b>
1.2.1 Spastic Equinus deformity	6
1.2.2 Anatomy of the ankle	7
1.2.3 Gait analysis	8
1.2.4 Management of spastic equinus	9
1.2.5 Ankle biomechanics and spastic equinus	10
1.2.6 From conventional static to dynamic imaging techniques	11
1.2.7 Dynamic MRI	11
1.2.8 <i>In Vivo</i> ankle joint biomechanics	13
<b>1.3 Image registration</b>	<b>14</b>
1.3.1 Rigid image registration	14
1.3.2 Non-rigid image registration	16
<b>1.4 Mathematical tools for Dynamic MRI data post-processing</b>	<b>18</b>
<b>1.5 Temporal evolution of nonlinear dynamical systems</b>	<b>18</b>
1.5.1 Ordinary differential equations ODEs	18
1.5.2 Lie groups	19
1.5.3 Group of 3D homogeneous rigid transformations $SE(3)$	19
1.5.4 Diagonalizability of the $4 \times 4$ homogeneous transformation matrices	21
1.5.5 Linear interpolation on $SE(3)$	21
1.5.6 Log Euclidean Polyrigid Framework	22
1.5.7 Some applications of the LEPF	24
<b>1.6 Matrix exponential</b>	<b>25</b>
1.6.1 The scaling and squaring method	25
1.6.2 The eigendecomposition method	26
1.6.3 The principal matrix logarithm	27
1.6.4 Applications	27
<b>1.7 Rotations and quaternions</b>	<b>28</b>
<b>1.8 Contributions summary</b>	<b>29</b>
<b>1.9 Conclusion</b>	<b>30</b>

## 1.1 Overview

In the last two decades, clinicians and researchers have focused on analyzing *in vivo* human movement patterns using advanced technologies like dynamic imaging techniques [18]. Dynamic magnetic resonance imaging (MRI) was originally developed for cardiovascular imaging to non-invasively quantify blood flow to study heart valve functions towards the end of the 1980s [110]. Since then, MRI acquisition and reconstruction techniques have improved by leaps and bounds with current sequences like cine phase-contrast MRI (cine-PC MRI) [129], fast phase-contrast MRI (fast-PC MRI) [13], ultrafast MRI [33], and real-time Fast Field Echo FFE sequences [120, 90]. Furthermore, dynamic MRI can be used to acquire high resolution static data (*i.e.* *stationary* data) and low resolution temporal images (*i.e.* *non-stationary* data). However, spatial and temporal data should be combined to provide the most comprehensive point of view to study joint motion.

This thesis aims to develop and create new frameworks to improve the diagnostic power of MRI and to process spatio-temporal anatomical MRI data. Processing this volumetric data can enable researchers to analytically track bones without having to identify specific points or anatomical landmarks and thus can provide the ability to track cartilage deformation as well as skeletal motion. These proposed frameworks tend to reduce the human intervention as much as possible while guaranteeing the measurement accuracies by combining spatial information of conventional static MRI with temporal information provided by four-dimensional (3D+time) dynamic MRI sequences.

## 1.2 Clinical context

### 1.2.1 Spastic Equinus deformity

Equinus is the most common deformity in children with cerebral palsy (CP) [48, 93]. Spastic equinus is typically defined as the inability to dorsi-flex the foot above plantigrade, with the hindfoot in neutral position and the knee in extended position [72, 132]. Approximately 90% of the deformities in CP occur in the ankle and foot region alone [73] with the incidence of equinus being around 75% [11]. Spastic equinus exhibits poor muscle control and muscle weakness around ankle and foot, resulting in gait abnormalities and bone deformities during growth. Specifically, a dynamic tightness or fixed contracture of the calf muscle disrupts the normal heel, ankle and forefoot rockers and impairs the function of the foot [108, 109]. Equinus deformity induces abnormal gait patterns decreasing the stability instance, causes a loss of the smooth translation of the body over the foot and often leads to an inadequate clearance of the foot during the swing phase of the gait [108, 109, 63].

### 1.2.2 Anatomy of the ankle

The ankle joint is a complex anatomical structure that links the foot and the lower leg. It is a synovial hinge joint and the main movements at this joint are: dorsiflexion which is produced by muscles of the anterior leg and limited by triceps surae (*e.g.* when bringing the toes up to its head); and plantar flexion which is produced by muscles of posterior compartment of leg (*e.g.* when walking on tiptoes).

#### 1.2.2.1 Bones of ankle joint

Bones of ankle joint are presented in Figure 1.1. The ankle joint consists of three joints: the tibiofibular joint, the tibiotalar joint, and the subtalar joint: The tibiofibular joint is the articulation between the tibia and the fibula, the tibiotalar joint occurs at the meeting point of the tibia and the talus, and the subtalar joint is the articulation between the talus and the calcaneus. The "mortise" is the concaved surface formed by the tibia and fibula. The surface is adjustable and is controlled by the proximal and distal tibio-fibular joints. The talus articulates with this surface and allows dorsiflexion and plantar flexion.

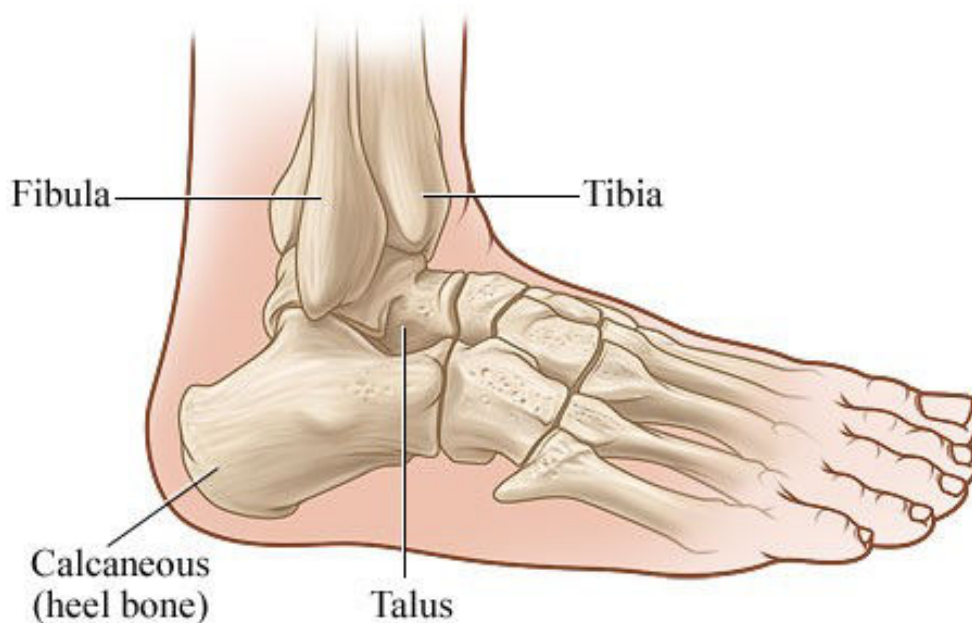


Figure 1.1: Bones of ankle joint. Source: <https://www.howtorelief.com/ankle-joint-anatomy-overview/>

#### 1.2.2.2 Ligaments and tendons of ankle joint

Ligaments maintain link between the two adjacent bones forming a joint and prevent separation of the bones. The medial and lateral ligaments are presented in Figures 1.2 and 1.3, respectively.



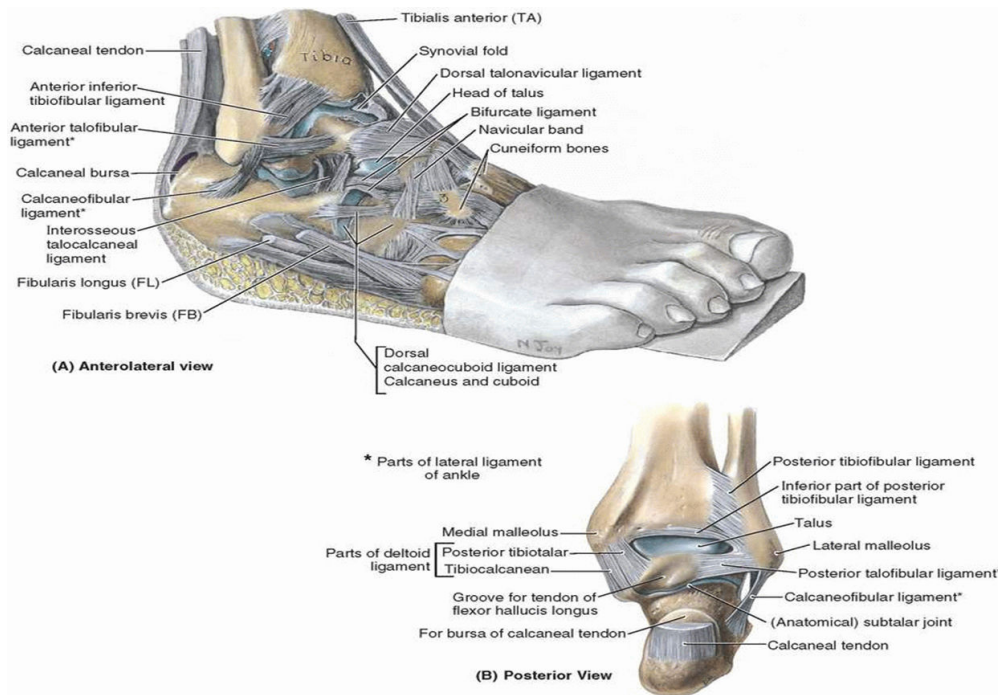


Figure 1.3: Lateral ligaments and tendons of ankle joint. Source: <https://www.memorangapp.com/flashcards/67023/012C+-+Lower+Limb/>.

kinematics will be computed using the VICON Plug-in Gait model [38]. In addition to the joint kinematics, joint powers and moments will be computed using an inverse dynamics method. In this thesis, we focused on a specific motion cycle: extracting the ankle joint kinematics during dorsi-plantarflexion using dynamic MRI to study the spastic equinus deformity since this pathology was defined as the inability to dorsiflex the foot above plantigrade, with the hindfoot in neutral position and the knee in extended position [72, 132].

#### 1.2.4 Management of spastic equinus

Management of spastic equinus deformity has been a long studied problem [135]. There is a general agreement that surgical intervention is the most viable option for fixed equinus deformity with the goal to stabilize the lower extremity, and efficiently use available strength to allow the patient to walk as independently as possible [132, 55, 44]. However, non-operative conservative management of equinus is typically undertaken up until 8 years in order to prevent recurrent equinus or overcorrection [21, 84] by avoiding high-growth phase of child's development for surgical intervention. Despite the large volume of published studies, there is an inconsistency in recommendations for treatment and lack of evidence for best clinical practice [54, 75]. This is reflected in post-surgical statistics as the long term follow-up studies report up to 48% of recurrence rate [44, 71, 32] and shows a general lack of understanding of spastic equinus deformity in children. Recurrence surgery not only increases the



Figure 1.4: Motion analysis laboratory at the CHRU Morvan and an example of a typical set-up for reflective marker placements on a healthy child.

economic burden on the society but also has a debilitating impact on children and their families.

### 1.2.5 Ankle biomechanics and spastic equinus

While deciphering the high prevalence of recurrence rates, researchers found that age and type of limb involvement were the major risk factors associated with the recurrence [21, 71]. However these risk factors have not been well-established as recent studies reported controversial outcomes [32]. In the hindsight, previous literature is focused on extrinsic risk factors such as CP type, demographic parameters, and clinical gait parameters for surgical recurrence and none assessed the intrinsic risk factors such as the internal ankle joint biomechanics, muscle mechanics or tendon strains. Being a dynamic pathology, it is critical to understand the *in vivo* effect of weak ankle joint musculature on joint mechanics and the resultant bone deformity. A primary reason for this recurrence could be a lack of understanding of bone deformity that might be forcing the child to adapt altered ankle joint and muscle mechanics (bone kinematics, cartilage contact parameters, muscle strain) during dynamic activities. A secondary reason could be hidden in the surgical approach itself that facilitates function rather than to stamp out deformity. This is further evident by the fact that the surgical interventions for correcting fixed equinus do not consider any bone corrections and focus on muscle release or lengthening only [132]. Consequently, optimal recommendations in each of these categories would be possible with a complete understanding of the functional intrinsic biomechanics of equinus deformity.

### 1.2.6 From conventional static to dynamic imaging techniques

Imaging methodologies have long played crucial role in helping surgeons and clinicians to guide or diagnose various disorders. Conventional static MRI techniques have been used for accurate diagnosis of the ankle and foot disorders given the complexity of their anatomy. However these techniques may not physiologically represent the dynamic musculoskeletal system [129, 18] and thus may mislead the treatment plans and strategies for children. *In vivo* imaging of moving articulated structures could be performed using different dynamic imaging techniques such as: computed tomography (CT) [137], ultrasonography (US) [56], single or bi-planar fluoroscopy [80], and MRI [123]. However, US is limited to the evaluation of soft tissues around the joint while CT and fluoroscopy are limited to quantifying bone kinematics and expose patients to ionizing radiations. MRI, being a *non-invasive* technique for the study of the musculoskeletal system, provides anatomical details of bones and surrounding soft tissues in both static and dynamic settings.

### 1.2.7 Dynamic MRI

In the last decades, researchers have developed and validated dynamic MRI techniques to analyze *in vivo* muscle and joint mechanics [128, 20, 19]. These techniques have been proven accurate and precise (*e.g.*, tracking error  $< 1mm$ ) in order to use them reliably as clinical diagnostic tools [13]. The dynamic MRI technique employs sequences that acquire three dimensional anatomical data throughout a motion cycle performed inside the magnet [131]. Furthermore, it remains non-ionizing, can handle both healthy and pathological joint function, and can visualize and track soft tissues as well. Thus, properties such as bone kinematics, cartilage contact mechanics, musculo-tendon moment arms, muscle strain and tendon strain are available from these analyses. Dynamic MRI techniques have been successfully employed to evaluate joint pathologies such as anterior knee pain in cerebral palsy [126]. Recently ankle joint kinematics, ankle instantaneous helical axes and Achilles tendon moment arms in adult population have also been reported in dynamic *in vivo* movements [129, 125, 124].

#### 1.2.7.1 Fast-PC MRI

Sequences such as cine-PC MRI [106, 131] or fast-PC MRI [127, 116] can provide *in vivo* joint velocity field measurements. However, these data require long acquisition times with a high number of repeated cycles: During each cycle, the MR scanner collects a single line of data in Fourier space over and over again. This process is continued until all lines of data are collected. Once the data are collected each cycle is interpolated to the desired number of time frames. Then all the lines representing the first time are put together and an image for the first time is created. This is repeated for all frames. The output of this process is a series of anatomical images portraying the different phases of the movement cycle.

The acquired fast-PC data typically consists of 30 temporal anatomic images which when played in a movie loop visually demonstrate how the ankle is moving. The 3D velocity vector for each pixel is basically a matrix of numbers defining the velocity for each pixel. A major clinical limitation of these sequences is that subjects with musculoskeletal disorders, who cannot complete a large number of repeated motion cycles, cannot be studied with cine-PC or fast-PC MRI.

### 1.2.7.2 Ultrafast-MRI

Ultrafast 3-T MRI is a feasible alternative imaging technique which has been employed to several clinical applications such as: prenatal diagnosis of congenital anomalies [62], evaluation of abusive head trauma [76], and also for the determination of ankle joint kinematics and for measuring muscle moment arms *in vivo* [33]. Contrary to fast-PC MRI technique, this imaging technique allows for capturing the joint trajectory during a single range-of-motion cycle, by exploiting spatio-temporal redundancy. Furthermore, it has the potential to be used under either passive (relaxed) or active (voluntary) muscle conditions without the need to control joint angular velocity or MRI gating.

Ultra-fast (turbo) gradient echo sequences have been used in the work of *Clarke et al.* [33] to obtain 20 time frames (with a resolution of  $1 \times 1 \times 4mm$ ) within 50 seconds. However, since these sequences are sensitive to motion artifacts, the motion itself is reduced to almost static or quasi-static nature (*i.e.* mean rotation speed of  $1^\circ/sec$ ) where no real functionality can be assessed.

Real-time T1 Fast Field Echo (T1-FFE) sequence is another valid and reliable technique to evaluate joint motion [18] with a good contrast between structures at the ankle [90], as illustrated in Figure 1.5. This imaging modality allows an *in vivo* quantification of joint kinematics where the scanning time for acquiring a single cycle of dorsi-plantar flexion is reduced to only 18s to acquire (15 time frames, with a spatial resolution of  $0.56 \times 0.56 \times 8mm$ ). Using these sequences in the current research, the rotation rate is 4 to 5 times higher than that of Ultra-fast (turbo) gradient echo sequences (*i.e.* mean rotation speed of  $4^\circ/sec$ ). A detailed description of the protocols used to acquire the dynamic MRI data is given in chapter 2.

To conclude, fast acquisition time, no need of repeated motions, and good soft tissue contrast are the key features that makes this method suitable for real-time evaluation of joint motion *in vivo* in normal and pathological conditions.

When compared to conventional static MRI, dynamic MRI comes with its own set of challenges such as the low-resolution, the anisotropy and the motion-related artifacts. Figure 1.6 illustrates the differences between static and dynamic data.

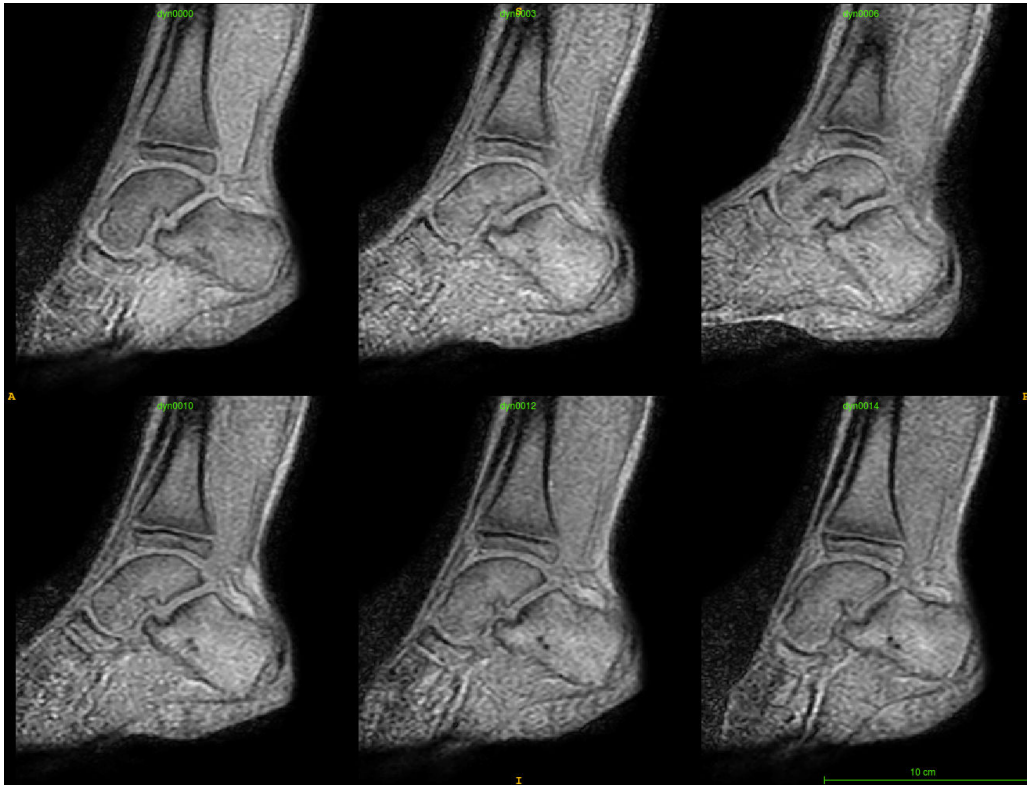


Figure 1.5: T1-FFE images of ankle joint during motion. The sequence is composed of 15 time frames, with a spatial resolution of  $0.56 \times 0.56 \times 8mm$ .

### 1.2.8 *In Vivo* ankle joint biomechanics

As a starting point of this research, our co-investigators in CHRU of Brest proposed to develop and implement the dynamic MRI techniques to quantify *in vivo* biomechanics of ankle joint with the help of image post-processing techniques later. This would provide original knowledge on the patho-physiology of equinus and its related consequences on gait. Our medium term goal is to provide a subject specific biomechanical assessment of equinus deformity to surgeons and clinicians. Development of dynamic MRI techniques will enable investigations that require functional assessment of joints and surrounding tissues. Furthermore, these tools may be applicable to other joints and related musculoskeletal disorders.

In previous works [33], a mesh-based registration technique is proposed to track bones across time. This method consists of registering the high-resolution bone models from the static image to the low-resolution bone models established at each time frame. However, their solution is limited as it requires the manual segmentation of all dynamic data in addition to the manual segmentation of the static MR scan. Moreover, this task is time consuming and prone to segmentation bias because of image noise and motion artifacts. In this work, we present to derive the joint



Figure 1.6: Static VS dynamic MRI: the left image corresponds to the dense high-resolution static image, while the right image corresponds to a sparse low-resolution time frame from a T1-FFE dynamic MRI sequence.

kinematics using an intensity-based registration tracking algorithm, which exploits all the available volumetric information by tracking the 3D bone segmentations. Using our method, the segmentation of dynamic data is performed automatically. And the rotations and translations of each bone with respect to another one is established from the estimated rigid transformations.

### 1.3 Image registration

Image registration [25, 102, 45] is the principal technique that we have used for motion reconstruction and for spatio-temporal data reconstruction during this thesis. Image registration methods can be divided into two families: rigid (linear) and non-rigid (non-linear).

#### 1.3.1 Rigid image registration

Rigid registration is the basic formulation of image registration. Theoretically, it aims to *maximize* a similarity measure (*e.g.* mutual information, correlation ratio, etc.) between two images (conventionally named source and target images, or floating and reference images in some documentations) in an intensity-based context (iconic approaches) or to *minimize* the distance between two point sets (*e.g.* mean squared error in point-wise distance between the source and target point sets) in a shape-based context. Whereas the main goal always remains the same; finding the optimal geometric transformation, that when applied to the source image or shape, aligns it with the target image or shape, respectively. The mathematical formulation

of this optimization problem is given by one of the two following equation:

$$T_{opt} = \underset{T \in A_T}{argmax} S(I_2, T(I_1)) \quad (1.1)$$

where:  $I_1$  is the source image;  $I_2$  is the target image;  $S$  is a similarity measure\*\* while  $D$  is a distance or cost function;  $A_T$  is the space of allowable transformations; and  $T_{opt}$  is the optimal geometric transformation that, when applied to  $I_1$ , aligns it with  $I_2$ . Note that the estimation of the optimal transformation  $T_{opt}$  can also be done by minimizing a cost function like the mean least squared error between image intensities before and after applying any allowable transformation to the floating image  $I_1$ .

\*\***Similarity measures:** In the context of intensity-based registration, the existing similarity measures can be divided into three categories: *statistical similarity* measures such as the correlation ratio (CR) or the normalized correlation (NC); *information theoretic similarity* measures such as the mutual information (MI), the normalized mutual information (NMI), and the entropy correlation coefficient (ECC); and *distance-based cost* functions such as the least squares (LS). The most commonly used intensity-based cost functions are defined mathematically as follows:

$$\begin{aligned} \text{CR} & \quad \frac{1}{N\sigma_Y^2} \sum_i N_i \sigma_{Y_i}^2 \in [0, 1] \\ \text{NC} & \quad \frac{\Sigma(X,Y)}{\sqrt{\Sigma X^2} \sqrt{\Sigma Y^2}} \in [-1, 1] \\ \text{MI} & \quad H(X, Y) - H(x) - H(Y) \in [-\infty, 0] \\ \text{NMI} & \quad \frac{H(X,Y)}{H(x)+H(Y)} \in [0, 1] \\ \text{LS} & \quad \Sigma(X - Y)^2 \in [0, +\infty] \end{aligned}$$

where:  $X$  and  $Y$  denote the two images, both represented as a set of intensities;  $\sigma_Y^2$  is the variance of the set  $Y$ ;  $Y_i$  is the  $i^{th}$  iso-set of intensities of  $Y$  at positions where the intensity in  $X$  is in the  $i^{th}$  intensity bin;  $N_i$  is the cardinal of  $Y_i$ ;  $H(X)$  and  $H(Y)$  are the marginal entropies; and  $H(X, Y)$  is the standard joint entropy of  $X$  and  $Y$ .

The registration process is composed of the principal following steps:

- **Optimization:** Each registration algorithm searches for maximizing the similarity measure in order to determine the optimal geometric transformation that aligns the source and target images, through the space of allowable transformations. The optimization process consists of varying the parameters of the transformation model to maximize the similarity measure.

- **Interpolation:** Once the optimal geometric transformation is determined, the alignment process requires the definition of the interpolation method. This method defines how the floating image intensities will be mapped to new coordinates in the target image space when applying the optimal transformation. The methods most commonly used are nearest neighbor, trilinear, Fourier and spline.

Rigid registration can be extended to include affine registration, which includes additional parameters (scalings and shearings) and this kind is commonly used in the context of brain registration for example.

### 1.3.2 Non-rigid image registration

Non-rigid or deformable registration is an important tool for assessing spatial and temporal changes between images [133]. Deformable registration has long been used in several fields such as: augmented reality during hepatic surgery [59], scanning microscope data [68], and medical imaging applications such as organ segmentation [25, 86, 95]. A review of the non-rigid registration is proposed in [37]. In general, non-rigid registration aims to optimize an energy function and is usually characterized by an additional regularization term (penalty term) during the optimization process in order to ensure smoothness of the deformation field. So that the equation (1.1) becomes as follows:

$$T_{opt} = \underset{T \in A_T}{\operatorname{argmax}} \quad S(I_2, T(I_1)) + \mathcal{R}(T) \quad (1.2)$$

where  $\mathcal{R}(T)$  is the regularization term. To regularize the resulting non-rigid transformation, there are two main methods according to [107]: either rely on regularization theory, or rely on physical models (elastic and viscous fluid models). Although this regularizer aims to smooth the estimated dense deformation field, this additional term can affect the local similarities (*e.g.* this can affect bone shapes by affecting sharp peaks in the context of articulated registration, which was the case in the work of Abbas *et al.* [1] for estimating the non-linear deformations of the wrist joint).

According to Sotiras *et al.* [133], the deformable registration algorithms can be classified into four groups based on the transformation model that they use:

- **Transformations derived from physical models** [96], such as: elastic body models relying on partial differential equations (PDEs) [24], curvature registration where the deformation is modeled by an equilibrium equation [52], viscous fluid flow models where the geometric transformation is governed by the Navier-Stokes equation [31], and flows of diffeomorphisms such as the Large Deformation Diffeomorphic Metric Mapping (LDDMM) Framework [12] which determines correspondences between two images or two sets of points via the geodesic distances.
- **Transformations derived from interpolation theory and approximation theory**, such as: interpolation of the deformation using the radial basis functions (RBFs) [144], elastic body splines [39], free-form deformations

(FFDs) and their symmetric extension proposed by *Noblet et al.* under the assumption that both source and target images will deform toward a common domain under the influence of two isomorphic grids [103], and finally locally-affine models which guarantee the invertibility of transformations [5].

- **Knowledge-based geometric transformations**, such as: statistically-constrained transformations for which the spatial constraints are established based on a statistical information about deformation fields across a high number of subjects in order to reduce the number of DOFs and thus the complexity of geometric transformations. These statistical models have been successfully employed to study shape variability and to accelerate image alignment and segmentation [36, 136]. The registration is constrained here by performing principal component analysis (PCA) on point correspondences. A finite element methods (FEMs) involving statistical priors on biomechanical properties of tissues are also employed to estimate complex deformation fields with the use of few DOFs, such as the biomechanical models of the breast [9], and the biomechanical models of the prostate [97].
- **Task-specific constraints**: some methods are proposed with the goal of *preserving topologies*, such as: the method proposed by *Christensen et al.* [30] which consists of constraining the transformation by adding a penalty term to the similarity function, that acts upon the Jacobian values (*i.e.* a term that penalizes small and large Jacobian determinant values for both forward and backward deformation fields). A similar method is proposed by *Rueckert et al.* in which the authors proposed to add, a term penalizing the values of the Jacobian that are close to zero, to the objective function [118]. A non-rigid FFD registration method imposing local rigidity constraints is proposed in [82]. In this work, the alignment is achieved by penalizing deviations of the Jacobian from orthogonality.

Since we process volumetric static and dynamic MRI data in our study, we proposed to divide the non-linear joint registration into two parts: first, the registrations of bones are constrained assuming their rigid nature, meaning the local bone transformations are individually estimated using a robust intensity-based registration algorithm relying on local similarities. Second, a smooth deformation field of the joint is obtained in a fast way by fusing the set of locally rigid transformations.

Contrary to rigid registration which can be determined in few seconds, most non-rigid registration algorithms require minutes or hours in determining a large number of parameters [37]. This is another reason which motivates our choice for the Log Euclidean Polyrigid Framework (LEPF) for which the resulting polyrigid transformations (*i.e.* resulting from fusing a set of multiple rigid transformations, corresponding to each bone of interest) are parametrized by a small number of intuitive parameters (*i.e.* only 6 parameters per rigid component and 12 parameters

per affine component). Furthermore, the resulting log-euclidean polyrigid transformations have the properties of a diffeomorphism, including invertibility and differentiability. In the next sections, we detail this registration framework and the mathematics behind.

## 1.4 Mathematical tools for Dynamic MRI data post-processing

In the sequel, we will present the developed mathematical tools that we have used to perform non-rigid image registration during this thesis. This part will present the different theories in relation with our work. The principal topics in focus are: geometric flows and ODEs (Section 1.5.1), Lie algebra (Sections 1.5.2 and 1.5.3), different methods for computing the matrix exponential, eigenvalue problems and their usefulness for the parameterization of non-rigid geometrical deformations with a small number of flexible DOF (Section 1.6.2), and geometric PDEs and their usefulness for computing soft tissue thickness that we will describe later in chapter 4.

## 1.5 Temporal evolution of nonlinear dynamical systems

In this section, we introduce the use of the theory of ordinary differential equations to handle the spatio-temporal evolution of nonlinear dynamical systems [105].

### 1.5.1 Ordinary differential equations ODEs

The trajectory of a point  $x$ , or more generally, of any vector field on a continuously differentiable manifold  $\mathcal{T}(x)$  between two instants (0 and 1) during a specific motion cycle can be modeled by the following Ordinary Differential Equation (ODE):

$$\dot{x} = V(x, \alpha) \tag{1.3}$$

with the initial condition  $x(\alpha_0) = x_0$ ; where  $V$  is a non-linear function, called the velocity vector field, and  $\alpha \in [0, 1]$  is the time term. The key idea is to split  $V$  into a set of  $N$  locally linear velocity vector fields  $v_i(\cdot, \alpha)_{i \in \{1 \dots N\}}$ .

Solving this ODE by varying  $\alpha$  continuously from  $\alpha_0 = 0$  to  $\alpha_1 = 1$  will smoothly integrate the entire trajectory of the point  $x$  (*i.e.*  $\alpha$ -change of the *infinitesimal* displacement of  $x$ ), starting from the initial position  $x_0$ , until reaching the final position  $x(1) = T(x_0)$  as illustrated in Figure 1.7.

For some cases, such as inter-subject registration for comparison purposes, it could be just needed to estimate the deformation vector between the start and end positions ( $x_0$  and  $x(1) = T(x_0)$ ), so that  $V(x_0, \alpha) = V(x_0, 1)$  does not depend on  $\alpha$ . In this case, the ODE is called stationary or autonomous.

The solution of this first order ODE that we note  $\phi(x_0, \alpha)$  is called the *flow*, which is dependent on the initial condition  $x_0$ . More generally, the one-parameter family

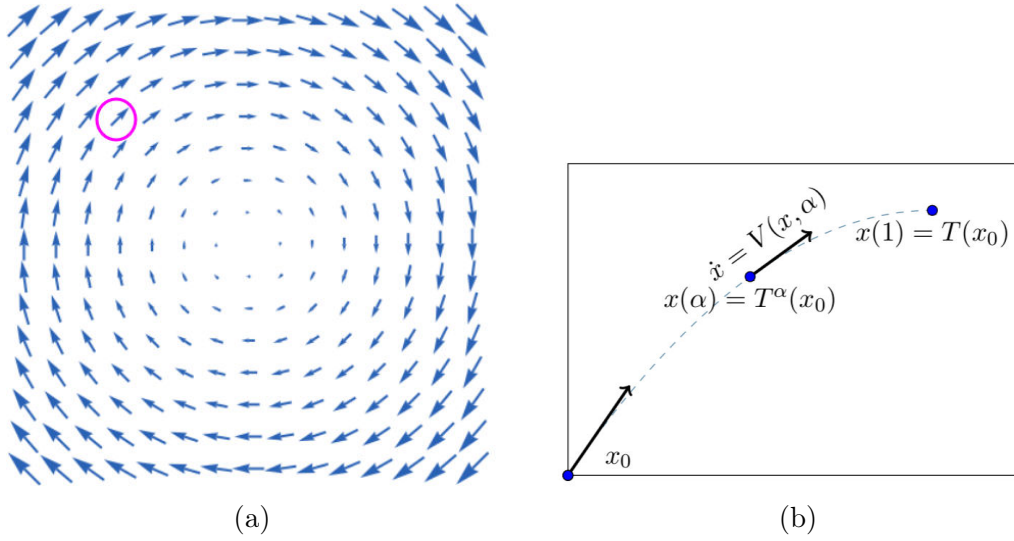


Figure 1.7: ODE integration: (a) a synthetic deformation field (velocity vector field) over a regular grid; example of a single clockwise rotation (rotation angle of  $-50$  degrees around the origin), (b) infinitesimal displacement of one velocity vector ; in particular we have zoomed a single point trajectory between the source and target positions in order to show the temporal evolution of the associated velocity vector (*i.e.* the elementary tangent vectors along the integral point trajectory).

of mappings (*i.e.* the one parameter subgroup of the group of *diffeomorphisms*),  $\phi(\cdot, \alpha) : \mathbb{R}^n \rightarrow \mathbb{R}^n$  satisfies Eqn. (1.4):

$$\begin{aligned} \phi(\cdot, 0) &= id, \\ \phi(\cdot, \alpha_1) \circ \dots \circ \phi(\cdot, \alpha_m) &= \phi(\cdot, \alpha_1 + \dots + \alpha_m). \end{aligned} \quad (1.4)$$

### 1.5.2 Lie groups

Starting from its *algebraic sense*, a Lie group is a first order group in which the multiplication of elements is defined [74]. It is also a topological group (*i.e.* a smooth manifold or  $C^\infty$ -manifold) with a set of properties like *invertibility*, *multiplication*, and *differentiability*. In particular, the group of 3D rigid transformations  $SE(3)$  (linear transformations on homogeneous 4-vectors, as defined in Eq. (1.5) is a Lie group (*i.e.* a *continuous*-transformation group) associated with the Lie algebra  $so(3)$ , where the composition of mappings corresponds to the multiplication of elementary (*i.e.* *infinitesimal*) transformations.

### 1.5.3 Group of 3D homogeneous rigid transformations $SE(3)$

The Lie group of 3D homogeneous rigid transforms (*i.e.* the differentiable manifold with structure  $so(3) \times \mathbb{R}^3$ ) [17], also denoted as the special Euclidean group  $SE(3)$ ,

is defined as follows:

$$SE(3) = \left\{ T \mid T = \left[ \begin{array}{c|c} R & t \\ \hline 0_{1 \times 3} & 1 \end{array} \right], R \in SO(3), t \in \mathbb{R}^3, R^T R = R R^T = I, |R| = 1 \right\} \quad (1.5)$$

Each element  $T$  in  $SE(3)$  possess six degrees of freedom (DOFs) of relative movement as it is composed of two parts: a linear  $3 \times 3$  bloc  $R \in SO(3)$  describing the three spatial rotations and an additional  $3 \times 1$  translation vector  $t \in \mathbb{R}^3$  that describes the displacement with respect to the origin. The following Equation presents the direct approach to apply a rigid transformation to a point  $x$  in order to obtain the location of point  $y$  (see Fig 1.8):

$$y = Rx + t \quad (1.6)$$

The above defined Equation requires the vector addition. Hence, mixing the rotation bloc and the translation vector allows for a direct matrix-vector multiplication (i.e.  $\tilde{y} = T \cdot \tilde{x}$ ). So that  $T$  can be written as  $4 \times 4$  matrix:

$$T = \begin{pmatrix} R & t \\ 0 & 1 \end{pmatrix} \quad (1.7)$$

If  $x = \begin{bmatrix} x_0 \\ x_1 \\ x_2 \end{bmatrix}$ , then  $\tilde{x}$  is simply obtained by adding an extra "1" to  $x$ ,  $\tilde{x} = \begin{bmatrix} x_0 \\ x_1 \\ x_2 \\ 1 \end{bmatrix}$ .

It is also possible to interpolate a 3D rigid transformation after considering all the allowed rotations and translations as a single bloc (see section 3.4.2).

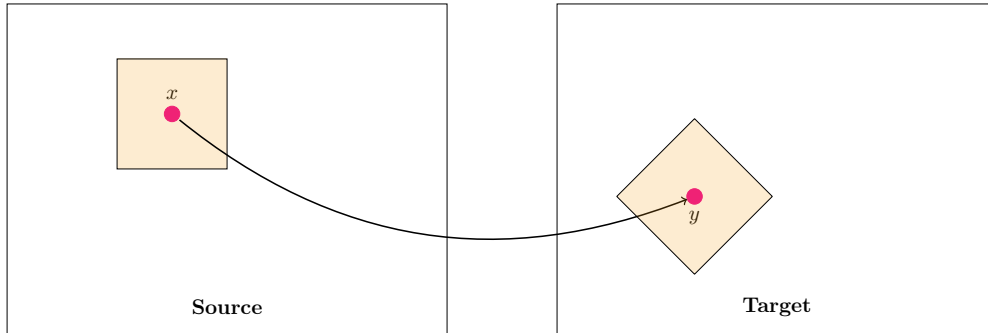


Figure 1.8: Apply a synthetic rigid transformation  $T$  in  $SE(3)$ , expressed in an orthonormal basis  $(O, \vec{i}, \vec{j}, \vec{k})$ , to a point  $x$ . Transformation parameters are set as follows:  $R_i = 0^\circ$ ,  $R_j = 0^\circ$ ,  $R_k = 45^\circ$ ,  $t_i = 0$ ,  $t_j = -1.5$ , and  $t_k = 0$ . The result is given by  $\tilde{y} = \begin{pmatrix} y \\ 1 \end{pmatrix} = T \tilde{x}$ .

Moreover, matrices in  $SE(3)$  satisfy:

- **Closure property:** if  $T_1$  and  $T_2$  are two elements  $\in SE(3)$ , then their matrix product  $T_1T_2 \in SE(3)$ .
- **Associative property:** if  $T_1, T_2$  and  $T_3 \in SE(3)$ , then  $(T_1T_2)T_3 = T_1(T_2T_3)$ .
- **Neutral element:**  $\forall T \in SE(3)$ ,  $T$  verifies  $T.I = T$  where  $I$  is the  $4 \times 4$  identity matrix.
- **Inverse:**  $\forall T \in SE(3)$ ,  $T$ , there is an inverse  $T^{-1} \in SE(3)$ , such that  $T^{-1} = I$ .

In addition, this *algebraic* group is a continuous group. Meaning the product of any two matrices in  $SE(3)$  is a continuous function of the two matrices and the inverse of any matrix in  $SE(3)$  is a continuous function of that matrix.

#### 1.5.4 Diagonalizability of the $4 \times 4$ homogeneous transformation matrices

In general, a  $4 \times 4$  rigid transformation matrix is *diagonalizable*. With the exception of screw transformations (*i.e.*, when the motion consists of a rotation about an axis and a translation along the same axis). If we take the example of screw motion through the  $z$  - axis, the screw transformation will be:

$$T_\theta = \begin{bmatrix} \cos(\theta) & -\sin(\theta) & 0 & u_x \\ \sin(\theta) & \cos(\theta) & 0 & u_y \\ 0 & 0 & 1 & u_z \\ 0 & 0 & 0 & 1 \end{bmatrix} \quad (1.8)$$

where  $T_\theta \in SE(3)$ ,  $U = (u_x, u_y, u_z)$  is the translation vector, and  $\theta$  is the rotation angle about the  $z$  - axis. This matrix is diagonalizable if and only if the translation along the  $z$  - axis,  $u_z = 0$  [51]. In fact, the eigenvalues of  $T_\theta$  in the complex domain are:  $\{e^{i\theta}, e^{-i\theta}, 1, 1\}$ . So that the eigenvectors corresponding to the repeated eigenvalue 1 are linearly dependant, and thus the matrix  $T_\theta$  is non-diagonalizable. For example, the human bones may never be able to perform screw motions in normal conditions due to the natural joint mechanical constraints. This suggests that rigid bone transformations are always diagonalizable. An example of screw motion through the z-axis is illustrated in Figure 1.9.

#### 1.5.5 Linear interpolation on $SE(3)$

In this section, we adress the problem of finding a smooth continuous-time trajectory that interpolates between two rigid body poses [121, 14]. We introduce a matrix-diagonalization based approach thanks to the above algebraic properties, involved in  $SE(3)$  :

Let  $T \in SE(3)$  be the transformation matrix coding the rigid movement of a three-dimensional shape between two different poses. Assuming that this transformation is *diagonalizable* (which is the case for most transformations in an orthonormal basis, like the image coordinate system), then there exist an orthogonal matrix

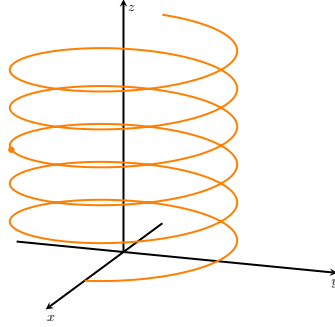


Figure 1.9: Example of screw motion through the z-axis.

$P$  and a diagonal matrix  $D$  such that  $T = PDP^{-1}$ . The non-zero elements of  $D$  are the eigenvalues of  $T$  ( $\lambda_1, \lambda_2, \lambda_3$ , and  $\lambda_4 = 1$ ), while the columns of  $P$  are the corresponding eigenvectors. Based on this matrix eigendecomposition, one can define  $T$  raised to its  $\alpha^{th}$  power as follows:

$$T^\alpha = PD^\alpha P^{-1} = P \begin{pmatrix} \lambda_1^\alpha & 0 & 0 & 0 \\ 0 & \lambda_2^\alpha & 0 & 0 \\ 0 & 0 & \lambda_3^\alpha & 0 \\ 0 & 0 & 0 & 1 \end{pmatrix} P^{-1} \quad (1.9)$$

Changing  $\alpha$  continuously from 0 to 1 will change the matrix  $T^\alpha$  from *identity* to the matrix  $T$ . This allows for interpolating between two distinct rigid-body poses from a realistic transformation matrix, expressed in homogeneous coordinates. Fig 1.10 illustrates the linear interpolation of one simulated rigid transformation (3 rotations+3 translations).

## 1.5.6 Log Euclidean Polyrigid Framework

### 1.5.6.1 Original Polyrigid Transformations

In the context of medical image analysis, Arsigny et al. [7] have modeled the registration process as a temporal transformation of point coordinates from time  $\alpha = 0$  to time  $\alpha = 1$ . This framework with ODEs is called *polyrigid and polyaffine transformations* as it can deal with nonlinear geometric deformations. As we said in Section 1.5.1, the goal is to divide the velocity vector field  $V$  into a set of  $N$  locally linear velocity fields  $v_i$  according to the following equation:

$$\dot{x}(\alpha) = V(x, \alpha) = \frac{\sum_{i=1}^N w_i(x) v_i(x, \alpha)}{\sum_{i=1}^N w_i(x)}; \quad \text{with } x(t_0) = x_0 \quad (1.10)$$

where  $w_i(x)$  is a weighting function that reflects the local influence of the velocity of the local transformation  $v_i(x)$  associated to the region  $i$  at point  $x$ , on the final velocity vector field  $V$  obtained when  $\alpha$  is equal to 1. Let's take the case of articulated structures registration as an example: using this framework, one can estimate

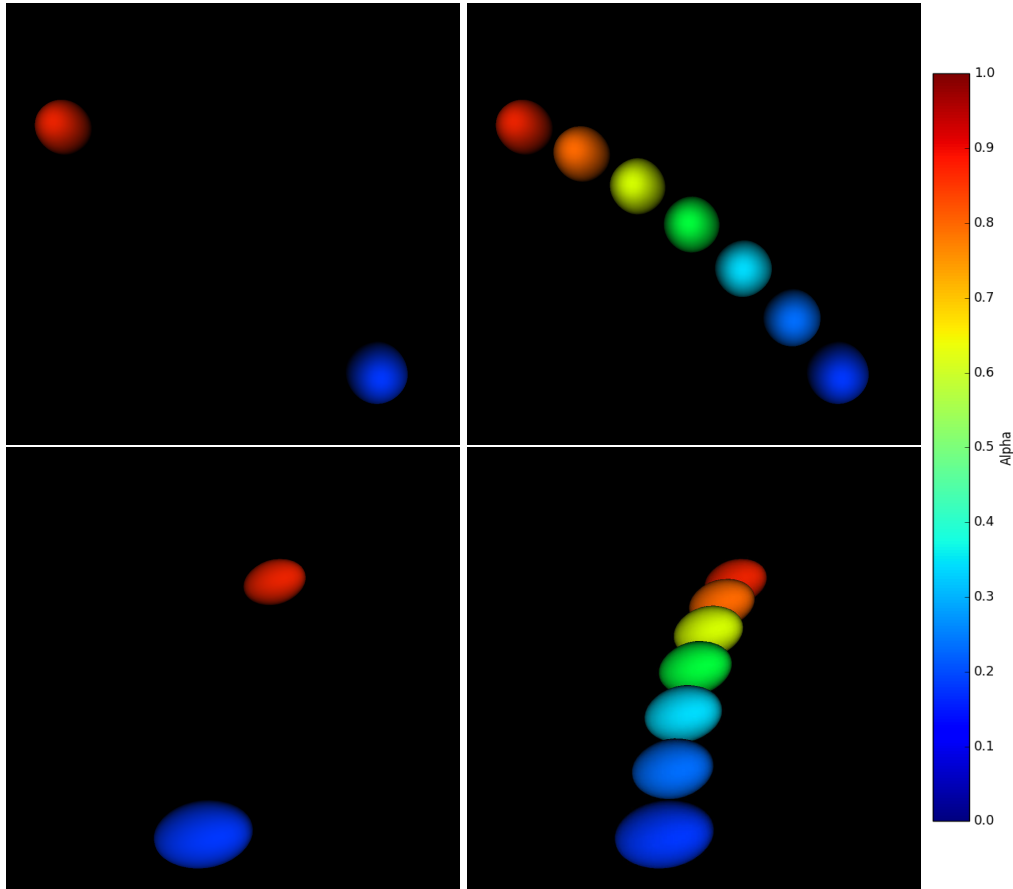


Figure 1.10: Interpolation of smooth motions on  $SE(3)$ : consistent interpolation of a simulated 3D rigid transformation  $T$  that maps the blue ellipsoid (initial pose) to the red one (final pose), transformation parameters are:  $t_i = 0mm$ ,  $t_j = 0mm$ , and  $t_k = 0mm$ ;  $r_i = 0^\circ$ ,  $r_j = 0^\circ$ , and  $r_k = 30^\circ$ . 5 secondary rigid transformations  $T^\alpha$  were interpolated between the identity and  $T$ , giving a smooth trajectory of the rigid body between two poses in function of  $\alpha$  ( $\alpha = \{n/6\}_{n \in \{1..5\}}$  in Eq 3.7).

a dense deformation field from just a few parameters,  $6N$  parameters if we have to fuse  $N$  rigid components. Meaning we would like to define an average polyrigid transformation as  $T(x_0) = \phi(x_0, 1)$ , where  $\phi$  is the smooth geometric flow associated to the ODE (1.10). Some shortcomings of this framework are:

- First, the proposed polyrigid fusion is not invariant with respect to a change of coordinate system.
- Second, the inverse of a polyrigid transformation is not polyrigid in general.

### 1.5.6.2 Log Euclidean Polyrigid Transformations

To overcome the above-mentioned limitations of the original polyrigid fusion, Arsigny et al. [5] proposed a new framework called *Log Euclidean Polyrigid Trans-*

*formations.* Since we have the relation  $\exp(\log(T^\alpha)) = \exp(\alpha \cdot \log(T))$ , the flow  $\phi(x, \alpha)$  which corresponds to the infinitesimal log Euclidean polyrigid transformation  $T(x, \alpha)$ , can be computed via the following non-stationary equation:

$$\phi(x, \alpha) = \exp \left( \alpha \sum_{i=1}^N \tilde{w}^i(x) \log(T^i) \right) \cdot \tilde{x}; \quad \text{with } x(t_0) = x_0 \quad (1.11)$$

where  $x$  is expressed in homogeneous coordinates;  $\alpha \in [0, 1]$  is the time-term;  $N$  is the total number of rigid components;  $T^i \in SE(3)$  is the rigid transform from the source to the target image for the component  $i$ ; and  $\tilde{w}^i$  is a normalized weighting function (*i.e.*  $\sum_{i=1}^N \tilde{w}^i(x) = 1$ , for all  $x$  in the source image).

Since  $\phi(x, \alpha)$  is a diffeomorphism, this mapping yields nice algebraic properties such as invertibility and bijectivity, leading to a smooth mapping of one differentiable manifold to another.

From a computational point of view, it is possible to fastly compute this mapping in regular grids thanks to the above-listed algebraic properties, defined in the Lie groups of rigid transformations expressed in homogeneous coordinates  $SE(3)$ . The computation of the exponential mapping of (1.11) can be computed using different techniques that we will discuss in the sequel (Section 1.6).

### 1.5.7 Some applications of the LEPF

This framework covers the fusion of affine transformations as well as rigid transformations. It is to be noticed that an affine transformation is a linear transformation which encodes a geometrical deformation within 4 parameter vectors; rotations, translations, scaling and shearing (*e.g.* 12 degrees of freedom DOFs in 3D). The LEPF has been then used in several applications: in [104], the authors prove that this type parameterization is well-adapted to the registration of articulated structures such as the hip and knee joint for serial x-ray CT mouse images; in [92], an extension of the Log Euclidean polyrigid registration was presented to deal with human articulated structures from 2D radiographs. Recently, the LEPF has been applied to surgical planning of fronto-orbital advancement. This work aims to estimate the necessary bone piece repositioning for achieving the optimal post-surgical cranial shapes [113]. In this thesis, we have extended these techniques to estimate the spatio-temporal evolution of human joints (*e.g.* the ankle joint). To do this, we have proposed an intensity based registration framework for combining spatial information of conventional static MRI with temporal information of dynamic MRI sequences [88, 90].

## 1.6 Matrix exponential

Towards the end of the 1970s, *Moler and Van Loan* have synthesized a study to present the different ways of computing the matrix exponential [99]. This famous study has been revisited more than two decades later in [100] to take advantage of the advances of computational resources and to classify the existing methods and algorithms in terms of generality, accuracy, storage requirements, and efficiency. This study has pointed out that the choice of the best method depends on the application. For example, algorithms which avoid use of the eigenvalues are more time-consuming for any particular problem. Moreover, they are prone to roundoff errors especially where the matrix to be exponentiated has large elements.

In this work, we will only focus on two techniques that are more suitable for computing the matrix exponential in dense regular grids: the scaling and squaring method and the eigen decomposition method [77]. These two methods, which are based on *factorizations* or *decompositions* of the matrix, are likely to be most efficient for problems involving homogeneous transformation matrices and repeated evaluation of their exponentials.

The real exponential function is defined by this following power series:

$$e^x = \sum_{n=0}^{\infty} \frac{x^n}{n!} = 1 + x + \frac{x^2}{2!} + \frac{x^3}{3!} + \dots \quad (1.12)$$

This power series decomposition, also known as the Taylor series expansion of the exponential function, is still available for expressing the exponential of a square real or complex matrix. So that the matrix exponential of an  $m \times m$  matrix  $T$  can be defined by the following convergent power series:

$$e^T = \sum_{n=0}^{\infty} \frac{T^n}{n!} = I_m + T + \frac{T^2}{2!} + \frac{T^3}{3!} + \dots \quad (1.13)$$

where  $I_m$  is the  $m \times m$  identity matrix.

To summarize, the matrix exponential can be approximated with a certain level of accuracy by neglecting high-order terms under certain conditions using the scaling and squaring method and it can be exactly computed using matrix eigen decomposition.

### 1.6.1 The scaling and squaring method

The scaling and squaring method [98, 78] is a recursive technique that exploits the fact that the matrix exponential can be easily estimated for matrices close to zero (coming from the scaling step) using the Padé approximants, by neglecting the high-order terms. This method is based on the relation  $e^T = (e^{\frac{T}{2^s}})^{2^s}$ . The first step (scaling step) consists of evaluating  $e^{\frac{T}{2^s}}$  while the second step (squaring step) consists of squaring the approximant  $s$  times to finally obtain an estimation of  $e^T$ . The accuracy of this technique involving approximation theory seems to be

satisfactory under certain conditions as it depends on the input parameters which are the total number of iterations  $N$  and the scaling factor  $s$  (note that  $N$  and  $s$  are two integers). In fact, the rounding errors introduced during the repeated squaring have a similar effect as that of a perturbation in the original matrix  $T$  itself. The efficiency of this technique over a regular grid is somehow comparable to that of the Fast Fourier Transform (FFT) according to Arsigny et al [5]. However, *Moler et Van Loan* [100] have concluded that this method is efficient for computing  $e^T$ , but not so efficient for computing  $e^{\alpha T}x$  for a given vector  $x$  (which represents the point components expressed in homogeneous coordinates in the registration context) and many values of  $\alpha$  (which is the case for non-stationary acquisitions like dynamic MRI sequences).

## 1.6.2 The eigendecomposition method

### 1.6.2.1 Definition

The matrix eigendecomposition [149] is the factorization of the matrix (supposed to be diagonalizable) into a canonical form. Let  $T$  to be a square  $m \times m$  real or complex matrix, then its distinct eigenvalues  $\{\lambda_k\}_{k \in \{1 \dots m\}}$  can be determined by solving the *characteristic* equation  $\det(T - \lambda_k I_m) = 0$  while the corresponding eigenvectors  $\{v_k\}_{k \in \{1 \dots m\}}$  satisfy the linear equation  $Tv_k = \lambda_k v_k$ , also known as the *eigenvalue problem*. Hence, a factorization of  $T$  can be expressed as:  $T = P.D.P^{-1}$ , where the columns of  $P$  contains the eigenvectors  $v = \{v_k\}_{k \in \{1 \dots m\}}$  corresponding to the eigenvalues of  $T$ ,  $\lambda = \{\lambda_1, \lambda_2, \dots, \lambda_m\}$  which are the non-zero elements of  $D$ . So that the exponential of  $T$  can be computed according to the following equation:

$$e^T = P e^D P^{-1} = P \begin{bmatrix} e^{\lambda_1} & 0 & \dots & 0 \\ 0 & e^{\lambda_2} & & \vdots \\ \vdots & & \ddots & 0 \\ 0 & \dots & 0 & e^{\lambda_m} \end{bmatrix} P^{-1} \quad (1.14)$$

where  $D$  is a *diagonal* matrix and  $P$  is an *orthogonal* matrix in general.  $e^T$  is a  $m \times m$  invertible matrix where the inverse can be computed according to:

$$(e^T)^{-1} = P^{-1} e^{-D} P = P^{-1} \begin{bmatrix} e^{-\lambda_1} & 0 & \dots & 0 \\ 0 & e^{-\lambda_2} & & \vdots \\ \vdots & & \ddots & 0 \\ 0 & \dots & 0 & e^{-\lambda_m} \end{bmatrix} P \quad (1.15)$$

#### Explication:

According to Equation 1.13, if  $T$  is a *diagonalizable* square matrix then it can be expanded into its power series as follows:

$$e^T = \sum_{n=0}^{\infty} \frac{(P.D.P^{-1})^n}{n!} \quad (1.16)$$

$T$  raised to its  $n^{\text{th}}$  power can be written as follows:

$$T^n = (P.D.P^{-1})^n = \overbrace{P.D.\underbrace{P^{-1}.P}_I.D.\underbrace{P^{-1}.P}_I \dots \underbrace{P^{-1}.P}_I.D.P^{-1}}^{n\text{-times}} = P.D^n.P^{-1} \quad (1.17)$$

where  $I$  is the identity matrix.

Combining (1.16) with (1.17) we have:

$$e^T = \sum_{n=0}^{\infty} \frac{P.D^n.P^{-1}}{n!} = P.\underbrace{\sum_{n=0}^{\infty} \frac{D^n}{n!}}_{=e^D}.P^{-1} \quad (1.18)$$

The advantage of the eigen decomposition method is that it automatically takes into account all the terms (including the high-order terms in Equation 1.13). This method leads to a more accurate computation of the matrix exponential when compared to the scaling and squaring method.

It should be noticed that the matrix logarithm and the  $n^{\text{th}}$  matrix power can be determined in the same way by computing the natural principal logarithm and the  $n^{\text{th}}$  power of the eigenvalues, respectively. Although it is obvious that the matrix power can be computed using this matrix-diagonalization based method according to Equation 1.17, the matrix logarithm can be computed similarly to the matrix exponential, simply because the natural logarithm and the exponential are two inverse functions (*i.e.*  $\exp(\log(T)) = \log(\exp(T)) = T$ , for all square matrix  $T$ ).

### 1.6.3 The principal matrix logarithm

Given a matrix  $T = \begin{pmatrix} R & t \\ 0 & 1 \end{pmatrix} \in SE(3)$ , a logarithm of  $T$  is defined as  $\log(T) = \begin{pmatrix} L & v \\ 0 & 0 \end{pmatrix}$ , where  $v = \log(t)$  and  $L = \log(R)$ .  $L$  can be computed using the eigen-decomposition technique previously described [29, 27]. However, this quantity is not unique because of the rotational periodicity so that the matrix logarithm  $\log(T)$  is also not unique. In the context dynamic MRI, this is not a problem in itself as the local rotations are smaller in magnitude than  $\pi$  radians (*i.e.* the imaginary part of the eigenvalues of  $R$  are smaller than  $\pi$  because there are no large deformations between successive frames) so that the matrix logarithm is unique. This is called the *principal matrix logarithm* [5].

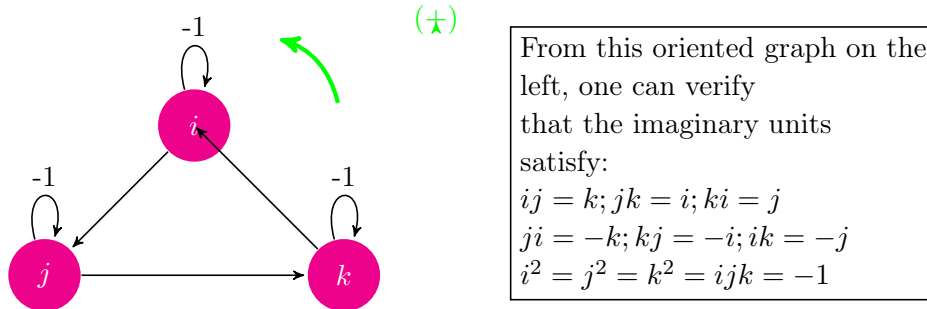
### 1.6.4 Applications

The matrix exponential is widely used in non-linear computational problems within dynamic systems like integrating first order Ordinary differential equations (ODEs), describing the time-dependant N-dimensional deformation field along a

diffeomorphic trajectory. This embedding of Lie algebra into a matrix algebra has been successfully employed in the context of medical image registration, yielding nice properties of the estimated deformations like smoothness and invertibility in addition to the invariance with respect to a change of coordinate system. In this context, *Arsigny et al.* [6] presented a general log euclidean polyaffine framework to fuse multiple local affine transformations. As a particular case, a polyrigid fusion can be performed using this framework if the local transformations are simply rigid (*e.g.* bone transformations).

## 1.7 Rotations and quaternions

Quaternions are hyper-complex numbers invented by an Irish mathematician, Sir William Rowan Hamilton [57] in 1843 as an extension of the classical complex numbers in  $\mathbb{C}$  in order to provide a more compact representation of rotations in the space. Quaternion algebra  $\mathbb{H}$  is associative but non-commutative over  $\mathbb{R}$ . Any quaternion number  $q \in \mathbb{H}$  can be written as:  $q = q_a + iq_b + jq_c + kq_d$ , where  $q_a \in \mathbb{R}$  is the real part,  $(q_b, q_c, q_d) \in \mathbb{R}^3$  are the three complex components of  $q$ , and  $\{1, i, j, k\}$  is a basis of  $\mathbb{H}$ .



A quaternion  $q = q_a + iq_b + jq_c + kq_d$  is called *unit quaternion* or *versor* if and only if its modulus  $|q| = \sqrt{qq^*} = \sqrt{q_a^2 + q_b^2 + q_c^2 + q_d^2}$  verifies  $|q| = 1$ , where  $q^* = q_a - iq_b - jq_c - kq_d$  is the conjugate of  $q$ . Unit quaternions can represent a rotation angle in  $\mathbb{R}^3$ . In fact, a unit quaternion can be decomposed into a scalar real part  $s = \text{Re}(q) = q_a$  and a vector part  $V = \text{Im}(q) = iq_b + jq_c + kq_d$  (also called *pure unit quaternion*), so that  $q = s + V$ , with  $s^2 + \|V\|^2 = 1$ . Hence,  $q$  can be written in the *polar* form:

$$q = \cos(\theta) + u.\sin(\theta) \quad (1.19)$$

where  $\theta \in [0, 2\pi]$  is the argument of  $q$  and  $u \in \mathbb{R}^3$  is the orientation vector.

Considering the following application:

$$\begin{aligned} \mathbb{H} &\rightarrow \mathbb{H} \\ P_2 &\mapsto qP_1q^* \end{aligned}$$

Then we obtain a rotation angle of  $2\theta$  and an axis  $u$  describing the orientation.

$$qP_1q^* = \begin{pmatrix} 1 & 0^T \\ 0 & R \end{pmatrix} \cdot \begin{pmatrix} p_1 \\ p_2 \\ p_3 \\ p_4 \end{pmatrix} \quad (1.20)$$

where:

$$R = \begin{pmatrix} q_a^2 + q_b^2 - q_c^2 - q_d^2 & 2(q_bq_c - q_aq_d) & 2(q_bq_d + q_aq_c) \\ 2(q_bq_c + q_aq_d) & q_a^2 - q_b^2 + q_c^2 - q_d^2 & 2(q_cq_d - q_aq_b) \\ 2(q_bq_d - q_aq_c) & 2(q_cq_d - q_aq_b) & q_a^2 - q_b^2 - q_c^2 + q_d^2 \end{pmatrix} \quad (1.21)$$

## 1.8 Contributions summary

In this thesis, we present the following contributions:

- **Spatio-temporal resolution reconstruction of the ankle joint from one high-resolution static scan and one low-resolution dynamic MRI sequence:** Chapter 2 will cover our recent developments on dynamic MRI and particularly the proposed intensity-based registration algorithm for skeleton tracking. The most challenging task is to find a link between static and dynamic MRI data. In fact, the required multi-resolution registration is prone to errors since the optimization of the similarity measure is prone to local minima problems. To tackle this problem, we decomposed the multi-resolution registration into two steps (a global rigid registration, followed by a local rigid registration) based on the fact that the registration process is much simpler to converge for transformations close to the identity.
- *Non-invasive* quantification of contact kinematics by accurately measuring 4D joint space width (JSW): our main contribution is the temporal tracking of the joint space section from the low-resolution dynamic sequences, while all our results are performed in the resolution of the static image. Furthermore, we developed an Eulerian PDE approach which was first dedicated for measuring the cortical thickness, characterized by its more complicated topology.
- **Enhancing the accuracy of the joint deformation fields, estimated via the Log Euclidean Polyaffine (or polyrigid) Framework:** the use of the scaling and squaring method for computing the principal matrix logarithm or the matrix exponential within the LEPF is prone to very small errors (rounding errors) as this technique involves approximation theory. This accumulative error may not be appreciated by the naked eye but it exists anyway.

Reducing this accumulative error can be appreciated for some sophisticated applications especially where the ROIs are very fine structures like the human brain cortex segmentation. For which it is always interesting to reduce the partial volume error.

- We have also investigated the combination of the linear registration tool `Fsl-flirt` [66, 67] with the LEPF to deal with non-linear dynamics of articulated structures. Since this framework allows for estimating smooth deformation fields by fusing a set of locally linear transforms. The main goal is to benefit from this robust linear registration tool to track bones since the LEPF generates smooth deformations independently of the way in which the local bone rigid transforms are first estimated. This contribution is explained in chapter 3.

Development of dynamic MRI techniques will enable investigations that require functional assessment of joints and surrounding tissues. Furthermore, these tools may be applicable to other joints and related musculoskeletal disorders.

## 1.9 Conclusion

In this chapter, we have introduced the mathematical tools that we have used for dynamic MRI data post-processing. From a mathematical point of view, the registration process aims to perfectly align between two images. However, there are some inevitable physical limitations like image resolution, motion artifacts and image noise which make each registration algorithm prone to a certain bias even if it works and sometimes prone to fail in the worst cases (e.g. local minima problem). In other words, such algorithms are always exposed to small errors that can be related to the optimization iterative process in it self or to the interpolation method. Unfortunately, these small errors will be mixed together making it difficult to separate between their origins given the resulting or warped image.

Talking about small registration bias, the use of the scaling and squaring method for computing the principal matrix logarithm or the matrix exponential within the LEPF is also prone to very small errors (rounding errors) as this technique involves approximation theory. This accumulative error may not be appreciated by the naked eye but it exists anyway.

Eliminating this accumulative error can be appreciated for some sophisticated applications especially where the ROIs are very fine structures like the human brain cortex segmentation. For which it is always interesting to reduce the partial volume error. **FSL-flirt** (FMRIB's Linear Image Registration Tool) is a fully automated robust and accurate tool for linear (affine/rigid) intra- and inter-modal brain image registration [66]. In this work, we have extended this tool to deal with non-linear image registration in the context of dynamical articulated structures. Although there exist different tools for non-linear or diffeomorphic image registration such as ANTs (Advanced Normalization Tools), they did not necessarily preserve bone shapes af-

ter the alignment process [1]. So we have preferred to fuse the flirt transformations by the log euclidean polyrigid framework.



# In vivo Ankle Joint Kinematics from Dynamic Magnetic Resonance Imaging using a Registration-based Framework

---

## Contents

---

<b>2.1</b>	<b>Introduction</b>	<b>33</b>
<b>2.2</b>	<b><i>In vivo</i> ankle joint biomechanics</b>	<b>34</b>
<b>2.3</b>	<b>Materials and methods</b>	<b>35</b>
2.3.1	Subject recruitment	35
2.3.2	Data Acquisition	35
2.3.3	Motion estimation	37
2.3.4	FSL-FMRIB's Linear Image Registration Tool: FSL-FLIRT	38
2.3.5	Computation of temporal dense deformation fields	40
2.3.6	Determination of ankle joint biomechanics	41
2.3.7	Method evaluation	42
<b>2.4</b>	<b>Results</b>	<b>43</b>
<b>2.5</b>	<b>Discussion</b>	<b>43</b>

---

## 2.1 Introduction

In this chapter, we propose a method for non-invasively measuring three-dimensional *in vivo* kinematics of the ankle joint from a dynamic MRI acquisition of a single range-of-motion cycle. The proposed approach relies on an intensity-based registration method to estimate motion from multi-plane dynamic MRI data. Our approach recovers not only the movement of the skeleton, but also the possibly non-rigid temporal deformation of the joint. First, the rigid motion of each ankle bone is estimated. Second, a four-dimensional (3D+time) high-resolution dynamic MRI sequence is estimated through the use of the log-euclidean framework for the

---

<sup>0</sup>This chapter is the subject of the publications [88] and [90].

computation of temporal dense deformation fields. This approach has been then applied and evaluated on *in vivo* dynamic MRI data acquired for a pilot study on six healthy pediatric cohort in order to establish *in vivo* normative joint biomechanics. Results demonstrate the robustness of the proposed pipeline and very promising high resolution visualization of the ankle joint.

## 2.2 *In vivo* ankle joint biomechanics

Musculoskeletal disorders and injuries of the ankle joint occur with considerable frequency in the pediatric population (such as equinus, ankle fractures). However, surgical intervention is rarely straightforward due to a lack of knowledge of joint and muscle biomechanics.

To better understand the biomechanics of the pediatric ankle joint, it is crucial to establish *in vivo* normative joint biomechanics [18] before focusing on pathomechanics studies. This approach would likely contribute to a better long-term follow-up for childhood disabilities such as cerebral palsy.

Conventional MRI techniques have been used for accurate diagnosis of the ankle and foot disorders given the complexity of their anatomy [10]. Dynamic MRI was originally developed to study cardiovascular functions towards the end of the 1980s [110]. Since then, MRI acquisition and reconstruction techniques have improved by leaps and bounds with current sequences such as Fast-PC MRI, ultrafast MRI, and Fast Field Echo FFE. These techniques have been successfully employed to quantify the knee joint kinematics [126, 20], and to analyze *in vivo* 3D musculoskeletal dynamics [13, 130], non-invasively. Sequences such as cine-PC MRI [106, 131] or fast-PC MRI [127, 116] can provide *in vivo* joint velocity field measurements. However, these data require long acquisition times with a high number of repeated cycles. Sequences such as ultrafast MRI [33] allow faster scan speed by exploiting spatio-temporal redundancy and can acquire images during a single cycle. However, they require slow motion of the joint making the movement quasi-static where no real functionality can be assessed. Thus, both these types of sequences are not appropriate to acquire dynamic *in vivo* data for children especially with musculoskeletal disorders. In this work, we use real-time FFE sequences [120] which are less sensitive to motion artifacts and which reduce the scanning time to 18 seconds to acquire the dorsi-plantarflexion cycle.

Furthermore, post-processing of acquired dynamic images remains a challenging task due to low resolution and motion artifacts. In [126], the displacement of specific points on each bone were quantified by integrating the velocity data using a three-dimensional Fourier tracking method [150]. However, motion tracking based on single-slice cine-PC data has limitations and the out of plane accuracy of the bone motion remained a challenge.

Clarke *et al.* [33] determined *in vivo* muscle moment arms during ankle movement using a 3D mesh-based registration method. They estimated bone motions by registering the high-resolution joint geometry from MRI scans of the stationary joint to

low-resolution geometries from ultrafast MRI scans of the slowly moving joint. However, in addition to the segmentation of the high-resolution static scan, it was needed to manually segment each low-resolution time-frame which was time-consuming and prone to segmentation bias.

The combined use of high-resolution static data and low resolution dynamic data is thus limited in the literature. In this study, the spatial information of the high-resolution static MRI data and the temporal information of the dynamic data were combined using a log-euclidean polyrigid framework (*LEPF*). The purpose of this study was twofold: 1) to estimate bone motion, allowing to derive the 3D kinematics of the joint, 2) to compute temporal dense deformation fields of the joint, allowing to reconstruct a high-resolution dynamic MRI sequence from a low-resolution dynamic MRI sequence and one high-resolution MR image.

The use of the *LEPF* proposed by *Arsigny et al.* [7, 6, 5] has been investigated for registration of structures such as the hip and knee joint in mouse CT images [104], human hands from 2D hand radiographs [92], bones in lower-abdomen area [35], and also intra-subject mandible 3D datasets [122]. In this work, we adapted this framework to deal with 4-dimensional MRI data by proposing a fast and accurate algorithm to compute the dense deformation fields in regular grids. In fact, we propose to compute the exponential mapping of the *LEPF* using matrix eigendecomposition instead of the scaling and squaring method used in the literature [5, 35].

## 2.3 Materials and methods

### 2.3.1 Subject recruitment

Six typically developing children with a mean age of 12 years and with a mean weight of 35.8 kg participated in this study which was approved by the regional ethics committee. Children were selected with no contraindications to MRI and with no history of lower limb musculo-skeletal injury or surgery in the past six months. MRI data were acquired in a single visit after parents signed informed consent forms.

### 2.3.2 Data Acquisition

MRI data have been acquired using a 3T MR scanner (Achieva dStream, Philips Medical Systems, Best, Netherlands). An MRI-compatible orthotic fixture was used to perform dynamic movements inside the scanner (Figure 2.1). Individual range-of-motion was checked by the clinician outside the MRI scanner and stops were placed on wire guides for controlling the range-of-motion inside the scanner. Each dynamic scan lasted for 18 seconds and ankle joint was moved (actively or passively) through the range-of-motion for each subject within 18 seconds with a rotation speed of  $4^\circ/s$  to  $5^\circ/s$  (depending on the range). Both passive and active acquisitions were standardized for all subjects as detailed below. Dynamic images were

acquired in the oblique axis of the ankle motion. This was done by acquiring axial dynamic scans first and then obliquely orienting the scanning plane for images to be acquired in sagittal plane. For passive acquisition, after placing the ankle joint in the fixture, each child was asked to relax the lower-limb musculature and then the fixture was cyclically moved by a technician. The technician was given a set of headphones through which he/she could hear a metronome. Fixture was then moved in a consistent passive plantar-dorsiflexion by the technician at the beat of the metronome and using the guide wires attached to the fixture. For active movement, no technician was present and children were asked to perform voluntary plantar-dorsiflexion between the extreme positions on the beat of the metronome. Meaning, the active motion was completely voluntary with all the muscles dynamically taking part in the production of the plantar-dorsiflexion movement. Rotation speed was kept approximately the same as for passive motion. The scanning protocol included one high-resolution static 3D scan of the ankle joint with a resolution of  $0.26 \times 0.26 \times 0.8mm$  (T1-weighted gradient-echo, flip angle 10, matrix 576576, FOV 150mm150mm, TR/TE 7.81/2.75 ms, mean acquisition duration: 424.32 s), and three low-resolution dynamic sequences per child: two passive sequences for repeatability measures and one active sequence, all acquired with knee angle kept at full extension (approximately between  $0^\circ$  to  $10^\circ$ ). Each sequence is composed of 15 time frames with a voxel size of  $0.57 \times 0.57 \times 8mm$  (flip angle  $15^\circ$ , matrix 352352, FOV 200mm200mm, TR/TE 20.61/1.8 ms, acquisition duration: 18.98 s).

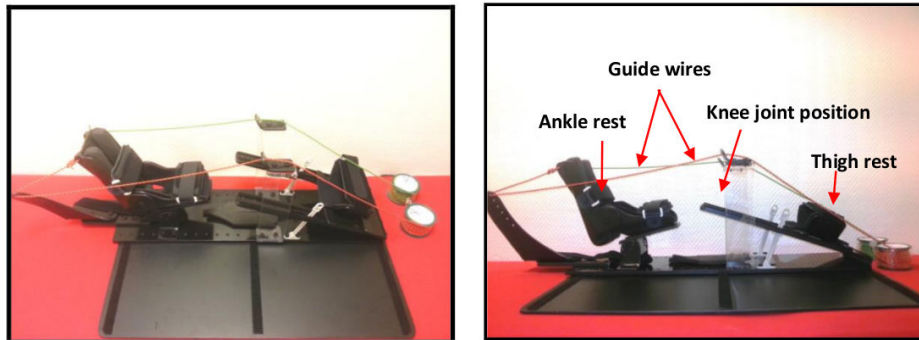


Figure 2.1: Orthotic fixture specially designed to acquire MRI data on pediatric ankle joint. The entire fixture is made out of MRI-compatible material. Guide wires helped the technician to control and operate the passive plantar-dorsi flexion movements of the ankle joint while rest of the limb is fixed using straps at foot, tibia and mid thigh locations. Position of the ankle rest can be adjusted based on the limb length. Knee angle can be adjusted from full extension to  $45^\circ$  flexion. Cushioned ankle rest supports the foot to be imaged.

### 2.3.3 Motion estimation

Temporal tracking of the ankle bones is a challenging task because of nonlinearly articulated joint motion. Image registration is an *iterative* process maximizing a similarity measure or minimizing a distance between two images (source and target) in order to find the optimal geometric transformation that best align them. In this work, we used a locally-linear intensity-based registration method to estimate bone motion, and then we fused these local transformations to compute temporal dense deformation fields. The bones of interest were manually segmented in the high-resolution static image (Figure 2.2) and then automatically propagated throughout the dynamic low-resolution sequence using intensity-based registration.

Each high-resolution static image of the dataset was manually segmented to extract accurate region of interest of the three bones considered in this work (see Figure 2.2). In order to take into account the partial volume effect due to anisotropy of the image resolution, a Gaussian blur with a standard deviation set to 2 voxels has been applied onto each bone mask.

The proposed approach for motion estimation consisted in two steps: 1) estimating a mapping for each bone between static MRI data and dynamic sequences, 2) estimating the relative bone motions using the dynamic sequence.

**step1:** The first step was to compute the transformations from the static image to the dynamic images. More precisely, we estimated a rigid transformation for each bone between images that underwent non-rigid deformations. In order to make this step robust, the multi-resolution registration was carried out in two steps: *First*, the static image was globally (and rigidly) registered to each low-resolution time frame  $\{D_k\}_{k \in 1 \dots K}$ . This provided a set of rigid transforms  $\{T_{S \rightarrow D_k}\}_{k \in 1 \dots K}$ .

*Second*, initialized with the set of global rigid transforms  $\{T_{S \rightarrow D_k}\}_{k \in 1 \dots K}$ , the temporal position of each bone was refined thanks to a local rigid registration using bone masks. In this step, the static image is registered to each dynamic image  $\{D_k\}_{k \in 1 \dots K}$  using input weights on each of the bones separately. This provided another set of rigid transforms  $\{T_{S \rightarrow D_k}^i\}_{k=1, \dots, K}^{i=1, \dots, 3}$ .

However, although the fact that the alignment process was divided into two registrations, it is not always guaranteed to avoid misregistration issues caused by local minima in the similarity measure which frequently occurred for time frames representing big deformations of the joint (for bone-dependent registrations in most of cases). To maximize the robustness of the algorithm, an image  $D_{k^*}$  from the dynamic sequence whose the content is the closest to the static image, was automatically detected. The underlying assumption is that the registration process is much simpler to converge for transformations close to the identity. To this end, the image of the sequence for which the overlap between regions of interest before and after bone-dependent registration was maximum, was selected as the reference image which served as a starting point for the motion estimation within the dynamic sequence.

**step2:** The second step focused on the estimation of bone motion during the dynamic sequence. To do this, we proposed to take advantage of the temporal

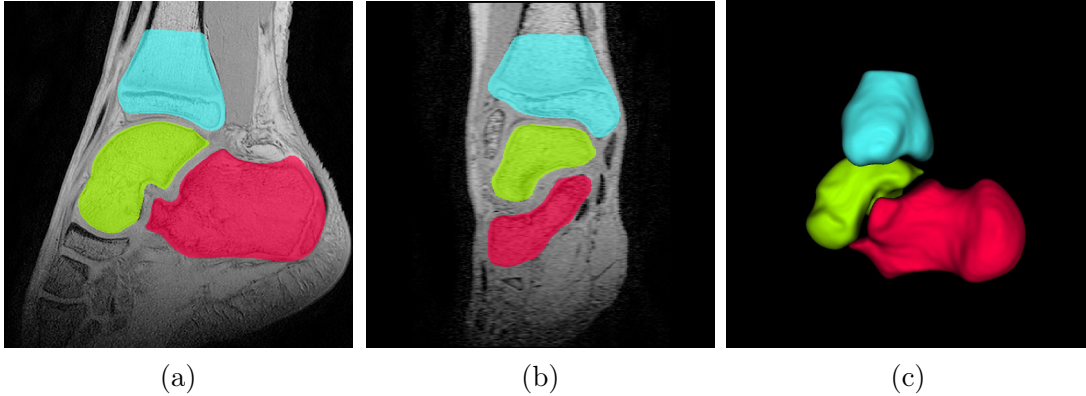


Figure 2.2: Bones of interest: calcaneus (red), talus (green) and tibia (cyan). (a): Mid-sagittal image from the high-resolution static scan; (b): Mid-coronal image from the high-resolution static scan ; (c): Three dimensional rendering of segmented bones.

regularity of the data by propagating the bone masks in the dynamic sequence. For each bone, a rigid transform was estimated between successive images. *i.e.* local and rigid registrations were conducted from the reference image  $D_{k^*}$  towards first and last images of the sequence. To go forward and backward in time, only one interpolation was needed to propagate segmentation from  $D_{k^*}$  to each time frame  $D_k$  by composing a set of successive rigid transforms in order to avoid the propagation of interpolation errors as much as possible. Temporal bone rotations were optimized based on their quaternion representations [101], making the segmentation propagation more accurate and robust.

Bone transformations are estimated using the linear registration tool FSL-FLIRT (described in section 2.3.4). The overall algorithm for bone motion estimation is described in Algorithm 1, using the following notations:  $S$  is the high-resolution static image,  $\{D_k\}_{k=1,\dots,K}$  is the set of low resolution dynamic images,  $\{M^i\}_{i=1,\dots,N}$  is the set of mask of bones of interest,  $T_{A \rightarrow B}$  is the rigid transform from image  $A$  to image  $B$ ,  $T_{A \rightarrow B}^i$  is the rigid transform from image  $A$  to image  $B$  for the bone  $i$ ,  $Dice(A,B)$  is the DICE coefficient which measures the overlap between segmented regions ( $Dice(A,B) = \frac{2|A \cap B|}{|A| + |B|}$ ).

### 2.3.4 FSL-FMRIB’s Linear Image Registration Tool: FSL-FLIRT

FSL-FLIRT is a robust linear registration tool proposed by *Jenkinson et al.* [66] in the context of brain MRI registration (for estimating affine and rigid transformations). This tool is characterized by its lower sensitivity to local minima problems during the optimization step. Avoiding the local minima is addressed in two principal ways:

- A general apodization of the cost function is proposed to eliminate small dis-

**Algorithm 1** Bone motion estimation

**Input:** segmentation of bones of interest in  $S$ .

**Mapping estimation from  $S$  to  $\{D_k\}$ :**

- Estimate rigid transforms  $\{T_{S \rightarrow D_k}\}_{k=1, \dots, K}$
- Estimate rigid transform  $\{T_{S \rightarrow D_k}^i\}_{k=1, \dots, K}$  using bone mask  $M^i$ , initialized with  $\{T_{S \rightarrow D_k}\}_{k=1, \dots, K}$
- Select  $D_{k^*}$  in  $\{D_k\}_{k=1, \dots, K}$  such that  $k^* = \underset{k}{\operatorname{argmax}}(\prod_{i=1}^N \operatorname{Dice}(T_{S \rightarrow D_k}(M^i), T_{S \rightarrow D_k}^i(M^i)))$

**Motion estimation:**

- Estimate forward successive rigid transforms  $\{T_{D_k \rightarrow D_{k+1}}^i\}_{k = k^*, \dots, K-1; i=1, \dots, N}$ .
- Estimate backward successive rigid transforms  $\{T_{D_k \rightarrow D_{k-1}}^i\}_{k = k^*, \dots, 2; i=1, \dots, N}$ .

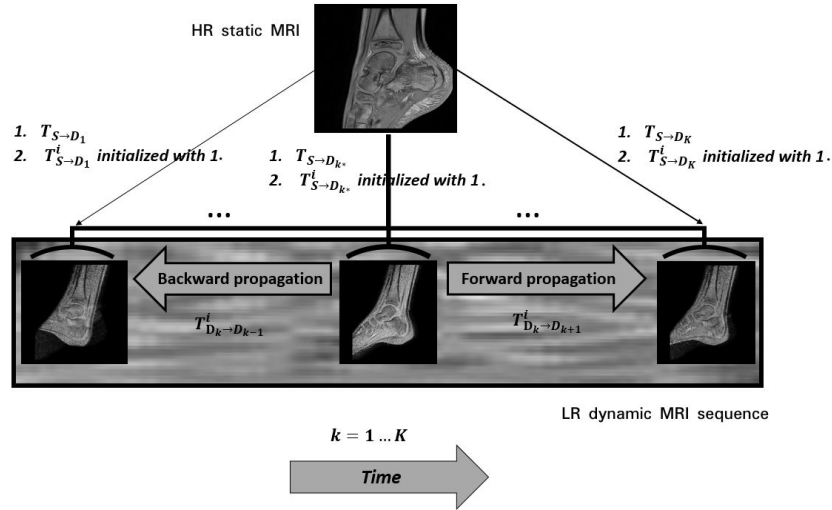


Figure 2.3: Proposed pipeline for ankle motion estimation: Bones of interest are segmented in the high-resolution static image. This high-resolution MR image is globally (and rigidly) registered to each MR image of the dynamic sequence (1.), and the position of each bone is refined thanks to a local rigid registration using bone segmentations (2.). This allows to identify the dynamic MR image which is closest to the high resolution image and which will serve as a starting point for the motion estimation within the dynamic sequence. Last, local and rigid registrations are conducted from the reference towards the sequence first and last images.

continuities of the number of voxels in the overlapping FOV, which occurs when changing the parameters of the transformation model to maximize the similarity measure.

- An hybrid global-local optimization method is proposed where the initial global search phase is based on a prior knowledge of the problem itself (*e.g.* size of the brain).

Local minima problems occur frequently in multi-resolution registration, which is the case for bone registration between static and dynamic MRI. Consequently, our choice of FSL-FLIRT for performing bone registrations is motivated by the fact that this tool is very efficient especially in the case of multi-resolution rigid registration.

Moreover, FSL-FLIRT uses a customised global optimisation technique that operates over multiple resolutions, which makes it suitable for registering bones from T1-weighted sequences with good contrast between structures.

### 2.3.5 Computation of temporal dense deformation fields

A dense deformation map of the joint from the static to each time frame was obtained by fusing rigid transforms corresponding to the bones of interest. For each bone, a non-negative weighting function was computed based on a distance to the mask [34]. Each weighting function reflects the local influence of the rigid transform of each bone. For each voxel  $x$ , the weighting functions were computed as follows:

$$w_{D_k}^i(x) = \frac{1}{1 + dist^2(x, M_{D_k}^i)} \quad (2.1)$$

where:  $dist(x, M_{D_k}^i)$  is the Euclidean distance between the point  $x$  and the mask of the bone  $i$  propagated onto the dynamic image  $D_k$ .

Given a point  $x$  in the high-resolution static image, the target location of this point in the dynamic image  $D_k$  can be computed with the following equation [7]:

$$\mathcal{T}_{S \rightarrow D_k}(x) = \exp \left( \sum_{i=1}^N \tilde{w}_{D_k}^i(x) \log(T_{S \rightarrow D_k}^i) \right) \cdot x \quad (2.2)$$

where  $\mathcal{T}_{S \rightarrow D_k}$  is the dense *invertible* deformation field from the static image  $S$  to the dynamic image  $D_k$ ,  $\tilde{w}_{D_k}^i$  is a normalized weighting function (*i.e.*  $\sum_{i=1}^N \tilde{w}_{D_k}^i(x) = 1, \forall x \in D_k$ ).

#### 2.3.5.1 Fast computation of dense deformation fields

In this section, we describe an efficient algorithm to compute deformation fields in dense regular grid based on the algebraic properties of the Log-Euclidean polyrigid framework. In [6, 5], the matrix exponential was recursively *approximated* with a certain level of accuracy using the *scaling and squaring* method by taking into account that the matrix exponential is much simpler to compute for matrices close to zero via the Pade approximant. In this work, we computed the exponential mapping of equation 2.2 *exactly* using eigen decomposition. Assuming the log-euclidean mean of linear transformations  $L(x) = \sum_{i=1}^N \tilde{w}_{D_k}^i(x) \log(T_{S \rightarrow D_k}^i)$  to be *diagonalizable* (*i.e.*  $L(x)$  can be expressed in the *Lie Algebra*  $se(3)$  as:  $L(x) = P.D.P^{-1}(x)$ , where the

columns of  $P$  contain the eigenvectors  $\{v_k(x)\}_{k \in \{1..4\}}$  corresponding to the complex eigenvalues of  $L(x)$ ,  $\{\lambda_1(x), \lambda_2(x), \lambda_3(x), \lambda_4(x) = \log(1) = 0\}$ , we broadcasted the exponentiation of transformation eigenvalues over all grid points using the following Equation:

$$e^{L(x)} = P e^D P^{-1}(x) = P \begin{pmatrix} e^{\lambda_1} & 0 & 0 & 0 \\ 0 & e^{\lambda_2} & 0 & 0 \\ 0 & 0 & e^{\lambda_3} & 0 \\ 0 & 0 & 0 & 1 \end{pmatrix} P^{-1}(x) \quad (2.3)$$

### 2.3.6 Determination of ankle joint biomechanics

#### 2.3.6.1 Definition of anatomically based coordinate systems

Anatomical coordinate systems  $\{R_i\}_{i=1, \dots, N}$  were defined on each bone in the high-resolution image  $S$  following the same protocols used in [129] as illustrated in Figure 2.4, and then mapped into the neutral position  $D_n$  using the estimated local-rigid transforms  $\{T_{S \rightarrow D_n}^i\}_{i=1, \dots, N}$ . The neutral dorsi-plantarflexion position was defined at an ankle angle of  $90^\circ$  as recommended by the ISB standards committee [143]. However, the above defined neutral position cannot be always achieved during dynamic scanning. Therefore, the image in which the foot position was closest to a dorsi-plantarflexion position of zero degrees was selected as the neutral position.

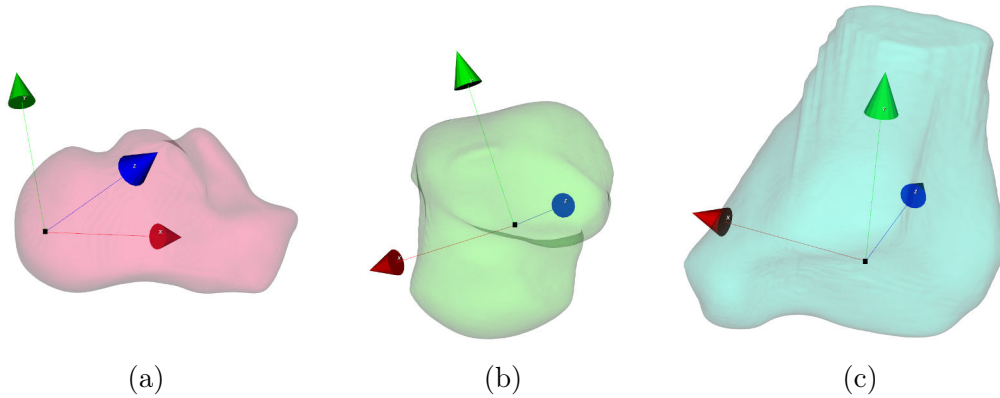


Figure 2.4: Anatomical coordinate systems for one subject's calcaneus (a), talus (b), and tibia(c) as per ISB.

#### 2.3.6.2 Quantification of ankle joint kinematics

In this study, the kinematics were defined through the 3D registration of the entire bone volume. More precisely, rotations and translations of each bone  $i$  were determined from estimated rigid transforms  $\{T_{D_k \rightarrow D_{k+1}}^i\}_{i=1, \dots, N}$ . Ranges of motion were estimated using low-resolution image data on multiple dynamic images (15 ankle

positions). Kinematics of talocrural joint, subtalar joint, and calcaneal-tibial complex were then derived from  $\{T_{D_k \rightarrow D_{k+1}}^i\}_{i=1, \dots, N}$ .

Given the image coordinate system  $R_I = (O, \vec{x}, \vec{y}, \vec{z})$ , we defined the transformation,  $M_{R_I \rightarrow R_j}$ , that mapped  $R_I$  to an anatomical bone-based coordinate system  $R_j = (O^j, \vec{x}^j, \vec{y}^j, \vec{z}^j)$ . This transformation changed a representation from the  $R_j$  system to the  $R_I$  system.

Individual bone transformation matrices expressed in  $R_I$  were then converted into the transformation matrices expressed in the new anatomical coordinate systems  $R_j$  as follows:

$$T_j^i(k) = (M_{R_I \rightarrow R_j} \times T_{D_k \rightarrow D_{k+1}}^i \times M_{R_I \rightarrow R_j}^{-1})_{k=1, \dots, K-1; i=1, \dots, N; j=1, \dots, N} \text{ where:}$$

- $T_j^i(k)$ :  $4 \times 4$  rigid transformation matrix of the  $i^{\text{th}}$  bone relative to the  $j^{\text{th}}$  local bone coordinate system at time  $k$ .
- $M_{R_I \rightarrow R_j}$ : the change of basis matrix.

Example:

change of basis matrix to convert the  $i^{\text{th}}$  coordinate system  $R_i = (O^i, \vec{U}^i, \vec{V}^i, \vec{W}^i)$  to the image coordinate system  $R_I = (O, \vec{x}, \vec{y}, \vec{z})$ :

$${}^j_I M = \begin{pmatrix} U_x^j & V_x^j & W_x^j & O_x - O_x^j \\ U_y^j & V_y^j & W_y^j & O_y - O_y^j \\ U_z^j & V_z^j & W_z^j & O_z - O_z^j \\ 0 & 0 & 0 & 1 \end{pmatrix} \quad (2.4)$$

For more details about the definition of  $\vec{U}^j$ ,  $\vec{V}^j$  and  $\vec{W}^j$  from MRI scans, the reader is referred to [129]. For each subject, image origin  $O$  and bone origins  $\{O^j\}_{j=1, \dots, N}$  were expressed in  $mm$ .

Note that image and bone origins were expressed in  $mm$ .

### 2.3.7 Method evaluation

To evaluate the proposed registration approach for bone motion estimation, the propagated mask of each bone through the dynamic sequence was compared with a manually delineated bone on each time frame. The accuracy of the estimations of the successive rigid transforms was assessed by computing the DICE coefficient  $Dice(B_k^i, B_{m_k}^i)$  and the RMS error  $RMSE(B_k^i, B_{m_k}^i)$  where  $B_k^i$  was the propagated mask of the bone  $i$  on dynamic image  $D_k$  and  $B_{m_k}^i$  was a manually delineated mask of the same bone on the dynamic image  $D_k$ . A DICE value close to one indicates that the bone masks have been well propagated through the entire dynamic sequence. RMS error was computed as follows:

$$RMSE(B_k^i, B_{m_k}^i) = \sqrt{1/n_c \cdot \sum_{x_c=1}^{n_c} dist^2(x_c, \zeta_{B_k^i})}$$

where  $n_c$  is the total number of voxels of ground-truth contours (i.e. contours of  $B_{m_k}^i$ ) and  $dist(x_c, \zeta_{B_k^i})$  is the Euclidean distance between  $x_c$  and the contour of  $B_k^i$ .

## 2.4 Results

Results on bone motion estimation were reported in Figures 2.9-2.10 for the six subjects of the pilot study. Results for passive and active motion were separated. In most of the cases, the DICE coefficient was greater than 0.8 and the RMSE was smaller than 0.6 indicating accurate propagations of bone masks over the dynamic sequence, for both passive and active motions.

From the set of rigid transforms of each bone over the dynamic sequence, it was then possible to compute temporal dense deformation fields to synthesize a high-resolution dynamic MRI sequence. Using the fast computation technique described in Section 2.3.5.1, a dense deformation field was computed in *3min* on an Intel<sup>®</sup> Xeon<sup>®</sup> Processor E3-1271 v3 3.60 GHz on a  $576 \times 576 \times 90$  regular grid and in *15min* on a very high dimensional space ( $576 \times 576 \times 202 \simeq 67$  million deformation vectors) which required a high capacity RAM because computations were performed in the complex domain for the purpose of enhancing the accuracy. Figure 2.11 illustrates, for one subject (A6), such high-resolution reconstructed data.

Three-dimensional kinematics of the joint under both active and passive ankle dorsi-plantarflexion movement using the current 3D dynamic MRI method were presented in Figures 2.6 to 2.8.

Kinematics of all ankles (except A5) were derived from the estimated temporal rigid transforms of each bone of interest, converted into the matrices of the calcaneus relative to the tibia, the talus relative to the tibia, and the calcaneus relative to the talus. The talus mistracking for the ankle A5 was caused by the considerable missing portion from the bone in intermediate time frames due to the inappropriate initial placement of the flex coils.

The mean rotation about the Inferior-Superior and about the Posterior-Anterior axes (averaged across time for all subjects) was close to 0 degrees for both active and passive motion. The mean range of passive rotation about the Medial- Lateral axis for talocrural and calcaneal-tibial joints was between  $-11$  degrees of maximal dorsiflexion and  $+32$  degrees of maximum plantarflexion with full extended knee. This demonstrates excellent correspondance with the mean range of passive rotation reported in [3] and validated for 245 healthy children between 7 and 14 years old.

## 2.5 Discussion

In this study, we have presented a method to determine full 3D-kinematics of the ankle joint from dynamic anatomical MRI data. An intensity-based registration pipeline has been proposed to estimate bone motion through the dynamic sequence. The robustness of this approach for both passive and active motion has been evaluated on *in vivo* data acquired for a pilot control cohort study. Although based on a successive estimation of transformations, the proposed approach demonstrates advantages in efficiency, reliability and robustness for all subjects.

The proposed algorithm is robust enough to image quality as well as motion

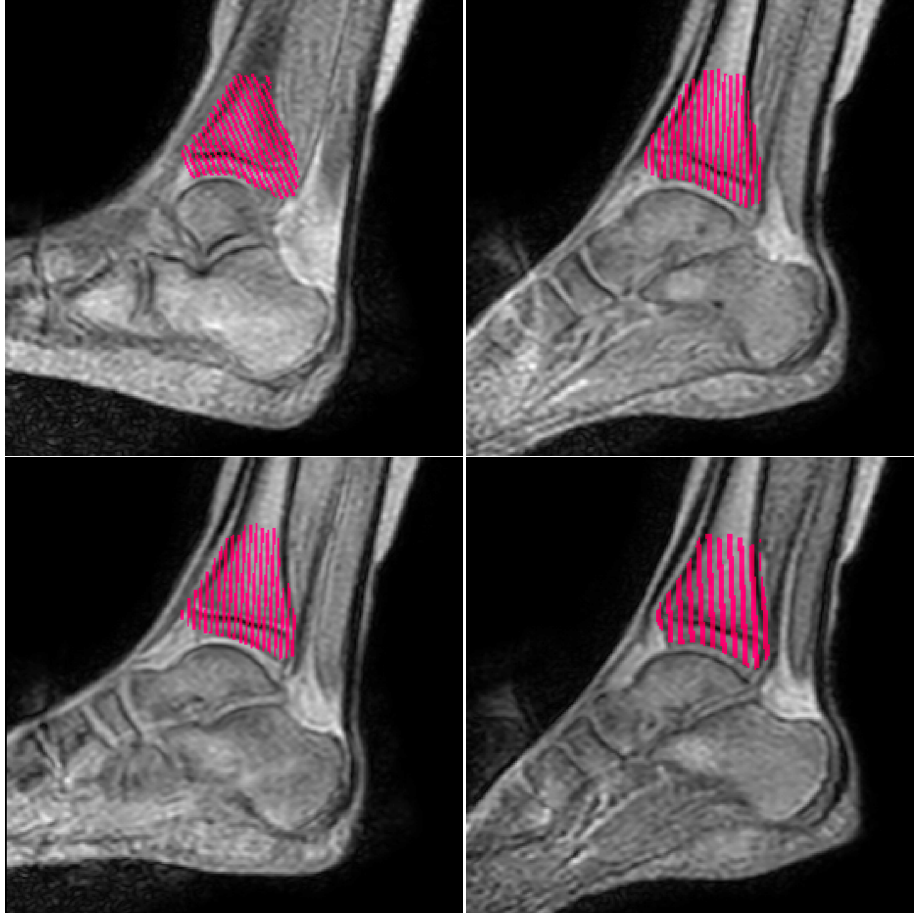


Figure 2.5: Tracking of the tibia for one subject using Algorithm 1, only one out of two slices has been segmented in the static image (*i.e.*, spatial resolution reduction).

artefacts in a way that it can determine kinematics even for unconstrained motion. This was evaluated by changing the delta-time  $\Delta k$  separating each couple of source/target images during the successive rigid registrations and the algorithm is still robust even for  $\Delta k = 5$ . Furthermore, the proposed motion estimation algorithm works well even if only one out of two slices is segmented in the high-resolution static image as shown in Figure 2.5.

It can be noticed that the proposed approach can be used for both passive and active motion of the ankle joint. Normative passive kinematics show that the subjects maintained a consistent movement trajectory. This is an expected consequence knowing that the joint was moved in a consistent plantar-dorsiflexion cycle. Three-dimensional kinematics of the joint under passive ankle movement using the proposed method (Figures 2.6 to 2.8) were similar to ankle joint kinematics reported in other studies using velocity data [129]. Normative active kinematics show that the subjects were able to perform voluntary plantar-dorsiflexion between the extreme positions with the same temporal regularity as for passive motion. The

comparison between passive and active kinematics shows closest temporal averages despite some temporal fluctuation of the standard deviation across subjects. Consequently, it appears that the range of motion of ankle in healthy children is extremely variable in terms of rotation and translation. Ankle dorsiflexion is restricted by a contracted gastrocnemius muscle with the knee extended [60] ( $-11$  degrees of maximal dorsiflexion). The proposed workflow is a brute force registration approach, with the static image rigidly registered to all dynamic (globally then locally refined). And the best registration selected (based on minimal local bone change). This then provides bone labels for all the dynamic scans. Then given the segmentations, the spatial-temporal model is built based on the log-euclidean fusion of rigid transformations.

Although the fact that both our method and other motion methods tend toward the same goal which is bone motion tracking, there are some technical differences making it difficult to perform an objective comparison based on a common error parameter.

In [33], the authors were more interested in the Achilles tendon moment arms and the accuracy and precision of bone motion tracking were not reported. Clarke et al. [33] have discussed some limitations in their methods which can be particularly useful in adults. They have explicitly mentioned that their protocols require some modifications to be useful in the smaller joints of children. To satisfy the mesh density requirements for using the ICP algorithm, they have recommended the reduction of the slice gap for the dynamic scanning protocol while increasing the number of slices per time frame so that the slices span the joint width. However, assuming that they have used ultrafast MRI sequences (with 8 sagittal slices/time frame compared to 6 slices in our work, and taking around 2 min to acquire 10 to 20 time frames compared to only 18 sec to acquire 15 time frames in our work), increasing the number of slices will increase the scanning time of dynamic data to more than 2 min which will be uncomfortable especially for the pathological subjects. The authors have also notified that the rotation speed for their study was slow (mean 1/s compared to 4.2/s in our work) in order to reduce the effects of motion artifacts, so the motion itself is reduced to almost static or quasi-static nature where no real functionality can be assessed. Our choice for FFE sequences for dynamic data acquisition was motivated by the fact that these techniques are less sensitive to motion artifacts [134] and more than 5 times faster than ultrafast MRI.

In the work of Sheehan *et al.* [129], the displacements of three to five points on each bone were calculated through Fourier integration and then converted into three-dimensional orientation angles. As part of the tracking process, they identified a series of vertices, defining regions on each bone of interest in the first time frame (i.e. three to five vertices per bone). The distance between these vertices in the first time frame was considered the absolute distance under the assumption that it should remain fixed throughout the movement because bones are rigid. Thus, for each bone, the difference in distance between vertices in each time frame relative to the absolute distance was defined as the tracking error. A potential limitation

of this study [129] was the out of plane accuracy of the bone motion because the accuracy of cine-PC MRI is independent of the shape of the bone being tracked [13]. Another clinical limitation is that subjects with musculoskeletal disease who cannot complete a large number of repeated motions cannot be studied with cine-PC MRI techniques. Although the vertices were well-defined from 3D high-resolution adult data in previous work of Sheehan *et al.* [129], it was hard to reproduce their exact locations from developing children data for comparison purposes because of the differences in bone size and topology between children and adults. From another point of view, it was not sufficient to consider the distance between only some vertices as system bias and thus we have considered all the bone segmentations (*i.e.* all the volumetric information) for method evaluation.

The proposed method remains robust as long as the field-of-view (FOV) is well adjusted (*i.e.* when the FOV covers either the full or nearly-full anatomy of the ankle bones throughout the entire joint trajectory).

We have also extended the log-euclidean framework to estimate temporal dense deformation fields from multiple rigid transforms. The polyrigid approach provides a way to combine high resolution spatial information with temporal dynamics of joints. The output of this process is a series of high-resolution anatomical images portraying the different phases of the movement cycle. In this context, we proposed to compute the exponential mapping of the LEPF in an efficient and elegant way using matrix diagonalization-based techniques rather than using techniques involving approximation theory. The preservations of the bone shapes after the polyrigid fusion were checked by computing the Jacobian maps associated to the estimated deformation fields (as shown in figure 3.5).

To conclude, we strongly believe that our work is the first effort to track ankle joint motion and deformation from volumetric image data using intensity-based non-rigid image registration rather than using explicit mechanistic models. It therefore achieves its goals without having to perform time-consuming manual segmentations. In immediate future, the proposed approach will be applied to compare the ankle joint dynamics of children with spastic equinus with age-matched healthy children. Since spastic equinus was typically defined as the inability to dorsiflex the foot above plantigrade, with the hindfoot in neutral position and the knee in extended position [72], the foot was constrained to a specific path using the fixture. However, this set-up is problem-specific and can be changed or removed while evaluating the pathomechanics of other joint(s). We will also explore this method to extract fine biomechanical parameters of tendon, and cartilage contact mechanics (*e.g.* temporal joint space width) of the tibio-talar joint which is the primary joint responsible for plantarflexion and dorsiflexion of the ankle. Furthermore, these techniques can be applied to other joints and related musculoskeletal disorders. This suggests that anatomical dynamic MRI and dedicated image processing techniques can open a new way to study in vivo human joints.

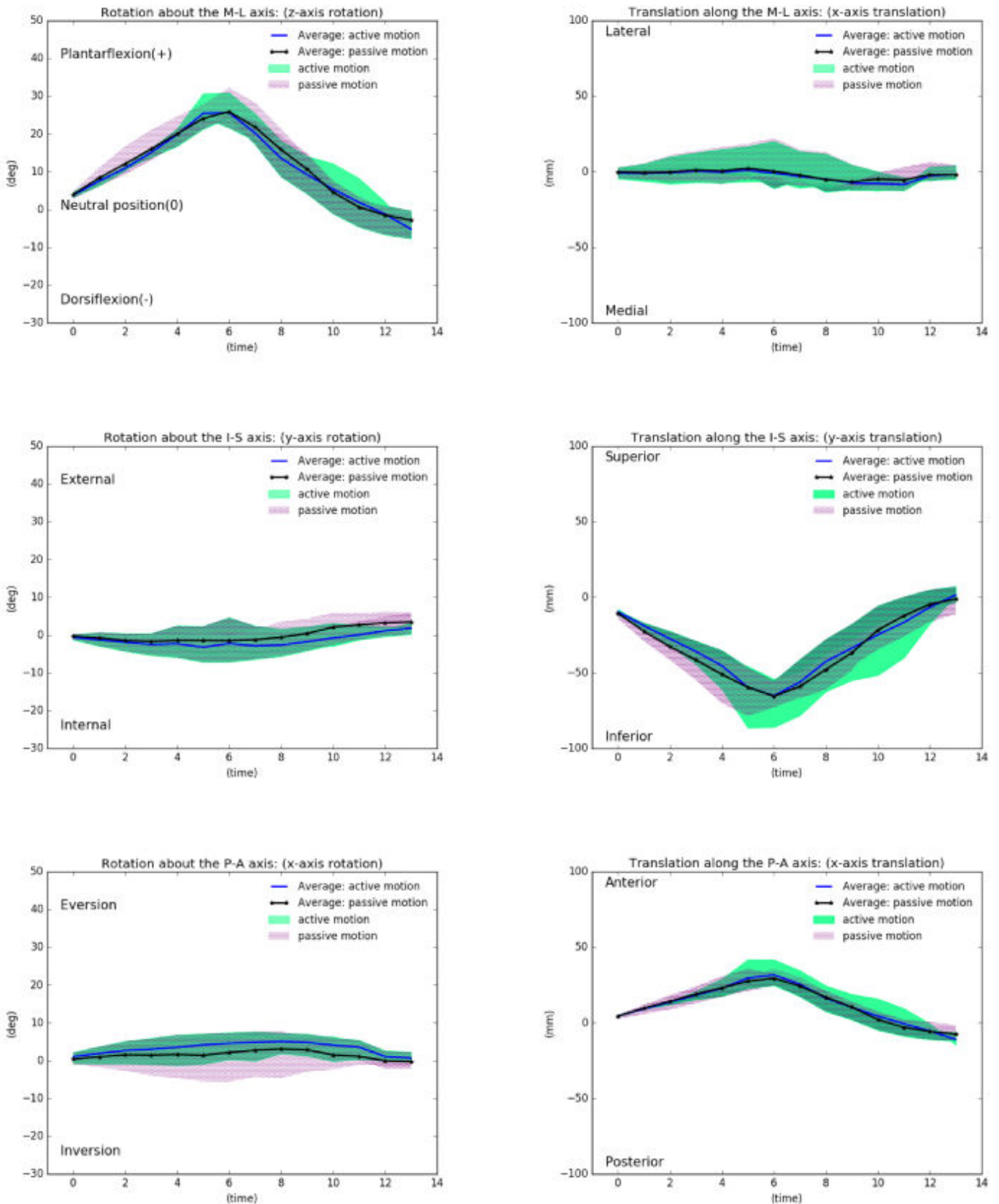


Figure 2.6: 3D normative kinematics of the calcaneal-tibial complex using the proposed image processing method. The kinematics of the calcaneus are represented relative to the tibial coordinate system defined in neutral position. Average rotation and translation were computed for both passive and active motion for the studied ankles. Standard deviation above and below the average line are shown (dotted shaded area for passive motion and green shaded area for active motion).

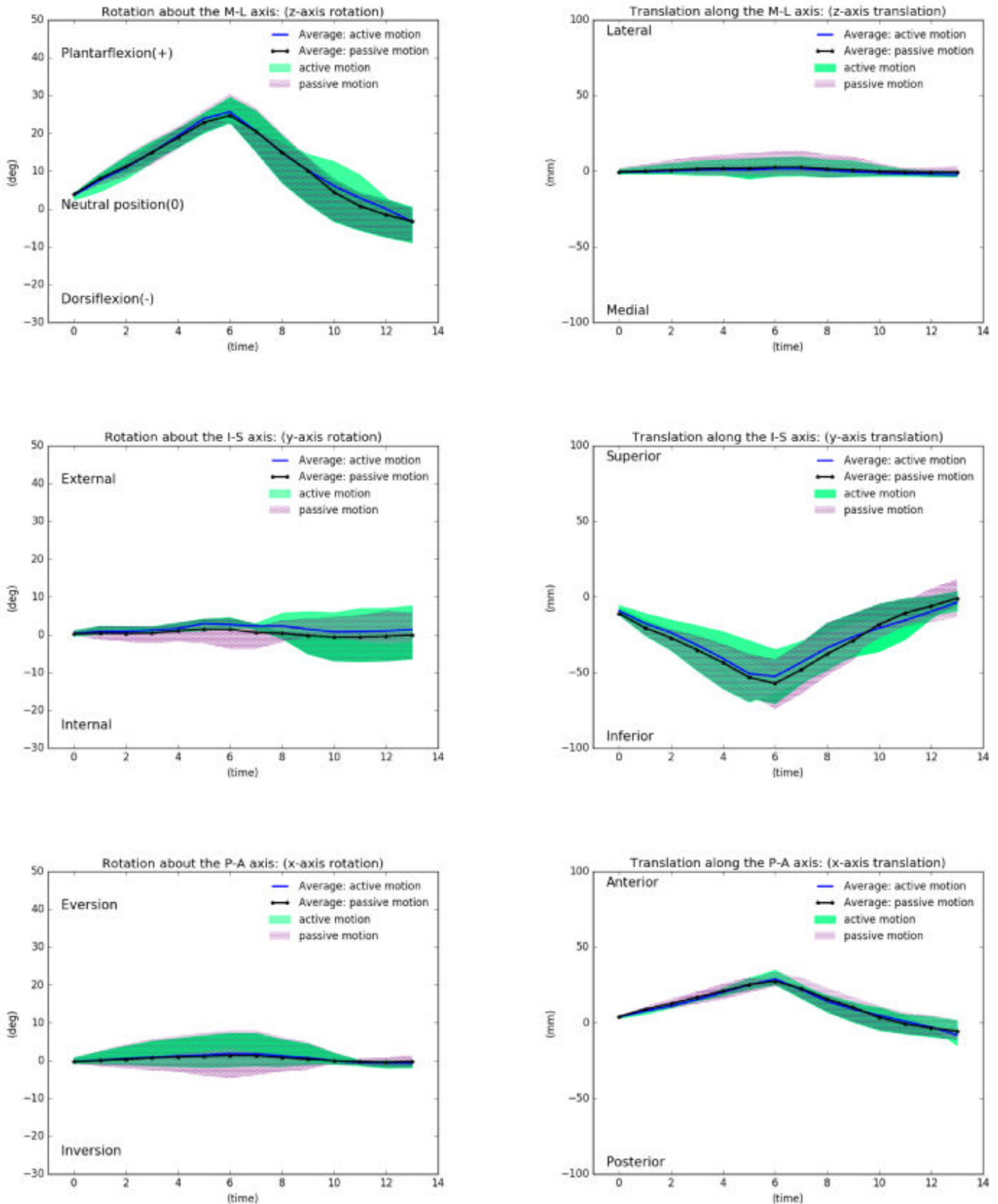


Figure 2.7: 3D normative kinematics of the talocrural (talar-tibial) joint using the proposed image processing method. The kinematics of the talus are represented relative to the tibial coordinate system in neutral position. Average rotation and translation were computed for both passive and active motion for the studied ankles. Standard deviation above and below the average line are shown (dotted shaded area for passive motion and green shaded area for active motion).

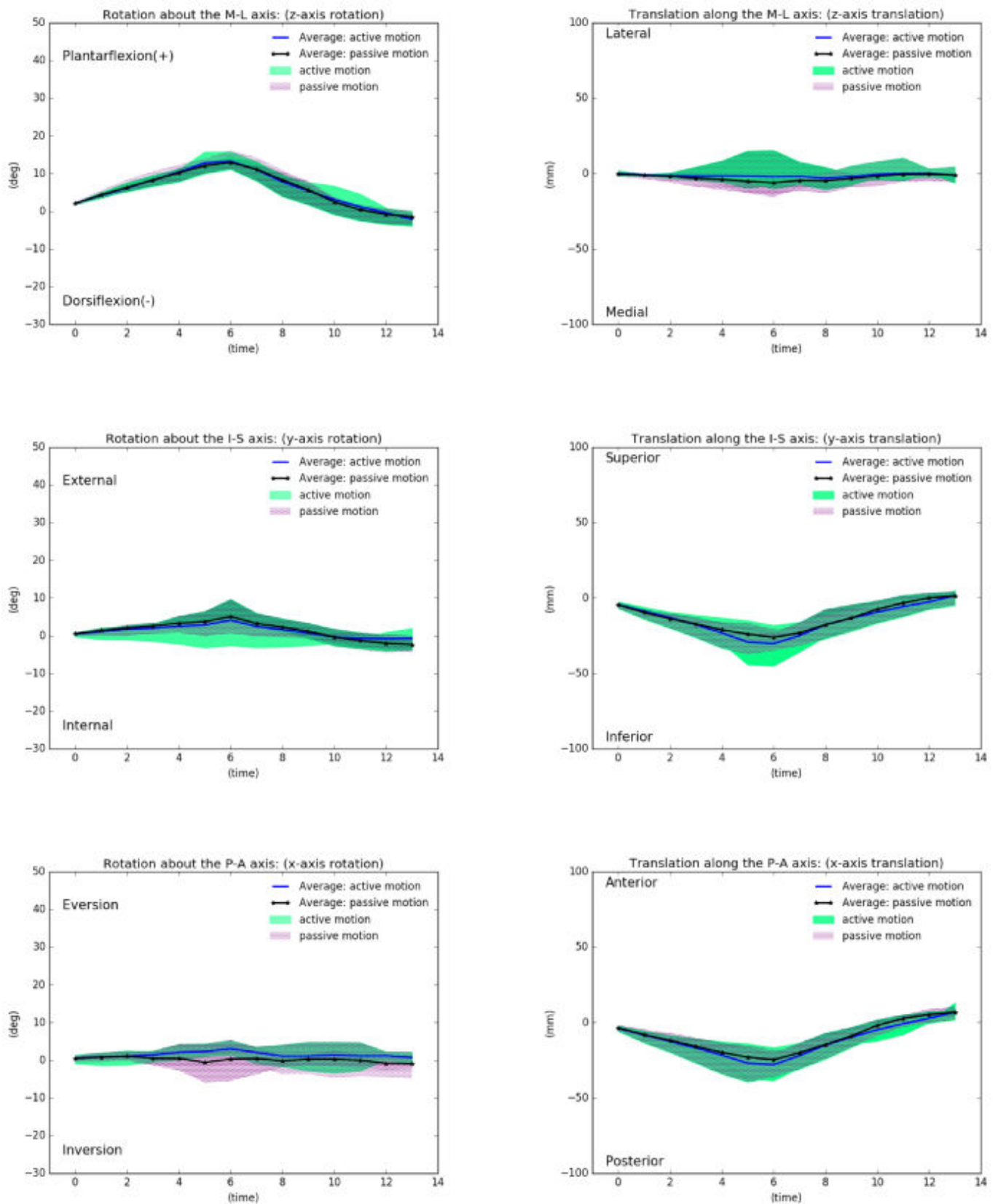


Figure 2.8: 3D normative kinematics of the subtalar joint using the proposed image processing method. The kinematics of the calcaneus are represented relative to the talar coordinate system in neutral position. Average rotation and translation were computed for both passive and active motion for the studied ankles. Standard deviation above and below the average line are shown (dotted shaded area for passive motion and green shaded area for active motion).

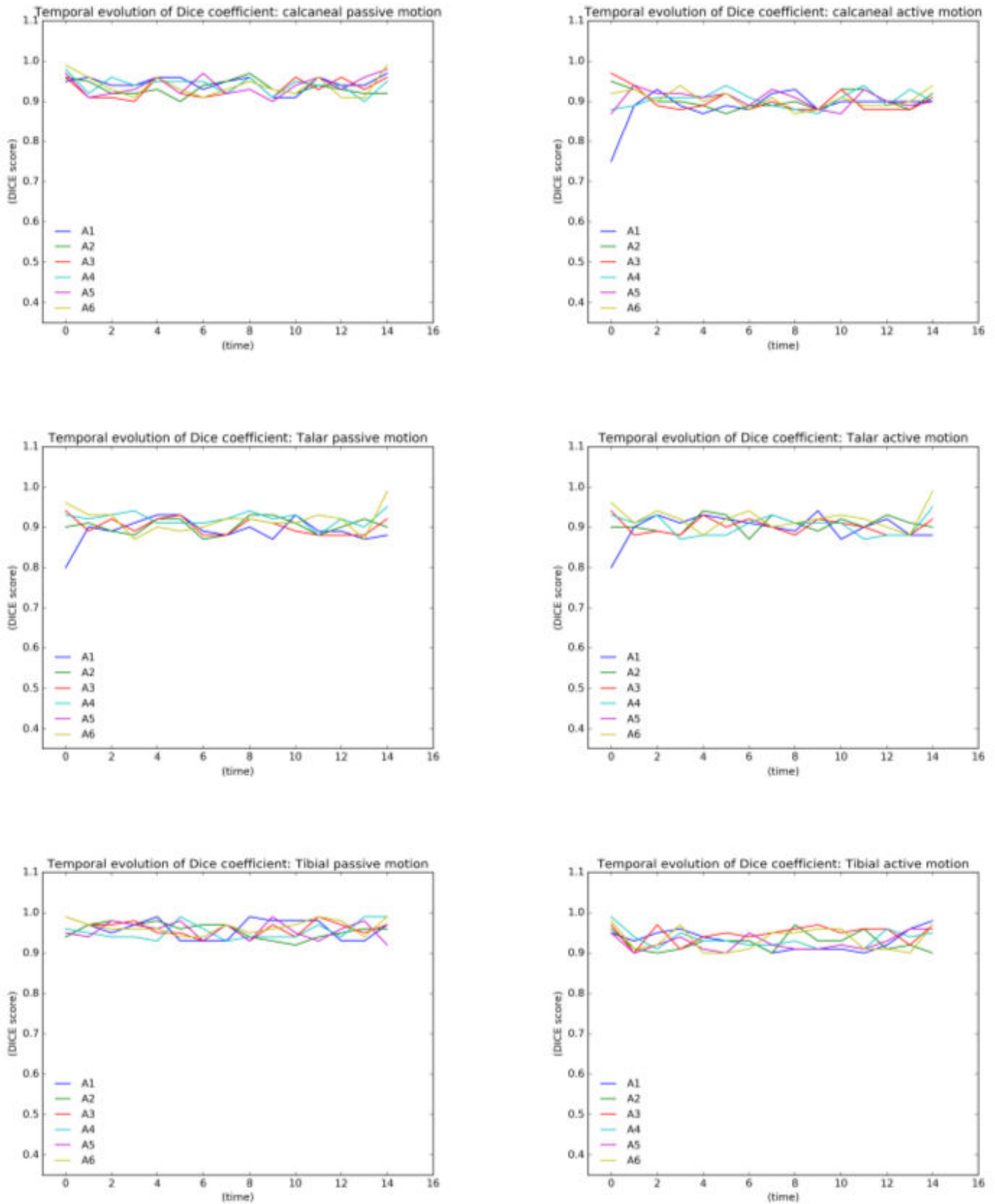


Figure 2.9: 3D DICE coefficients between manual and automatic bone segmentation maps for the six subjects of the pilot study taking account of the whole set of bone trajectories. Results for passive (left column) and active motion (right column) are separated. A dice value of 1 indicates perfect geometric alignment between automatic and ground truth segmentations.

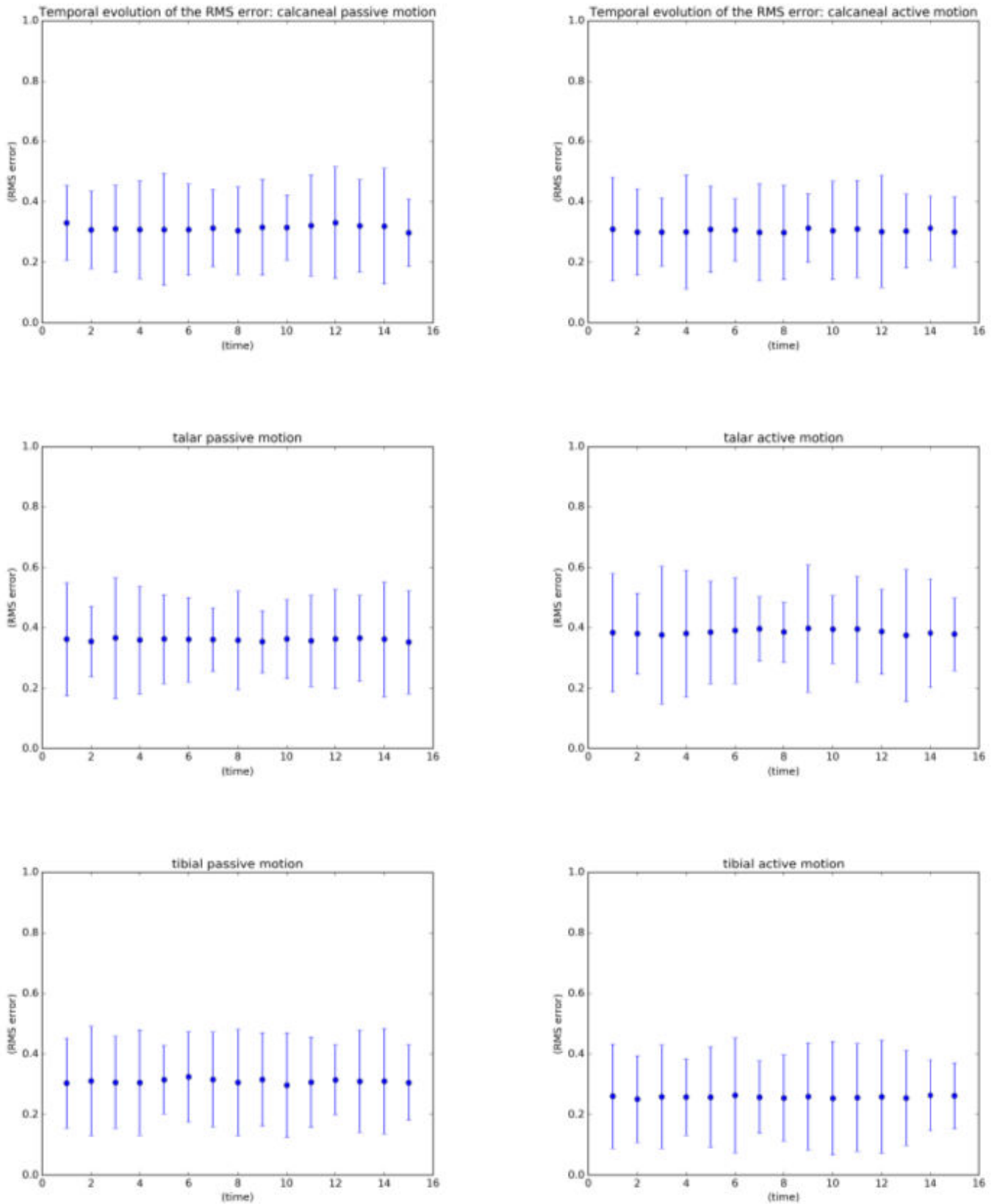


Figure 2.10: Temporal evolution of the root-mean-square error (RMSE in voxels) between manual and automatic bone segmentations for studied ankles. Errors are represented using error bars. The average is shown with a dotted line with one standard deviation above and below this line. Results for passive (left column) and active motion (right column) are separated.

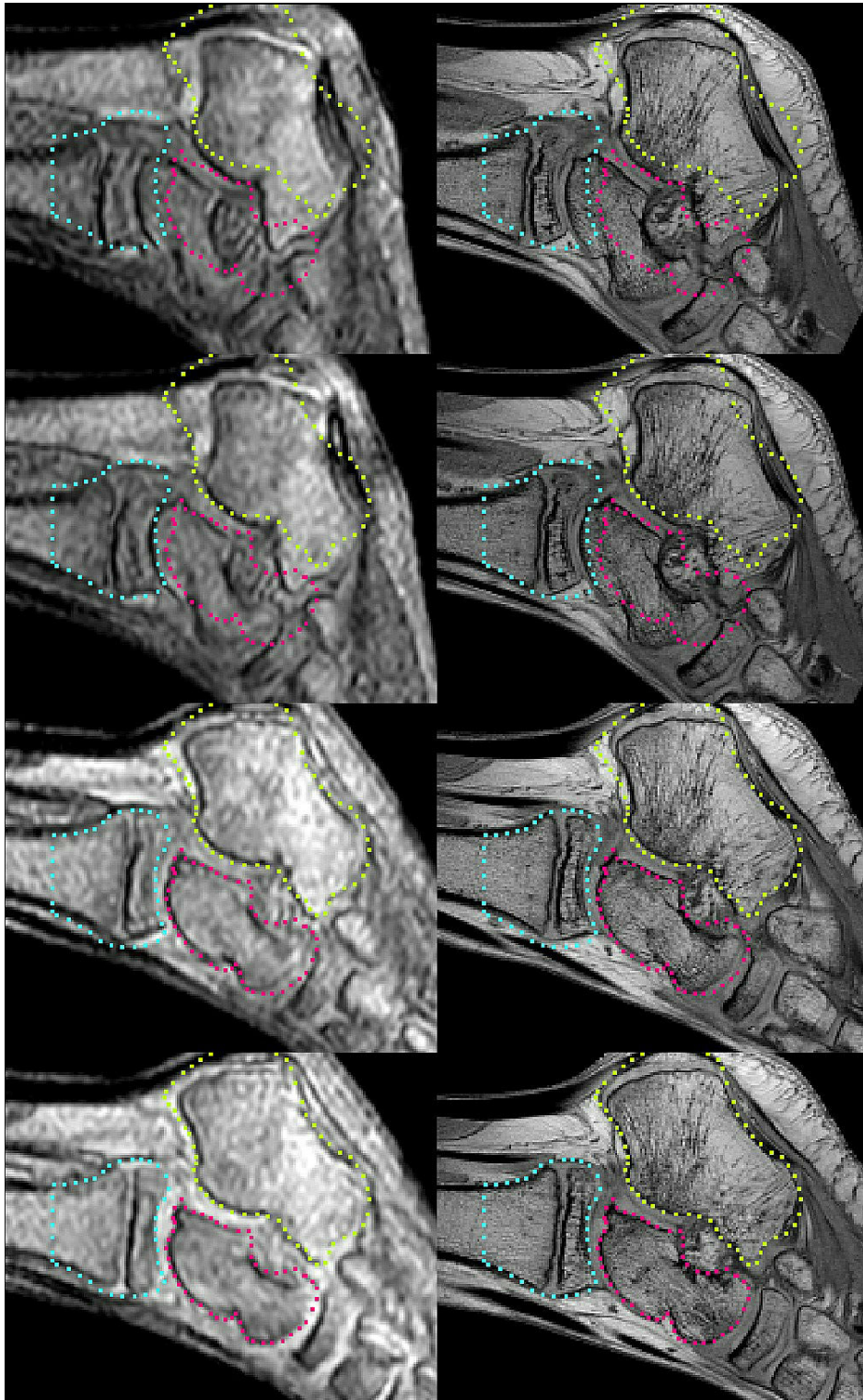


Figure 2.11: High-resolution temporal reconstruction of the ankle joint for one subject (subject 6: passive motion). First row: original dynamic images, second row: corresponding high-resolution reconstructed images, downsampled to resemble to the original low-resolution images in order to validate the reconstruction accuracy. Each column corresponds to one time frame. Contours of the first time frame show the reconstruction accuracy (column 1) and the joint motion (columns 2 to 4).

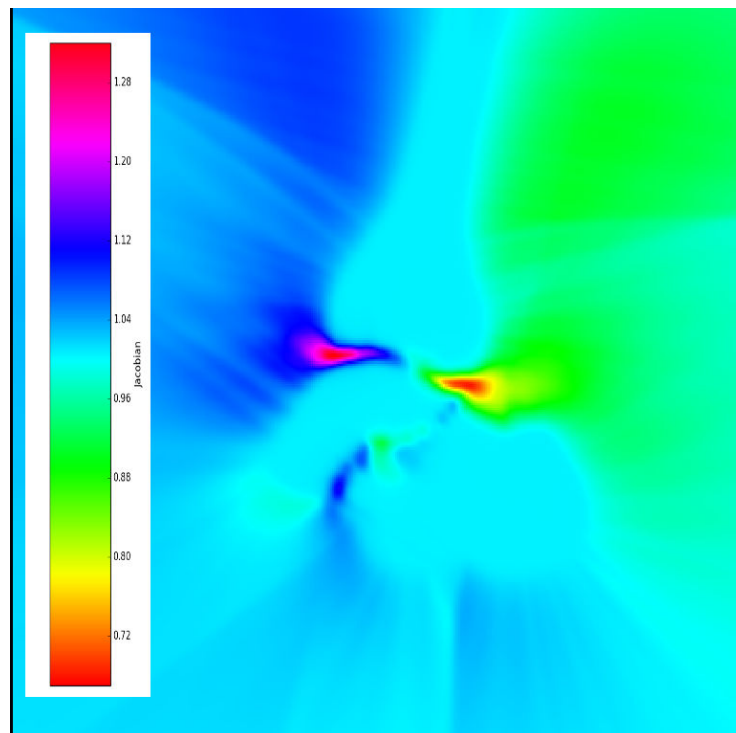


Figure 2.12: Jacobian map of the joint deformation field that maps  $D_1$  to  $D_2$  for subject 4. The Jacobian determinant  $J(x)$  at a voxel  $x$  measures how the voxel volume changes after the diffeomorphic registration. It indicates a volume increase if  $> 1$ , and a volume decrease if  $< 1$ . The Jacobian determinant is equal to 1 inside bone segmentations (indicating no voxel volume changes) as bones only perform linear rigid transformations (rotations and translations).



# Temporal resolution enhancement of dynamic MRI sequences within a motion-based framework

---

## Contents

---

<b>3.1</b>	<b>Introduction</b>	<b>55</b>
<b>3.2</b>	<b>State of the art</b>	<b>56</b>
<b>3.3</b>	<b>Motion artifacts in dynamic MRI sequences</b>	<b>57</b>
<b>3.4</b>	<b>Methods</b>	<b>58</b>
3.4.1	Skeleton-tracking algorithm	59
3.4.2	Smooth interpolation on $SE(3)$ : interpolation methods based on the exponential map	60
3.4.3	Spatio-temporal Log-euclidean polyrigid framework:	64
3.4.4	Redefinition of weighting functions	67
3.4.5	Jacobian of the estimated deformation fields	68
3.4.6	Combining the LEPF with the FSL registration tool	69
<b>3.5</b>	<b>Results</b>	<b>70</b>
<b>3.6</b>	<b>Discussion</b>	<b>73</b>
<b>3.7</b>	<b>Conclusion</b>	<b>76</b>

---

## 3.1 Introduction

Dynamic MRI has made it possible to non-invasively capture the moving human joints *in vivo*. Real-time Fast Field Echo (FFE) sequences have the potential to reduce the effect of motion artifacts by acquiring the image data within a few milliseconds [120]. However, the short acquisition times affect the temporal resolution of the acquired sequences (*i.e.* the scanning duration is short relative to the joint motion in order to optimally balance the trade-off between resolution, contrast and acquisition times). In fact, the existing real-time algorithms for spatio-temporal resolution enhancement of dynamic MRI sequences use three  $k$ -space sampling schemes [112, 43, 111]. However, this sampling scheme remains limited and suffers from low temporal

---

<sup>0</sup>This chapter is the subject of the publication [89].

resolution [81]. In this chapter, we propose a post-processing technique to reconstruct the missing frames of the sequence given the reduced amount of acquired data, which leads to recover the entire joint trajectory outside the MR scanner. To do this, we generalize the Log-Euclidean polyrigid registration framework to deal with dynamic three-dimensional articulated structures by adding the time as fourth dimension: we first estimate the rigid motion of each bone from the acquired data using linear intensity-based registration. Then, we fuse these local transformations to compute the non-linear joint deformations between successive images using a *spatio-temporal* log-euclidean polyrigid framework. The idea is to reconstruct the missing time frames by interpolating the realistic joint deformation fields in the domain of matrix logarithms assuming the motion to be consistent over a short period of time. The algorithm has been applied and validated using dynamic data from five children performing passive ankle dorsi-plantar flexion.

### 3.2 State of the art

Dynamic MRI techniques have been successfully employed to quantify *in vivo* musculoskeletal biomechanics such as the ankle kinematics during dorsi-plantar flexion. Sequences such as Cine-PC MRI or Fast-PC MRI [13] can provide velocity changes in the three directions of the space. However, these sequences require repeatable motions of the joint for up to two minutes (*e.g.* motion rate = 30 cycles/minute for one dorsi plantarflexion cycle) and the dynamic data are built using these repeatable motions. Hence, subjects with musculoskeletal disease who cannot complete a large number of repeated motions cannot be studied with cine-PC MRI techniques. Furthermore, motion tracking based on cine-PC data using a Fourier tracking algorithm [13] has limitations and the out of plane accuracy of the bone motion remained a challenge. Ultrafast Contrast-Enhanced MRI is another dynamic imaging technique which allows faster scanning speed by exploiting spatio-temporal redundancy and can acquire images during a single dorsi-plantar flexion cycle within 50 seconds [33]. However, these sequences require slow motion of the joint (mean rotation speed of  $1^\circ/s$ ) as they are sensitive to motion artifacts so the motion itself is reduced to almost static or quasi-static nature where no real functionality can be assessed. Real-time FFE sequences [120] are less sensitive to motion artifacts and they can reduce the scanning time to only 18 seconds to acquire a single cycle of dorsi-plantar flexion. However, the scanning duration is short relative to the joint motion cycle, thus making it difficult to acquire the entire or nearly the entire joint trajectory inside the MR scanner.

To resume, balancing the trade-off between acquisition speed and temporal resolution of dynamic sequences is still a challenging task.

Most existing real-time algorithms for accelerating the acquisition of dynamic MRI sequences have attempted to exploit the temporal correlations of the sequence [139] in order to reduce the effect of motion artifacts, leading to a challenging ill-posed inverse problem. However, it is hard to fastly acquire the entire or nearly the entire

joint trajectory inside the MR scanner because of the encountered hardware limitations (*e.g.* problems related to the surface coils) as well as the difficulty to satisfy the Nyquist sampling rate in the frequency space which introduces aliasing artifacts in the image space. This motivates researchers to tackle this inverse problem using deep learning methods by proposing a convolutional recurrent neural network architecture which exploits the temporal redundancy of sequences and the iterative nature of traditional reconstruction algorithms [114].

In this work, we propose to use FFE sequences, allowing the assessment of real functionalities (of muscles and tendon for example) with more comfortable and rapid acquisitions. The idea is to fastly acquire a reduced amount of data and then to estimate the missing amount with the help of image post-processing techniques. To this end, we propose to recover the missing data by continuously interpolating the temporal deformation field of the joint which can be estimated using diffeomorphic registrations from the acquired data assuming the motion to be continuous and consistent during scanning. In this context, we have extended the Log-euclidean polyrigid framework proposed by Arsigny et al. [7] to deal with spatio-temporal joint deformations with a small number of parameters (*i.e.* a small number of affine or rigid components) by adding the time dimension into the existing 3D stationary framework. In another work, Arsigny et al [6] presented a Log-Euclidean interpolation of tensors which are  $3 \times 3$  symmetric-positive-definite matrices. In this work, we propose to interpolate  $4 \times 4$  rigid transformation matrices (*i.e.* in the Lie group  $SE(3)$ ). In the literature [5, 35], the exponential mapping for solving the polyrigid Ordinary Differential Equation (ODE) is recursively computed using the scaling and squaring method involving approximation theory for which the accuracy always remains debatable. In the work of Moler et al. [100], the authors have synthesized a study to compare the different existing techniques for calculating the matrix exponential (like methods involving approximation theory, differential equations, or matrix eigenvalues) and they ended up with concluding that one can not decide which of the methods is the best ever and that this depends on the application. Hence, we propose to use matrix eigendecomposition for exactly computing the exponential mapping since computations are performed in non-dense regular grids due to the low-resolution of dynamic data, so that all the matrices can be stored in the main computer memory without the need of high-capacity RAM. The idea behind is to balance the trade-off between Furthermore, the scaling and squaring algorithm is prone to roundoff errors.

### 3.3 Motion artifacts in dynamic MRI sequences

The acquisition protocols and the data used in this work are exactly the same as the dynamic MRI sequences described in chapter 2.

As a feasibility study, two kind of acquisitions have been tested in order to select the best one for data post-processing: Sequences called "sInteractive" can enhance the image contrast but they are very sensitive to motion artifacts (Figure 3.1). On

the other hand, sequences called "Movie clear" are more prone to noise but are less sensitive to motion artifacts (Figure 3.2). Which motivates our use of Movie clear sequences during this thesis.

The global aim of this work is to provide high-temporal resolution dynamic MRI data while keeping the acquisition protocol described in chapter 2 intact. This allows the subjects with musculoskeletal disorders, who cannot repeat comfortably a high number of repeated motion cycles to be studied using the same protocol.



Figure 3.1: sInteractive sequences: these sequences are very sensitive to motion artifacts which may lead to misregistration when using intensity-based algorithms.

### 3.4 Methods

This chapter presents a method to provide a dynamic time sequence for MRI imaging of joints. The methodology is not specific to MRI necessarily, it involves interpolation of time frames in between measured or captured "static" frames using poly-rigid registration. Individual bones are treated rigidly and individually (Sections 3.4.1 and 3.4.2), and then a temporal deformation field is estimated by fusing these local rigid transformations (Section 3.4.3).

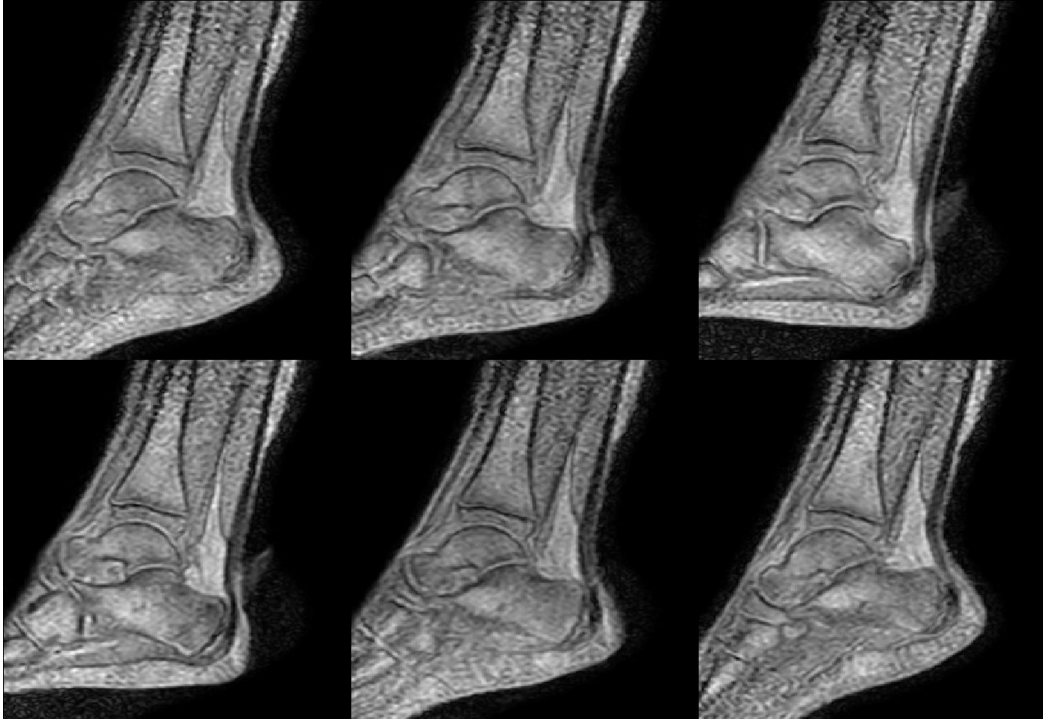


Figure 3.2: Movie clear sequences: these sequences are less sensitive to motion artifacts and thus are more suitable for intensity-based methods despite the presence of noise.

### 3.4.1 Skeleton-tracking algorithm

In this section, we present a robust skeleton-tracking algorithm employing intensity-based registration. For a given joint trajectory, each data-sequence was first splitted to  $K$  three-dimensional time frames (of  $352 \times 352 \times 6$  voxels, each one). Bones of interest (calcaneus, talus, and tibia) are manually segmented in the first or last time-frame and then automatically tracked throughout the sequence, forward or backward, using rigid registration. Our tracking method within the dynamic sequence is composed of two distinct steps:

- 1) Estimating bone rigid transforms by locally maximizing the correlation ratio between neighbouring time frames using voxel-wise weighting based on the segmentation masks (*i.e.* frame-to-frame registration).
- 2) Propagating the bone segmentations forward or backward by applying the estimated rigid transforms using nearest neighbor interpolation (*i.e.* reference-to-frame propagation).

The use of nearest neighbor interpolation allows for preservation of bone shapes contrary to other interpolation methods like trilinear which induces smoothing of the bone mask which affects sharp peaks particularly.

To go forward in time for example, only one image interpolation is needed to

propagate segmentations from the first time frame into each other time frame in the sequence. Since the composition of mappings in the Lie group  $SE(3)$  corresponds to the multiplication of elementary transformations, the direct path between images is computed by composing a set of estimated successive rigid transforms which gives a temporal manifold in the Lie Group  $SE(3) \times \dots \times SE(3)$  in order to avoid the propagation of interpolation errors as much as possible (*e.g.*  $T_{D_1 \rightarrow D_4}^i = T_{D_3 \rightarrow D_4}^i \times T_{D_2 \rightarrow D_3}^i \times T_{D_1 \rightarrow D_2}^i$ ). The same for backward propagation for which the last time frame becomes the starting point for the tracking process.

To improve the robustness of the algorithm, rotations are estimated based on their quaternion representations (*i.e.* using the unit quaternion representation of  $SE(3)$ ). Unit quaternions or versors are the most widely used in computer graphics and robotics, more precisely in tracking and motion interpolation algorithms regarding their compact representation of rotation angles in the space [101, 50]. Meaning rotations are represented by a rotation and an axis describing the orientation. Transformations are first splitted into two blocks: a rotation block and a translation vector. And these blocks are then mixed into a  $4 \times 4$  bloc that represents transformation matrix. In this work, we have used versors for representing bone rotations in order to tackle the problem of out-of-plane rotations that may occur during successive local registrations, even if the motion (*i.e.* ankle dorsi-plantar flexion) has been performed in sagittal plane because of the low-resolution of dynamic sequences.

Algorithm 2 describes the segmentation propagation for  $N$  bones of interest throughout the acquired  $K$  time frames (case of forward tracking).

---

**Algorithm 2** Bone motion estimation: forward tracking

---

**Input:** segmentation of each bone of interest  $i$  in the first time frame  $D_1$ .

**Motion estimation:**

- a: Estimate forward successive rigid transforms from  $D_k$  to  $D_{k+1}$ :  $\{T_{D_k \rightarrow D_{k+1}}^i\}_{k=1, \dots, K-1; i=1, \dots, N}$ .
  - b: Propagate bone segmentations from  $D_k$  to  $D_{k+1}$  using  $\{T_{D_k \rightarrow D_{k+1}}^i\}_{k=1, \dots, K-1; i=1, \dots, N}$ .
- 

Note that the bones of interest can be backward tracked by first segmenting  $D_K$  and then estimating successive rigid transforms from  $D_k$  to  $D_{k-1}$ :  $\{T_{D_k \rightarrow D_{k-1}}^i\}_{k=K, \dots, 2; i=1, \dots, N}$ . The results on bone motion tracking are presented for one subject in Figure 3.3.

**3.4.2 Smooth interpolation on  $SE(3)$ : interpolation methods based on the exponential map**

Smooth linear interpolation of rigid body displacements is a classical problem in robotics and computer graphics [146, 148, 147]. These methods have been employed for simulating human motion in computer graphics, more precisely for establishing

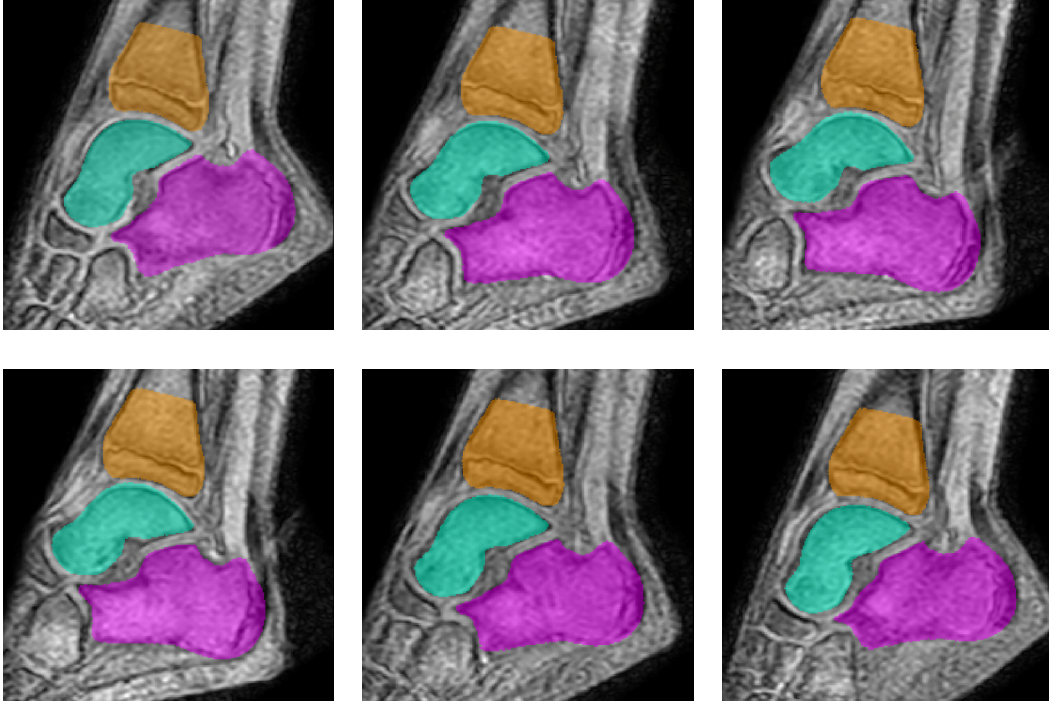


Figure 3.3: Joint forward-tracking. From up to down, from left to right:  $D_1$ ,  $D_4$ ,  $D_6$ ,  $D_9$ ,  $D_{12}$ , and  $D_{14}$ . Individual bone segmentation have been propagated separately.

a mathematical model to predict multi-joint arm movements [46]. In this section, we describe two principal interpolation methods which are based on the exponential map from the Lie Algebra  $se(3)$  to the associated Lie group  $SE(3)$ , involving a left invariant Riemannian metric on  $SE(3)$ . Then we propose to fastly compute this map via matrix eigendecomposition, allowing for computing the matrix exponential and for interpolating the rigid body motion in function of eigenvalues simultaneously.

### 3.4.2.1 Method 1:

In the work of Zefran *et al.* [147], the interpolation problem is formulated as follows:

*Given a sequence  $\{T_{\delta k}\}_{\delta k=1}^n$  of elements of the special Euclidean group  $SE(3)$ , where  $T_1$  encodes the initial position and orientation of a rigid body with respect to a fixed referential ( $F$ ), while  $T_n$  encodes its final position and orientation with respect to  $F$ : find a smooth curve  $\gamma(\delta k)$  such that  $\gamma(\delta k) = T_{\delta k}$  is the matrix which encodes the position and orientation of the rigid body at time  $\delta k$ .*

For a given homogeneous transformation matrix  $T \in SE(3)$  describing a rigid body displacement, we can rewrite  $T$  in a unique way as follows:

$$T = \exp(a_1 L_1 + a_2 L_2 + a_3 L_3 + a_4 L_4 + a_5 L_5 + a_6 L_6) \quad (3.1)$$

where  $L_i$  composes the basis of the associated Lie Algebra  $se(3)$ , this standard basis for  $se(3)$  is well defined in Equation (3.2). This exponential map is a diffeomorphism

for transformations *close to the identity*, while  $A = \{a_1, \dots, a_6\}$  defines the canonical coordinates for  $SE(3)$  so that the vector  $A$  represents a twist (for more details, we refer the reader to the work of *Zefran et al.* [146]). Finally, the interpolation is performed on a matrix representation of the vector  $A$  in the Euclidean space.

$$\begin{aligned}
 L_1 &= \begin{bmatrix} 0 & 0 & 0 & 0 \\ 0 & 0 & -1 & 0 \\ 0 & 1 & 0 & 0 \\ 0 & 0 & 0 & 0 \end{bmatrix}; L_2 = \begin{bmatrix} 0 & 0 & 1 & 0 \\ 0 & 0 & 0 & 0 \\ -1 & 0 & 0 & 0 \\ 0 & 0 & 0 & 0 \end{bmatrix}; L_3 = \begin{bmatrix} 0 & -1 & 0 & 0 \\ 1 & 0 & 0 & 0 \\ 0 & 0 & 0 & 0 \\ 0 & 0 & 0 & 0 \end{bmatrix} \\
 L_4 &= \begin{bmatrix} 0 & 0 & 0 & 1 \\ 0 & 0 & 0 & 0 \\ 0 & 0 & 0 & 0 \\ 0 & 0 & 0 & 0 \end{bmatrix}; L_5 = \begin{bmatrix} 0 & 0 & 0 & 0 \\ 0 & 0 & 0 & 1 \\ 0 & 0 & 0 & 0 \\ 0 & 0 & 0 & 0 \end{bmatrix}; L_6 = \begin{bmatrix} 0 & 0 & 0 & 0 \\ 0 & 0 & 0 & 0 \\ 0 & 0 & 0 & 1 \\ 0 & 0 & 0 & 0 \end{bmatrix}
 \end{aligned} \tag{3.2}$$

### 3.4.2.2 Method 2:

Recently [140], the authors presented a similar technique for interpolating on the Lie Group  $SE(3)$  in order to obtain a continuous trajectory from a discrete set of rigid-body poses. This technique also consists of mapping the elementary rigid transformations of a given rigid-body trajectory from the Lie Group  $SE(3)$  to the corresponding tangent plane  $se(3)$ . This allowed for performing temporal modeling in this Lie Algebra according to the following continuous curve:

$$\gamma_k(\delta k) = T_k \cdot \exp(\delta k \cdot \log(T_k^{-1} T_{k+1})) \quad \text{for } \delta k \in [0, 1] \tag{3.3}$$

where:  $T_1, T_2, \dots, T_K \in SE(3)$  are the elementary transformations composing the entire trajectory;  $k = 1, 2, \dots, K - 1$ ; and  $T_k$  is the rigid-body transformation between the two time instances  $k$  and  $k + 1$ . The main limitation of this method is that it imposes additional matrix multiplications, and thus it is not suitable for a voxel-wise computation scheme for which the primary challenges are the computational time and the memory requirements.

### 3.4.2.3 Method 3:

In the work of *Belta and Kumar* [14], the authors presented another technique for smooth interpolation of rigid body motion which is also based on the exponential map.

Let  $T \in SE(3)$  be the rigid transformation between two time instances  $k$  and  $k + 1$ , so that  $\log(T) = L$  is an element of the Lie algebra  $se(3)$ . Let  $\gamma_L : \mathbb{R} \mapsto SE(3)$  denotes the integral curve of the left invariant vector field  $L$ , with the initial condition  $\gamma_L(0) = id$ , then the trajectory of the rigid body can be described by the following ODE:

$$\dot{\gamma}_L(\delta k) = \gamma_L(\delta k) \cdot L \tag{3.4}$$

The solution of this ODE maps the interpolation from the Lie Algebra  $se(3)$  into the corresponding Lie Group  $SE(3)$ :

$$\exp(\delta k.L) = \gamma_L(\delta k) \quad \text{for } \delta k \in [0, 1] \quad (3.5)$$

The Equation (3.5) shows that the exponential map takes the line  $\delta k.L \in se(3)$ , into a one parameter subgroup of  $SE(3)$ .

Based on Equations (3.3) and (3.5), it is clear that the first method exhibits greater complexity than the second one as it imposes additional matrix multiplications.

This second method for generating smooth rigid body trajectories is simple to implement as the matrix exponential can be easily computed using eigendecomposition. Furthermore, it is possible to control the motion amount by controlling the rate of the eigenvalues of  $\delta k.L$ . Another advantage of this second method is that it can be easily extended from a simple log-euclidean *rigid* interpolation to a *more general* log-euclidean *polyrigid* interpolation by fusing multiple rigid transformations according to weight functions, and thereby allows for interpolating the non-linear joint deformations.

#### 3.4.2.4 Bone motion interpolation from 3D+t MRI data

In this work, we present an eigenvalue-based method for interpolation on  $SE(3)$ . And then the map from the Lie Group to the Lie Algebra (and vice versa) is performed thanks to the use of the Log Euclidean polyrigid framework for fusing multiple rigid transforms (section 3.4.3).

Let  $T_{i,k} \in SE(3)$  be the rigid transform from time frame  $D_k$  to time frame  $D_{k+1}$  for the bone  $i$ . Assuming that this matrix is diagonalizable (which is the case for most transformations in an orthonormal basis, such as the image coordinate system), then there exist an orthogonal matrix  $P$  and a diagonal matrix  $D$  such that  $T_{i,k} = PDP^{-1}$ . The non-zero elements of  $D$  are the eigenvalues of  $T_{i,k}$  ( $\lambda_1, \lambda_2, \lambda_3$ , and  $\lambda_4 = 1$ ), while the columns of  $P$  are the corresponding eigenvectors. Based on this matrix eigendecomposition, one can define the bone trajectory with respect to Equation (3.5) as follows:

$$T_{i,k}(\delta k) = \exp(\delta k.log(T_{i,k})) = P.diag(e^{\delta k.log(\lambda_1)}, e^{\delta k.log(\lambda_2)}, e^{\delta k.log(\lambda_3)}, 1).P^{-1} \quad (3.6)$$

In our context, the amount of local rotation of each bone is strictly below  $\pi$  radians, so that the matrix logarithm of  $T_{i,k}$  exists and always corresponds to the principal matrix logarithm. This suggests that the property  $\exp(\delta k.log(T)) = T^{\delta k}$ , is verified for all bone transformations (*i.e.*, during the motion cycle) and for  $\delta k \in [0, 1]$ .

Thanks to this property, one can reformulate the interpolation problem as follows:

$$\gamma_k^i(\delta k) = T_{i,k}(\delta k) = T_{i,k}^{\delta k} = PD^{\delta k}P^{-1} = P.diag(\lambda_1^{\delta k}, \lambda_2^{\delta k}, \lambda_3^{\delta k}, 1).P^{-1} \quad (3.7)$$

Changing  $\delta k$  continuously from 0 to 1 will *infinitesimally* change the matrix  $T_{i,k}^{\delta k}$  from the *identity* to the matrix  $T_{i,k}$ . This allows for interpolating between two bone poses from a realistic transformation matrix, expressed in homogeneous coordinates (*i.e.* in the special Euclidean group  $SE(3)$ ). This technique, if repeated for each bone transformation between each two successive time frames, have the potential to enhance the temporal resolution of the dynamic MRI sequence by a factor superior or equal to  $\frac{1}{\delta k}$  (by inserting  $(\frac{1}{\delta k} - 1)$  time frames in between  $D_k$  and  $D_{k+1}$  assuming  $\frac{1}{\delta k}$  to be an integer). For example, in the case where  $\delta k = 0.5$  (see Figure 3.9), the proposed pipeline will enhance the sequence temporal resolution by a factor of 2.

Figure 3.4 illustrates the application of this method to a synthetic data: in this experience, we have first synthesized an ellipsoid on a regular grid of  $128 \times 128 \times 128$  with a voxel spacing of  $0.28 \times 0.28 \times 0.5mm$  according to the following implicit equation:

$$E(x, y, z) = \begin{cases} 1, & \text{if } (x - 64)^2 + (y - 64)^2 + (z - 64)^2 \leq 5^2 \\ 0, & \text{otherwise.} \end{cases} \quad (3.8)$$

Note that Equation (3.8) corresponds to the equation of a sphere centered at  $(64, 64, 64)$  and with a radius  $R = 5$  in the case of isotropic resolution (*e.g.*, voxel size of  $k \times k \times kmm$ ).

Second, we have simulated a rigid transformation matrix  $T$  with the following parameters: rotations of  $(r_i, r_j, r_k) = (0, 0, 30^\circ)$ ; and translations of  $(t_i, t_j, t_k) = (0, 0, 0mm)$ , where  $R_I = (O, \vec{i}, \vec{j}, \vec{k})$  represents the image coordinate system.

Finally, a smooth trajectory of the ellipsoid is recovered by continuously interpolating the matrix  $T$  according to the equation (3.7). Idem for the interpolation of affine transformations, where the parameters of the simulated affine transformation, applied to the ellipsoid, are detailed in Figure 3.12.

### 3.4.3 Spatio-temporal Log-euclidean polyrigid framework:

The LEPF provides an efficient way to synthesize joint deformation fields with diffeomorphic properties like invertibility, differentiability, and smoothness, independently of the way local bone rigid transformations are first estimated. Since the LEPF relies on the computationally heavy solution of an ODE, the efficient computation of the exponential map over a regular grid requires the implementation of a fast algorithm to deal with the high-number of point trajectories to be estimated. In this context *Arsigny et al.* have proposed to use a fast algorithm to parameterize the polyrigid transformations based on the scaling and squaring method [5]. However, this method have a high memory requirement to store all matrices in the main computer memory during the repeated squarings. In fact, this technique is essentially based on the relation  $e^T = (e^{\frac{T}{2^s}})^{2^s}$ . The first step (scaling step) consists of evaluating  $e^{\frac{T}{2^s}}$  while the second step (squaring step) consists of squaring the approximant  $s$  times to finally obtain an estimation of  $e^T$ . For example, for a scaling

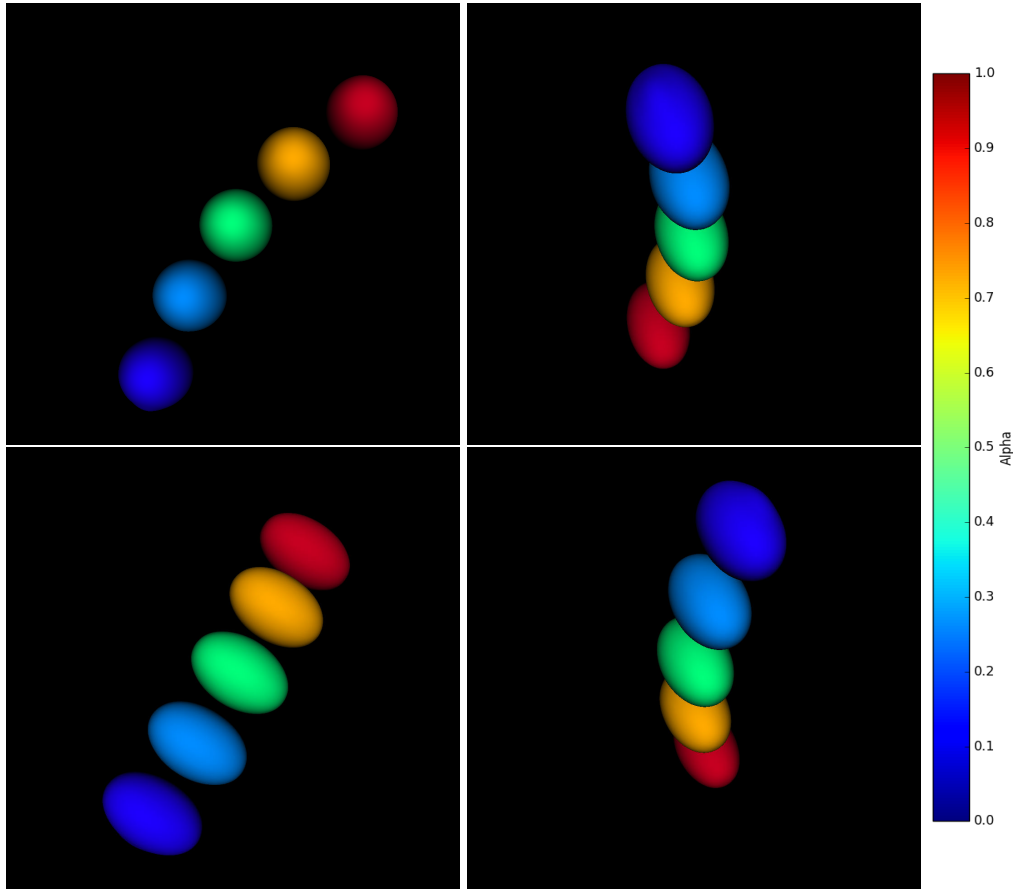


Figure 3.4: Interpolation of smooth motions on  $SE(3)$ : Consistent interpolation between two rigid-body poses (blue and red ellipsoids, respectively), transformation parameters are:  $t_i = 0mm$ ,  $t_j = 0mm$ , and  $t_k = 0mm$ ;  $r_i = 0^\circ$ ,  $r_j = 0^\circ$ , and  $r_k = 30^\circ$ . 3 secondary rigid transformations  $T^\alpha$  were interpolated between the identity and  $T$ , giving a smooth trajectory of the rigid body between two poses in function of  $\alpha$  ( $\alpha = \{n/4\}_{n \in \{1..3\}}$  in Eq 3.7).

factor of 5, 32 matrix multiplications are needed to compute the exponential map at each voxel:

$$T(., 1) = T(., \frac{1}{32})^{32} = \underbrace{T(., \frac{1}{32}) \circ \dots \circ T(., \frac{1}{32})}_{32 \text{ times.}}$$

and 16 matrix multiplications to compute the transformation half way between source and target positions:

$$T(., 0.5) = T(., \frac{1}{32})^{16} = \underbrace{T(., \frac{1}{32}) \circ \dots \circ T(., \frac{1}{32})}_{16 \text{ times.}}$$

Based on the fact that the bone transformations are *diagonalizable* as demonstrated

in Section 1.5.4, it is then possible to use the diagonalization method to parameterize the continuous bone trajectories by varying the time-scale factor from 0 to 1. Given a point  $x$  in the  $k^{th}$  time frame  $D_k$ , the target location of this point in the interpolated time frame  $D_{k+\delta k}$  (located between  $D_k$  and  $D_{k+1}$ ) can be computed thanks to the property  $\log(T^\alpha) = \alpha \cdot \log(T)$  with the following equation:

$$\Phi_{D_k \rightarrow D_{k+\delta k}}(x, \delta k) = \exp \left( \delta k \sum_{i=1}^N \tilde{w}_{D_k}^i(x) \log(\mathbb{T}_{i,k}) \right) \cdot x \quad (3.9)$$

where  $\Phi(x, 0) = x$ ;  $\delta k \in [0, 1]$  is the time-term added to the *stationary* polyrigid fusion formula;  $\mathbb{T}_{i,k}$  is an element of the Lie group  $SE(3)$ ;  $N$  is the total number of rigid components;  $\Phi_{D_k \rightarrow D_{k+\delta k}}$  is the *infinitesimal* deformation field from  $D_k$  to the time frame to be interpolated  $D_{k+\delta k}$  (the flow  $\Phi(\cdot, \delta k)$  of an autonomous ODE is a one-parameter subgroup of the group of diffeomorphisms);  $\tilde{w}_{D_k}^i$  is a normalized weight function (*i.e.*,  $\sum_{i=1}^N \tilde{w}_{D_k}^i(x) = 1, \forall x \in D_k$ ) which defines the local influence of the  $i^{th}$  bone displacement on the voxel  $x$  deformation (section 3.4.4).

In the literature, the exponential mapping of Eq (??) is approximated using the scaling and squaring method [61] which is prone to rounding errors [100]. In this work, this exponential mapping is computed exactly using eigendecomposition or spectral decomposition. Similarly to the matrix power defined in Eq(3.7), the matrix exponential is obtained by exponentiating a  $\delta k$  amount of the associated eigenvalues (*i.e.* non-zero elements of the diagonal matrix  $D$ , as per Eq (3.10)). Thus, we just needed to cast the exponentiation of the complex eigenvalues of the transformation matrices in regular grids (Figure 3.5) leading to smooth dynamic deformation fields that preserve the topology of the bones.

$$e^{\delta k \cdot L(x)} = P e^{\delta k \cdot D} P^{-1} = P \begin{pmatrix} e^{\delta k \cdot \lambda_1} & 0 & 0 & 0 \\ 0 & e^{\delta k \cdot \lambda_2} & 0 & 0 \\ 0 & 0 & e^{\delta k \cdot \lambda_3} & 0 \\ 0 & 0 & 0 & 1 \end{pmatrix} P^{-1}(x) \quad (3.10)$$

where  $L(x) = \sum_{i=1}^N \tilde{w}_{D_k}^i(x) \log(\mathbb{T}_{i,k})$ ;  $\{\lambda_k\}_{k \in \{1..4\}}$  are the eigenvalues of  $L(x)$  and the columns of  $P$  are the corresponding eigenvectors.

Since  $L(x)$  is a real transformation matrix in the domain of matrix logarithms, complex eigenvalues occur in complex-conjugate pairs: The real part of  $\lambda_i$  gives the contraction rate (if  $Re[\lambda_i(x)] < 0$ ) or the expansion rate (if  $Re[\lambda_i(x)] > 0$ ) of the voxel  $x$  in the  $i^{th}$ -direction; while the imaginary part of each eigenvalue is the frequency of voxel rotation. The Eigen decomposition is performed in *python* using the LAPACK (Linear Algebra PACKage) routines [4], and this takes approximately 3 seconds to compute the exponential map.

Finally, the floating image intensities are mapped to new coordinates in the target image space by spline interpolation.

Technically, This method can be considered as an application of the linear Koopman operator  $\mathcal{K}$  that capture the evolution of a nonlinear dynamical system (the joint).

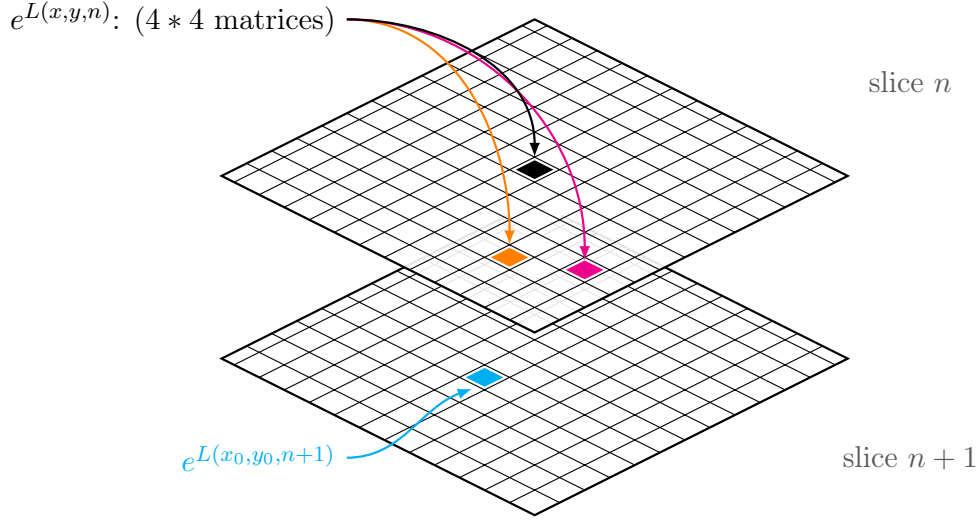


Figure 3.5: Repeated evaluation of matrix exponential over a three dimensional grid. This figure shows that the trajectories of all the points of the grid are computed simultaneously.

Where  $\mathcal{K} = \left( \delta k \sum_{i=1}^N \tilde{w}_{D_k}^i(x) \log(T_{i,k}) \right)$ ; the eigenvectors of  $\mathcal{K}$  are equivalent to the eigenfunctions of the Koopman operator; and the eigenvalues of  $\mathcal{K}$  give information about the spatial dynamics of the joint deformation field. [83].

#### 3.4.4 Redefinition of weighting functions

In the context of articulated structures registration, the choice of weight functions is very important as the main goal is to accurately estimate non-linear deformations of the joint without affecting bone shapes. It should be noticed that the Gaussian weight functions are more suitable for polyaffine fusion [122] than the polyrigid fusion, as they do not guarantee the rigidity and accuracy of the transformations in the bonny skeleton (by affecting sharp peaks particularly while smoothing). In [35, 34], *Commowick et al.* proposed an inverse-distance weighting function that preserves bone shapes after registration (Eq (3.11)). However, such a weighting function yields inaccurate deformation outside the segmented bones.

$$w_{D_k}^i(x) = \frac{1}{1 + \alpha \text{dist}(x, B_{D_k}^i)^\beta} \quad (3.11)$$

where  $B_{D_k}^i$  is the binary mask of bone  $i$  in time frame  $D_k$ ,  $\text{dist}(x, B_{D_k}^i)$  is the Euclidean distance between  $x$  and  $B_{D_k}^i$  (see Figure 3.6), and  $\alpha$  and  $\beta$  are two adjustable parameters. Figure 3.7 illustrates the normalized weighting functions for the three bones of interest of the ankle joint. As an example, these functions have been calculated using Eq (3.11) with  $\alpha = 0.5$  and  $\beta = 2$ . Each bone normalized weighting function is equal to 1 inside the bone mask  $B^i$  (*i.e.* for each point  $x$  satisfying  $\text{dist}(x, B^i) = 0$ ) and it decreases progressively (*i.e.* tends toward zero) as

the point moves away from the bone mask.

Experiments show that an increase in  $\beta$  leads to an increase in the deformation accuracy for non-rigid structures (see Figures 3.10 and 3.8). Thus, we propose new weighting functions suited for articulated registration. These new weight functions, which are inversely proportional to a rate of the distance exponential can be used within the log-euclidean framework in order to obtain more realistic deformations outside the segmented bones:

$$w_{D_k}^i(x) = \frac{2}{1 + \exp(\gamma \text{dist}(x, B_{D_k}^i))} \quad (3.12)$$

Note that these new weight functions yield more accurate transformations especially in the case of non-large deformations, which is always the case between two successive frames. With  $\gamma \in [0.4, 0.8]$ , to ensure a smooth interpolation.

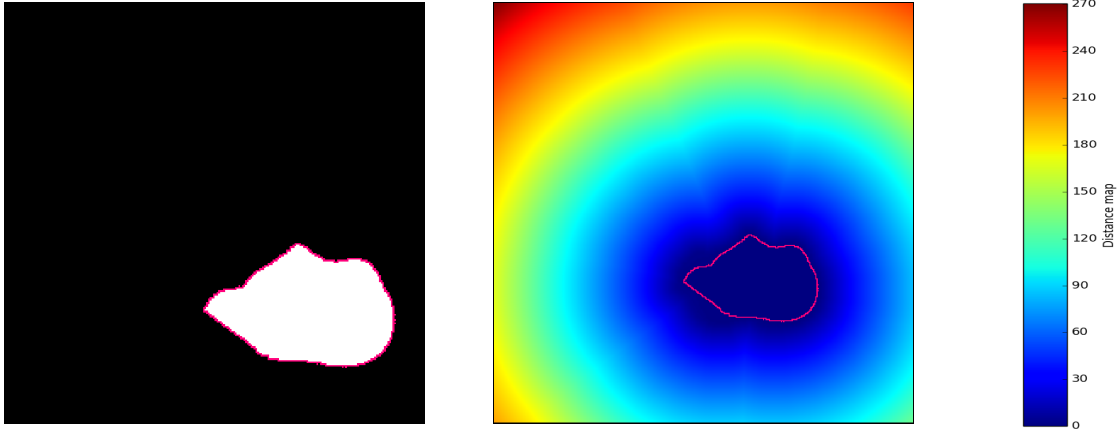


Figure 3.6: Euclidean distance map, from left to right: binary mask of the calcaneus; associated Euclidean distance map.

### 3.4.5 Jacobian of the estimated deformation fields

In order to analyze the joint deformations, we have computed the Jacobian maps associated to the estimated deformation fields. As shown in figure 3.11, the Jacobian value is equal to 1 for all bone voxels which confirms the conservation of bone shapes after image registrations. The Jacobian maps will be also used to detect volumetric changes of soft tissues and deformable structures such as the muscles and the Achilles tendon. The Jacobian is defined in three-dimensional space as follows:

$$\mathbf{J}_\Phi(\mathbf{x}) = \begin{vmatrix} \frac{\partial \phi_1(\mathbf{x})}{\partial x_1} & \frac{\partial \phi_1(\mathbf{x})}{\partial x_2} & \frac{\partial \phi_1(\mathbf{x})}{\partial x_3} \\ \frac{\partial \phi_2(\mathbf{x})}{\partial x_1} & \frac{\partial \phi_2(\mathbf{x})}{\partial x_2} & \frac{\partial \phi_2(\mathbf{x})}{\partial x_3} \\ \frac{\partial \phi_3(\mathbf{x})}{\partial x_1} & \frac{\partial \phi_3(\mathbf{x})}{\partial x_2} & \frac{\partial \phi_3(\mathbf{x})}{\partial x_3} \end{vmatrix} \quad (3.13)$$

The Jacobian maps of the estimated 3D deformation fields can be computed fastly on a regular grid using the rule of Sarrus for the computation of the determinant of  $3 \times 3$  matrices.

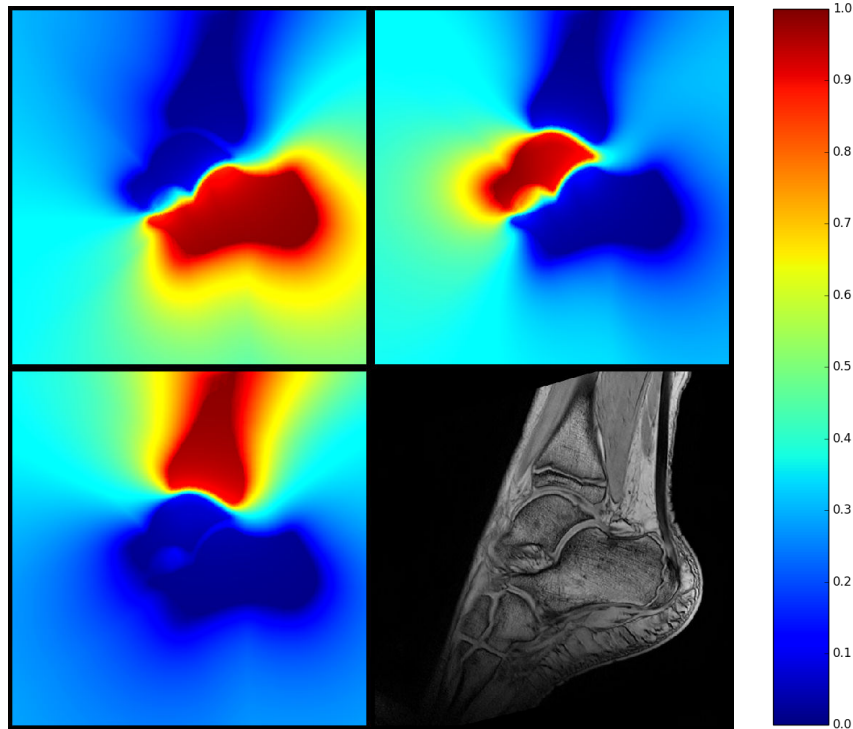


Figure 3.7: Normalized weighting functions: from up to down, from left to right: for the calcaneus; for the talus; for the tibia; and the associated high-resolution static image.

### 3.4.6 Combining the LEPF with the FSL registration tool

FSL flirt is a robust linear registration tool. However, it only provides a way to apply a unique geometric transformation to all image voxels. So since there is a need to treat voxels individually (*i.e.* each voxel has its own polyrigid transformation), one must understand how to apply a flirt transform to a single point.

Once the deformation field is computed using the LEPF by fusing a set of FSL-flirt transformations, the new coordinates in the target image space are computed based on the qform/sform matrix stored in the NIFTI file header simply because the flirt matrices do not use the NIFTI-defined  $mm$  coordinate system. In fact, FSL pre-dates NIFTI and so it uses (internally) a world coordinate system which is the voxel coordinates multiplied by the voxel spacing values according to each direction in the space  $(dx, dy, dz)$ . So everything is in  $mm$  where the  $(0mm, 0mm, 0mm)$  coordinate is the centre of the grid point  $(0, 0, 0)$ .

To determine the new coordinates of a voxel  $p = (x, y, z)$  in the target image, one needs to:

- take the initial voxel coordinates.
- flip  $p$  if necessary (based on the sign of the sform or qform determinant):  
if ( $\det(qform) > 0$ ):  
 $x' = N_x - 1 - x$ ;  $y' = N_y - 1 - y$ ; and  $z' = N_z - 1 - z$ ,  
where  $(N_x, N_y, N_z)$  represents the image size.
- scale the values by multiplying by the corresponding voxel spacing (in  $mm$ )
- apply the FLIRT matrix to map to the target image space
- divide by the corresponding voxel spacing (in  $mm$ , of the target image this time)
- flip  $p$  (based on the sign of the sform or qform determinant, of the target image this time)

Finally, this computation scheme is performed simultaneously over all grid points to determine the voxel coordinates of the estimated deformation field in the image space.

### 3.5 Results

The proposed pipeline has been applied on five dynamic MRI sequences. The exponential mapping of Eq (3.9) was computed within 3 s on an Intel<sup>®</sup> Xeon<sup>®</sup> Processor E3-1271 v3 3.60 GHz on a  $352 \times 352 \times 6$  regular grid using the proposed eigendecomposition method. Our code is implemented in *Python<sup>TM</sup>* using the LAPACK (Linear Algebra Package) routines for computing eigenvalues and eigenvectors. The RMSE (Root Mean Square Error) between Achilles tendon contours was around  $2mm$  when using the weighing functions defined in in Eq (3.11) with  $\beta < 3$ . This error is computed as follows:

- 1) Detection of ground truth contour voxels: first, the manually-segmented mask of tendon is eroded by one voxel in each dimension. Second, the ground-truth contours are obtained by subtracting the eroded mask from the original tendon mask.
- 2) Computation of the Euclidean distance map from contour of propagated Achilles tendon segmentation. This gives the distance between each image voxel and the tendon contours.
- 3) Finally, the RMS error is computed based on the distance map values at ground-truth contour voxels.  $RMSE(A_k, A_k^m) = \sqrt{1/n_c \cdot \sum_{x=1}^{n_c} dist^2(x, \zeta_{A_k})}$  where:  $A_k$  is the propagated mask of the tendon on dynamic image  $D_k$ ;  $A_k^m$  is a manually delineated mask of the tendon on the dynamic image  $D_k$ ;  $n_c$  is the total number of voxels of ground-truth contours (i.e. contours of  $A_k^m$ );  $\zeta_{A_k}$  is the contour of  $A_k$ ; and  $dist(x, \zeta_{A_k})$  is the Euclidean distance between  $x$  and  $\zeta_{A_k}$ .

The RMS error defined above has the potential to quantify the registration and interpolation errors mixed together. However, there is no evidence to separate between the two error origins. Which will be unfortunately the case for other error metrics such as the Hausdorff distance.

The redefinition of weighting functions played a crucial role in the enhancement of deformation accuracy outside the segmented bones while protecting skeleton edges, as shown in Figure 3.8 and as reported in Tab 3.1.

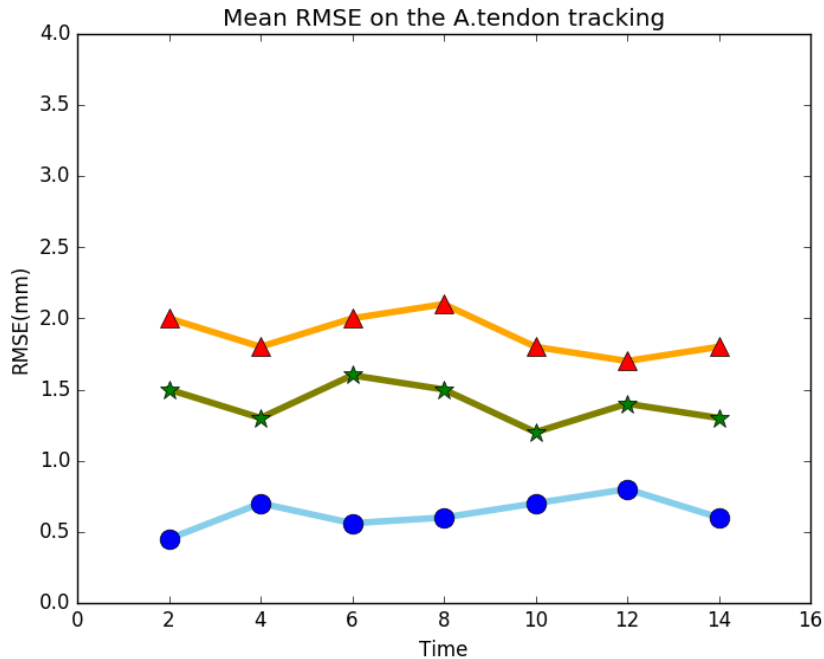


Figure 3.8: Temporal evolution of the mean RMSE across the five sequences for A.tendon tracking using different weight functions. Orange curve: when using the weight functions defined in Equation (3.11) with  $\alpha = 0.5$  and  $\beta = 1$ ; green curve: when using the weight functions defined in Equation (3.11) with  $\alpha = 0.5$  and  $\beta = 2$ ; blue curve: when using our weight functions defined in Equation (3.12) with  $\gamma = 0.4$ .

Figure 3.9 illustrates, for one subject, such high-temporal-resolution reconstructed data. Decreasing the value of  $\delta k$  increases the temporal resolution and makes the reconstruction more realistic outside the segmented bones as the interpolated transformations are close to the *identity* in this case. This leads to consistent interpolation of  $(\frac{1}{\delta k} - 1)$  time frames between  $D_k$  and  $D_{k+1}$  assuming  $\frac{1}{\delta k}$  to be an integer. Figure illustrates the Jacobian maps of the joint deformation fields between successive image.

The robustness of the method and the accuracy of the results have been evaluated using a local leave-one-out cross-validation technique. This was done by reconstructing each acquired time frame  $D_k$  based on the deformation field halfway

between  $D_{k-1}$  and  $D_{k+1}$  for  $k \in \{2 \dots K-1\}$ . Meaning each image  $D_k$  has been reconstructed from the image-intensities of  $D_{k-1}$ , where  $T_{i,k}$  is the rigid transformation from time frame  $D_{k-1}$  to time frame  $D_{k+1}$  for the bone  $i$  and  $\delta k$  is set to 0.5 in Eq (2.2) (in the case of forward tracking). This gives a set of reconstructed time frames  $\{D'_k\}_{k \in 2 \dots K-1}$ . Results on bone motion interpolation are reported in Tab 3.1. The accuracy of estimated deformation fields was then validated by computing the DICE overlap between the manually delineated masks of bones of interest on each acquired time frame  $D_k$  and the bone segmentations, automatically propagated onto each reconstructed time frame  $D'_k$ . For all sequences, the DICE coefficient was greater than 0.82 indicating accurate propagations of bone masks over each dynamic sequence. In order to provide a meaningful information about the accuracy of estimated deformation fields outside the segmented bones, we have computed the RMSE between contour-points of Achilles tendon on each acquired time frame  $D_k$  and on each reconstructed time frame  $D'_k$ . In all cases, the mean error was less than  $1mm$  (using the new weighting functions), indicating the accuracy of the estimated deformation fields for the non-rigid structures. Fig 3.10 illustrates the importance of the weighting functions when estimating and interpolating the temporal joint deformation field.

The proposed design for bone motion tracking is still robust in either direction (*i.e.* when going forward or backward in time) and the proposed method is robust to noise as well as to motion artefacts. Note that this interpolation technique is still available in the case of *polyaffine* transformations, inwhere local transformations to be fused are affine (*i.e.* include additional degrees of freedom like the scaling and shearing parameters). Figure 3.12 illustrates the consistent interpolation of a simulated affine transformation using matrix eigendecomposition.

Table 3.1: 3D DICE scores (for bones) and RMSE (for Achilles tendon contours) between manual segmentations of each structure of interest from the acquired data and segmentations of the same structures automatically-propagated onto the reconstructed data. Results are presented for several time frames across all subjects.

Time	$k = 2$	$k = 4$	$k = 6$	$k = 8$
Calcaneus	$0.88 \pm 0.3$	$0.83 \pm 0.4$	$0.84 \pm 0.3$	$0.84 \pm 0.2$
Talus	$0.84 \pm 0.2$	$0.84 \pm 0.4$	$0.83 \pm 0.2$	$0.85 \pm 0.4$
Tibia	$0.9 \pm 0.3$	$0.85 \pm 0.2$	$0.88 \pm 0.5$	$0.84 \pm 0.3$
A. tendon	$0.45 \pm 0.04mm$	$0.7 \pm 0.12mm$	$0.56 \pm 0.08mm$	$0.6 \pm 0.1mm$

Time	$k = 10$	$k = 12$	$k = 14$
Calcaneus	$0.88 \pm 0.5$	$0.85 \pm 0.3$	$0.82 \pm 0.1$
Talus	$0.83 \pm 0.3$	$0.84 \pm 0.3$	$0.82 \pm 0.2$
Tibia	$0.88 \pm 0.2$	$0.91 \pm 0.3$	$0.92 \pm 0.2$
A. tendon	$0.7 \pm 0.07mm$	$0.8 \pm 0.18mm$	$0.6 \pm 0.1mm$

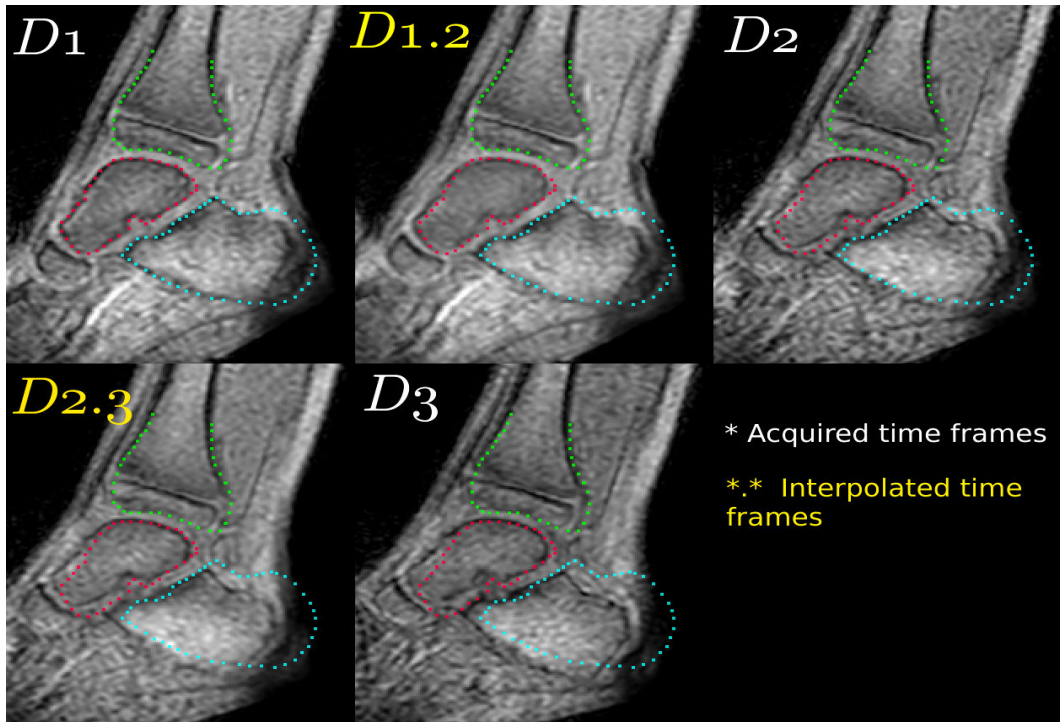


Figure 3.9: Interpolation of missing time frames using the proposed forward tracking method:  $D_k$  is the  $k^{th}$  acquired time frame; while  $D_{k.k+1}$  is the time frame half way between  $D_k$  and  $D_{k+1}$  (i.e.  $\delta k = 0.5$  in Eq (3.9)). for  $k = 1 \dots 3$ .

### 3.6 Discussion

FLIRT (FMRIB's Linear Image Registration Tool) [66] is a fully automated robust and accurate tool for linear (affine/rigid) intra- and inter-modal brain image registration. In this work, we have extended this tool to deal with non-linear image registration in the context of articulated structures. Although there exist different

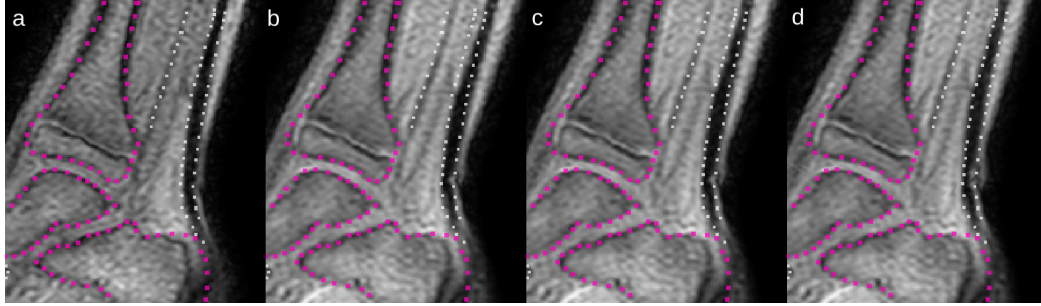


Figure 3.10: Effects of weighting functions on estimated deformation fields: (a) Target image; (b) Reconstructed image using the weighting functions defined in Equation (3.11) with  $\alpha = 0.5$  and  $\beta = 1$ ; (c) Reconstructed image using the weighting functions defined in Equation (3.11) with  $\alpha = 0.5$  and  $\beta = 2$ ; (d) Reconstructed image using our weighting functions defined in Equation (3.12) with  $\gamma = 0.4$ . The contours of bones (magenta) and of Achilles tendon (white) have been drawn in the target image to show the reconstruction accuracies when changing the weighting functions. Despite the fact that all the used weighting functions conserve bone topologies (this was validated by checking that the Jacobian of the deformation field is equal to 1 over bone segmentations), the reconstructed image is more accurate for non-rigid structures such as the Achilles tendon when using our proposed weighting functions (d).

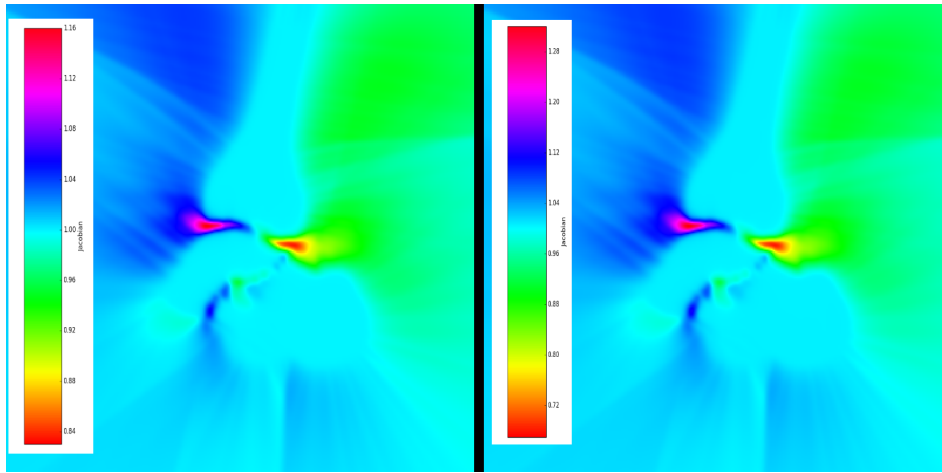


Figure 3.11: Jacobian maps of the joint deformation fields. From left to right: the deformation field that maps  $D_1$  to  $D_{1,2}$ ; and the deformation field that maps  $D_1$  to  $D_2$  where:  $D_1$  is the 1<sup>st</sup> acquired time frame while  $D_{1,2}$  is the time frame half way between  $D_1$  and  $D_2$ . these maps estimate the local volume percentage difference of the targets with respect to the source time frame. A positive Jacobian determinant values reflect that there is no folding in the deformation field.

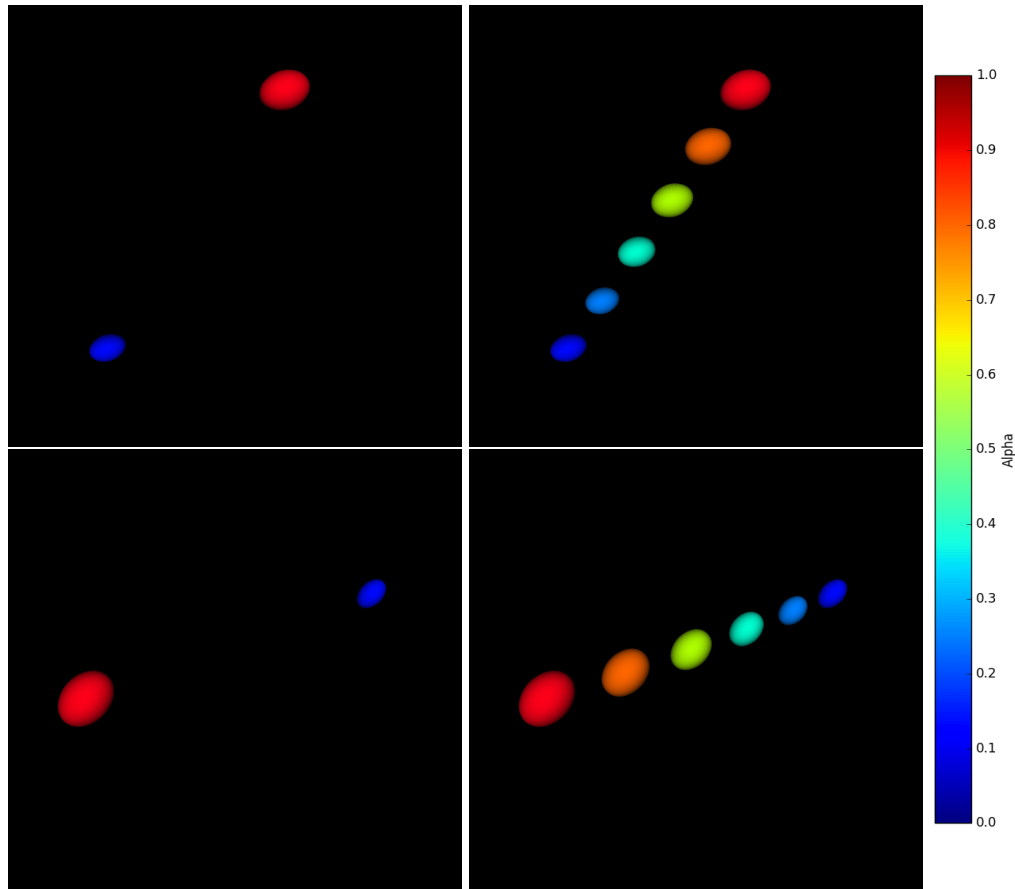


Figure 3.12: Consistent interpolation of a simulated affine map (*i.e.*, the transformation that maps the blue ellipsoid to the red one), transformation parameters are: Translations:  $t_i = 0mm$ ,  $t_j = 0mm$ , and  $t_k = 0mm$ ; Rotations:  $r_i = 0^\circ$ ,  $r_j = 0^\circ$ , and  $r_k = 10^\circ$ ; Shearings:  $g_i = 0$ ,  $g_j = 0$ , and  $g_k = 0$ ; Scalings:  $s_i = 1.5$ ,  $s_j = 1.5$ , and  $s_k = 1.5$ . 4 secondary transformations  $T^\alpha$  were interpolated between the identity and  $T$ , giving a smooth affine trajectory of the ellipsoid between two instants in function of  $\alpha$  ( $\alpha = \{n/5\}_{n \in \{1..4\}}$  in Eq 3.7).

tools for non-linear or diffeomorphic image registration such as FNIRT or ANTs (Advanced Normalization Tools) [8], they did not necessarily preserve bone shapes after the alignment process [1]. So we have preferred to fuse the flirt transformations by the log euclidean polyrigid framework. If  $n$  is the number of intermediate points chosen to discretize the continuous trajectory of each point  $x$ , the scaling and squaring method is the most commonly used technique for computing the matrix exponential in previous works [5]. However, this method only provides an approximation of the matrix exponential (with a certain level of accuracy). So since it is important to compute the matrix exponential efficiently and accurately, we have proposed to compute the matrix exponential using matrix eigendecomposition in the complex domain (by computing the eigenvalues and right eigenvectors of  $4 \times 4$

transformation matrices), provided that the trajectories of all the points of the regular grid are computed simultaneously as the grid is interpreted as a stack of  $dim_0 \times dim_1 \times dim_3$  matrices, each of size  $4 \times 4$ . In fact, for all real transformation matrices expressed in homogeneous coordinates, the associated complex eigenvalues occur in complex-conjugate pairs: The real part of  $\lambda_j(x)$  gives the rate of expansion (if  $Re[\lambda_j(x)] > 0$ ) or contraction (if  $Re[\lambda_j(x)] < 0$ ) of the voxel  $x$ ; the imaginary part of the eigenvalue is the frequency of voxel rotation about each direction in the 3D space.

Remarkably, the novel fusion in the domain of matrix logarithm is very close to the direct fusion in regions without singularities, independently of the way local rigid deformations are first estimated.

Finally, by the same qualitative discussion one could argue that such a design could walk in either direction (forward or backward in time), just as a human can walk forwards and backwards.

### 3.7 Conclusion

The global aim of this work is to provide high-temporal resolution dynamic MRI data while keeping the acquisition protocol described above intact. This allows the subjects with musculoskeletal disorders, who cannot comfortably repeat a high number of motion cycles to be studied using the same protocol. In this chapter, we have presented a motion-interpolation-based method on the Lie group  $SE(3)$  for increasing the temporal resolution of acquired dynamic MRI sequences. The intuition behind is that the joint motion is cyclic and pseudo-consistent in nature. We have generalized the Log-Euclidean polyrigid registration framework to dynamic articulated structures and we have also proposed new weight functions which are well adapted to our context. The exponential map from polyrigid body velocities (*i.e.* elements of the Lie algebra  $se(3)$ ) to the Lie Group of rigid body displacements  $SE(3)$  is computed in an efficient and elegant way using matrix diagonalization-based techniques so that the infinitesimal joint deformations are obtained by exponentiating the infinitesimal eigenvalues averaged in the logarithmic domain. The matrix eigen-decomposition lends itself well to modeling temporal dynamics of rigid bodies. To conclude, the proposed post processing technique aims to overcome the physical limitations (both hardware and physiological constraints) related to real-time dynamic MR imaging algorithms which are generally based on compressed sensing theory [49], for which it is hard to fastly acquire the entire or nearly the entire joint trajectory inside the MR scanner because of the limited  $k$ -space sampling [69] (*i.e.* the difficulty to satisfy the Nyquist sampling rate in the frequency domain).

A b-spline motion interpolation is possible [15] and this will be targeted in future works.

# 4D *in vivo* non-invasive quantification of ankle joint space width using dynamic MRI

---

## Contents

---

<b>4.1</b>	<b>Introduction</b>	<b>77</b>
<b>4.2</b>	<b>State of the art</b>	<b>78</b>
4.2.1	From stationary to non-stationary data	78
4.2.2	Related works	79
4.2.3	Computation of soft tissue thickness	80
4.2.4	Proposed pipeline	81
<b>4.3</b>	<b>A computational method: Eulerian framework for measuring soft tissue thickness</b>	<b>81</b>
4.3.1	Fast Eulerian PDE approach	82
4.3.2	Experiments	86
<b>4.4</b>	<b>Spatio-temporal evolution of the JSW</b>	<b>88</b>
4.4.1	Temporal tracking of joint space area	89
4.4.2	Computation of temporal joint space width	91
<b>4.5</b>	<b>Validation</b>	<b>92</b>
<b>4.6</b>	<b>Results</b>	<b>93</b>
<b>4.7</b>	<b>Conclusion</b>	<b>95</b>

---

## 4.1 Introduction

Spatio-temporal evolution of joint space width (JSW) during motion is of great importance to help with making early treatment plans for degenerative joint diseases like osteoarthritis (OA), by identifying the critical phases of movement. These diseases can affect people of all ages leading to an acceleration of joint degeneration and to limitations in the activities of daily living. 4D *in vivo* quantification of JSW can also be used to investigate the impact of musculoskeletal deformities on the

---

<sup>0</sup>This chapter is the subject of the publication [87].

dynamic cartilage contact mechanics, such as the the equinus deformity of the foot and its direct impact on the dynamic tibiotalar contact area. However, only a few *in vivo* studies have attempted to quantify the JSW from moving joints due to the lack of *in vivo*, dynamic cartilage contact mechanics data [19]. In this chapter, we present a generic pipeline to accurately determine the changes of the JSW during the joint motion cycle where the bone kinematics are derived using the motion estimation algorithm presented in chapter 2. The main goal is to identify the spatial location of each bone and of the joint space section at each time frame, but in the HR domain of the static scan (*i.e.* image resolution of  $0.26 \times 0.26 \times 0.8mm$ ). So that the temporal JSW measures are performed in this HR domain using an Eulerian approach for solving partial differential equations (PDE) inside a deforming inter-bone area where the HR reconstructed bone segmentations are considered as temporal Dirichlet boundaries.. The proposed approach has been applied and evaluated on *in vivo* MRI data of five healthy children to non-invasively quantify the spatio-temporal evolution of the JSW of the ankle (tibiotalar joint) during the entire dorsi-plantar flexion motion cycle. Promising results were obtained, showing that this pipeline can be useful to perform large-scale studies containing children with spastic equinus deformity for the ankle joint.

## 4.2 State of the art

Providing accurate spatial-temporal information on the JSW can help researchers and clinicians in identifying the critical phases of movement and making early treatment plans for degenerative joint diseases like OA [40]. The normal tibiotalar JSW in the neutral position varies in thickness from 1 to 4mm [65], reflecting the morphology of contact cartilage sublayers. In this work, we present a methodology to quantify the JSW during the entire joint trajectory.

### 4.2.1 From stationary to non-stationary data

In the literature, most studies were based on stationary acquisitions from different joints to evaluate intra-subject (*i.e.* over a large period of time to assimilate the progression of joint damage) [64] or inter-subject variability of the JSW [26]. In [53], Goker *et al.* quantified the tibiotalar JSW using 2D radiographic examinations. However, 2D measures are typically less informative than 3D measures simply because the human joints are complex 3D structures. In [26], the authors proposed to quantify 3D JSW of the metacarpophalangeal joint using high-resolution peripheral quantitative CT, by segmenting the joint section using binary morphological operations (*i.e.* dilation and erosion of bone segmentations). However, the behaviour of those morphological operations is hard to predict, and thus the resulting segmentations are not necessarily anatomically accurate. In [65], the authors evaluated the JSW of the tibiotalar joint using 3D reconstruction of CT images. However, their study reports only results at three specific locations (neutral position, maximum dorsiflexion, and maximum plantar flexion of the ankle joint). Furthermore, CT

scans expose subjects to harmful radiation in addition to the static nature of acquired data, making it hard to assess real functionalities and to perform large-scale *in vivo* studies.

Dynamic MRI is a non-invasive imaging technique which can be useful for performing large scale *in vivo* studies. However, this technique comes with its own set of challenges such as low-resolution, anisotropy, and motion artifacts.

#### 4.2.2 Related works

Recently, *Borotikar et al.* [20] proposed a methodology to non-invasively quantify patellofemoral cartilage contact kinematics from *non-stationary* MRI acquisitions based on the overlap between the two contact cartilage layers under the assumption that each cartilage layer should undergo the same rigid transform as that of the attached subchondral bone. However, the bone motions are estimated by integrating velocity data in the Fourier domain (*i.e.* by integrating the trajectory of some landmarks defined on each bone). A major limitation is the out of plane accuracy of the bone motion because the accuracy of cine-PC MRI is independent of the shape of the bone being tracked [13]. To tackle this problem, *Borotikar et al.* [19] proposed another method to quantify patellofemoral cartilage contact kinematics using all the volumetric information provided by anatomical dynamic MRI data to estimate bone motions using mesh-based registration:

Cartilage contact mechanics are quantified by creating rigid models of knee bones, defining the transformations from static to dynamic pose, and then applying ankle kinematics to these models. Briefly, static and sparse dynamic 3D patellar and femoral bone models are created and the optimal transformation of the static model to its dynamic pose is determined (Geomagic Inc., Research Triangle Park, NC). It is assumed that cartilage is rigidly attached to the subchondral bone and thus this 3D transformation is directly applied to its cartilage surface as well.

Patellar and femoral cartilage surfaces are reconstructed from static images using a thin-plate spline (TPS) mathematical surface [19, 22] and subsequently transformed to dynamic neutral position. A kinematics driven contact mechanics algorithm is employed using TPS surfaces and Talocrural and subtalar joint kinematics. At each time frame, contact between the two surfaces are determined by evaluating the amount of overlap between the stationary and moving cartilage surfaces. Contact area is determined by summing the area of each overlap using either Bretschneider's formula or Heron's formula [16]. Contact area centroid is determined as the weighted average of each contact grid patch's location with weighting based on the patch area [19]. Peak strain location are defined as the single point on the contact grid that corresponds with the maximum overlap value [19].

However, in addition to the manual segmentation of the static scan, it was needed to manually segment the dynamic data as they have used mesh-based registration for reconstructing HR temporal bone models by finding the rigid transformation of each bone geometry from static to each dynamic image. Moreover, this manual intervention is time consuming and prone to segmentation bias because of image noise

and low-resolution of dynamic data. These techniques have been used later in the work of *Vignos et al.* [141] to quantify tibio-femoral cartilage contact kinematics.

### 4.2.3 Computation of soft tissue thickness

To quantify the cartilage thickness distribution in the tibiofemoral joint [79], the authors have proposed to compute the thickness map of each cartilage layer separately. Their technique for finding cartilage thickness consists of: for each sampling point on the articular surface, a sphere was centered at this point and expanded until it was tangent to the opposite surface (*i.e.*, subcondral bone surface). The radius of this sphere, representing the shortest distance between the two surfaces, gives then the cartilage thickness. This method has been reproduced in [142] to quantify cartilage contact deformation of ankle joint. One limitation of this approach is that the thickness measures could be underestimated in the case of steep curvatures and complex surface structures (as in the case of the human brain cortex because of its complex topology). Figure 4.1 illustrates a thickness misestimation when using this method.

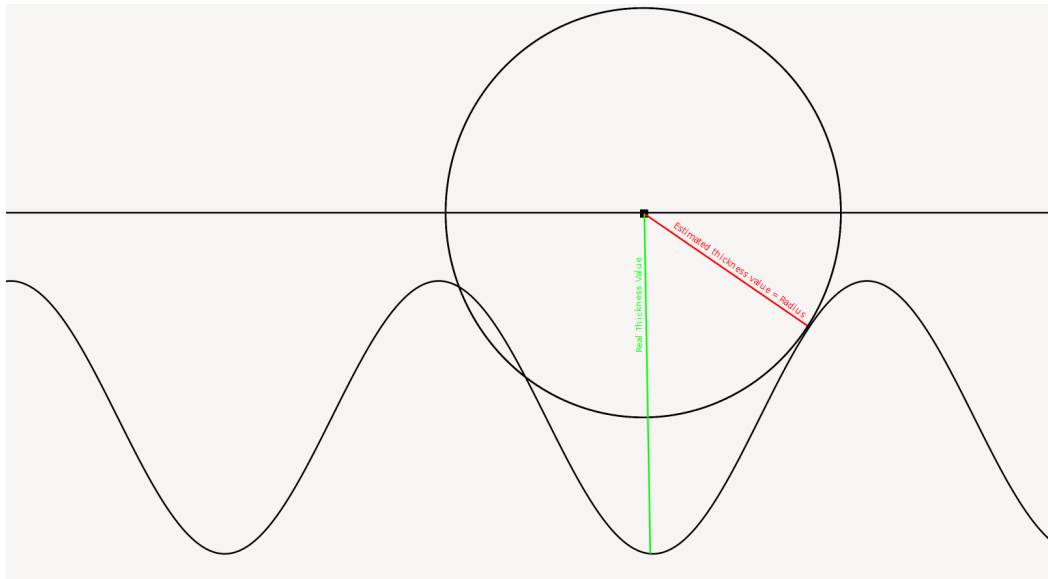


Figure 4.1: **Problems related to thickness estimation: the actual thickness (green); and the calculated thickness using the method proposed in [142] (red).**

In the context of soft-tissue thickness visualization and quantification, other techniques for computing anatomical thickness have been proposed, such as: the coupled-surface methods [85] which define the thickness between two boundaries as the distance between point pairs uniquely associated between the two boundaries; or the uncoupled-surface methods [94] which define the thickness as the nearest distance (from each point on a given boundary to the closest point on the opposing boundary). The limitations of these methods in terms of accuracy are then highlighted in the work of *Yezzi et al.* [145].

To overcome these limitations, *Yezzi et al.* [145] presented an efficient and computationally fast and stable voxel-based approach that can deal with highly convoluted objects, inspired by the work of *Jones et al.* [70]. This method can be applicable to any arbitrary topology as it does not require explicit construction of any correspondence trajectories. This consists on an Eulerian framework for computing the thickness of tissues based on the solution of the Laplace equation between two simply connected boundaries. The employment of Laplace’s equation provides a one-to-one correspondence between the two boundaries. Furthermore, the correspondence trajectories may never intersect as they are always perpendicular to the equipotential layers they derived from. Consequently, they terminate perpendicularly to each of the two boundary surfaces. The Laplace equation has been also employed to model contact cartilage layers [47], and to model cortical layers from high-resolution functional MRI [151]. The Eulerian PDE approach has been successfully employed to measure the cortical thickness by taking into account the partial volume effect [41, 2], to segment the articular cartilages from conventional MRI of the knee joint [47], and to compute the myocardial wall thickness from computed tomography images [28]. To summarize, this voxel-based approach is suitable for large data sets (*e.g.* the high-resolution reconstructed dynamic MRI sequences) of population studies.

#### 4.2.4 Proposed pipeline

In this chapter, we extend the Eulerian approach to the measurement of the JSW during the entire joint motion cycle using dynamic MRI sequences, which will certainly provide new temporal motion features. In our previous work [88], we have proposed a motion-based algorithm for estimating HR dynamic MRI sequences via a log-euclidean polyrigid framework (LEPF) [5] using both static and dynamic MRI. In the current work, we use the associated motion estimation algorithm to track the tibiotalar joint with high accuracy and without the need for manual segmentation of dynamic data. To summarize, we present a complete pipeline for: 1) estimating spatio-temporal bone rigid transformations, 2) computing spatio-temporal non-rigid deformations of the joint space area using the LEPF (Section 4.4.1), 3) measuring dynamic, *in vivo* JSW via an iterative relaxation method using the high-resolution-reconstructed bone segmentations as Dirichlet boundaries (Section ??).

### 4.3 A computational method: Eulerian framework for measuring soft tissue thickness

After determination of the skeleton kinematics during a single dorsi-plantar flexion motion cycle, we evaluated the contact mechanics of the ankle joint during motion based on the estimated bone rigid transformations from static to dynamic sparse data. To do this, we evaluated the spatio-temporal joint space width (JSW) of the tibio-talar joint, which is the primary joint responsible for plantarflexion and dorsi-

flexion of the ankle. The developed mathematical tools for evaluating 4D tibiotalar JSW are described in the sequel of this chapter.

### 4.3.1 Fast Eulerian PDE approach

#### 4.3.1.1 The Laplace equation

Measuring thickness of deformable tissues, bounded by two non-intersecting surfaces, has been approached by applying Laplace's Equation from mathematical physics [70]. Solving this computational problem is based on the solution of the following three-dimensional Laplace's Equation between the inner and outer surfaces, that we will call  $B_{in}$  and  $B_{out}$ , respectively:

$$\Delta u = \frac{\partial^2 u}{\partial x^2} + \frac{\partial^2 u}{\partial y^2} + \frac{\partial^2 u}{\partial z^2} = 0 \quad (4.1)$$

where  $u : \mathbb{R}^3 \rightarrow \mathbb{R}$  is a *scalar field*, also called *harmonic interpolant* or *harmonic function* which is a twice continuously differentiable function that satisfies Laplace's equation. This second-order partial differential equation (PDE), also known as the *heat equation* or the *equilibrium equation*, has been employed for handling many classical physical phenomena such as incompressible fluid flow, electrostatic fields for particle acceleration, and thermodynamic flows [70].

In electromagnetic theory for example, the electric field  $E$  satisfies the equation  $-\nabla\phi = E$  where  $\phi$  represents the *electric potential*. Then according to Gauss's law (first Maxwell's equation),  $E$  satisfies  $\nabla \cdot E = \frac{\rho}{\epsilon_0}$  for a particular charge density  $\rho$  ( $\epsilon_0$  is the electric constant) so that  $\phi$  satisfies  $\nabla^2\phi = \frac{\rho}{\epsilon_0}$ . Consequently,  $\phi$  satisfies the Laplace equation  $\nabla^2\phi = \Delta\phi = 0$  in a charge-free surface area (*i.e.* when  $\rho = 0$ ). In this case, the *electric potential*  $\phi$  corresponds to the *harmonic function*  $u$ , previously mentioned.

#### 4.3.1.2 Numerical solution of Laplace's equation

The solution of Equation (4.1) can be approximated inside an area  $R$ , bounded by  $B_{in}$  and  $B_{out}$ , using standard numerical methods like the finite difference method, involving low order Taylor series expansions [119].

In this thesis, we have used an iterative relaxation method (also called the Jacobi iterative method) which is simple to implement and numerically robust:

$$u_{i+1}(x, y, z) = \frac{1}{6} [u_i(x + dx, y, z) + u_i(x - dx, y, z) + u_i(x, y + dy, z) + u_i(x, y - dy, z) + u_i(x, y, z + dz) + u_i(x, y, z - dz)] \quad (4.2)$$

where  $u_i(x, y, z)$  is the value of the scalar field  $u$  at point  $(x, y, z)$  during the  $i^{th}$  iteration;  $dx$ ,  $dy$ , and  $dz$  are the voxel spacing values in the  $x$ ,  $y$  and  $z$  directions,

respectively. Each iteration is quite fast as the computations are performed simultaneously at all points and only inside  $R$ . The initial Dirichlet boundary conditions are  $u(B_{in}) = 0$  and  $u(B_{out}) = n$ ,  $n \in \mathbb{N}_+^*$  (e.g.  $n = 100$ ).

**Convergence criterion:** *Jones et al.* [70] proposed a convergence criterion based on the total field energy over all grid voxels:

$$\varepsilon_i = \sum_{\text{voxels}} \sqrt{\left(\frac{\Delta u_i}{dx}\right)^2 + \left(\frac{\Delta u_i}{dy}\right)^2 + \left(\frac{\Delta u_i}{dz}\right)^2} \quad (4.3)$$

where:  $\frac{\Delta u_i}{dx} = \frac{1}{2}[u - i(x + dx, yz) - u_i(x - dx, y, z)]$ . And then the Jacobi iterative method converges when the ratio  $\frac{\varepsilon_i - \varepsilon_{i+1}}{\varepsilon_i}$  becomes smaller than a user-defined threshold (typically about  $10^{-5}$ ). The main limitation of this convergence criterion is that it requires a repeated evaluation of Equation (4.3) in each iteration which increases the computation times. As an example, *Jones et al.* suggested that 200 iterations are sufficient to calculate the cortical thickness using MRI data with a resolution of  $0.5 \times 0.5 \times 0.5mm$ . In this work, we preferred to keep the number of iterations as a user-defined parameter in order to optimize the computation schemes. By default, the total number of iterations is set to 200 for solving the Laplace Equation, and to 100 iterations for solving the pair of PDEs according to Equations (4.7) and (4.8) (i.e. via the iterative Gauss-Seidel method).

#### 4.3.1.3 Normalized gradient vector flow field

The normalized gradient vector flow field  $\vec{N}$  is then computed from  $u$  with 3D finite differences, this coincides with the tangent vector field of the correspondence trajectories:

$$\vec{N} = \frac{\nabla u}{\|\nabla u\|_2} = \begin{pmatrix} N_x \\ N_y \\ N_z \end{pmatrix} \quad (4.4)$$

where:  $\nabla u = \begin{pmatrix} \frac{\partial u}{\partial x} \\ \frac{\partial u}{\partial y} \\ \frac{\partial u}{\partial z} \end{pmatrix}$  is the gradient vector; and  $\|\nabla u\|_2 = \sqrt{\left(\frac{\partial u}{\partial x}\right)^2 + \left(\frac{\partial u}{\partial y}\right)^2 + \left(\frac{\partial u}{\partial z}\right)^2}$

is the gradient Euclidean norm.

#### 4.3.1.4 PDE formulation

Once the normalized gradient vector flow is computed, it is then possible to compute the two correspondence trajectories at each point  $p = (x, y, z)$  inside  $R$ :  $L_0$  between

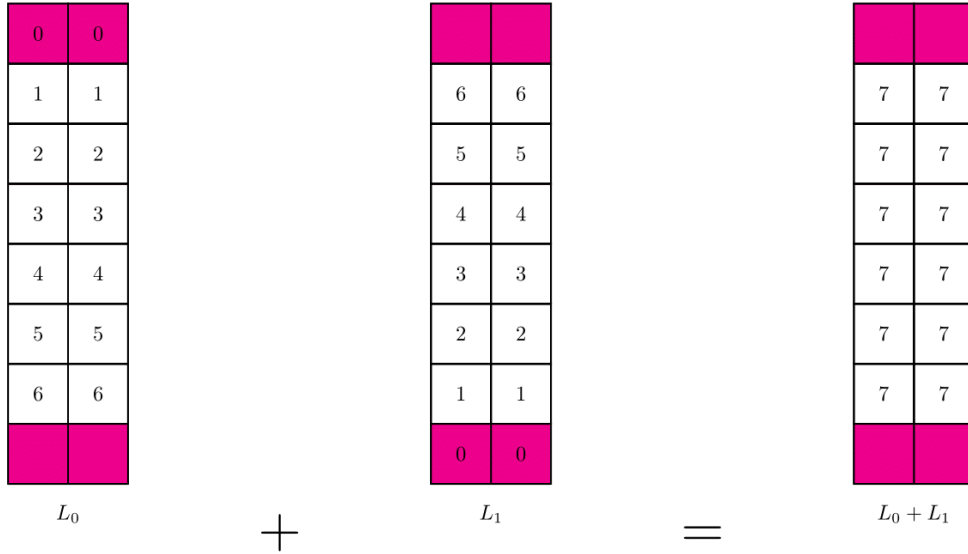


Figure 4.2: Overestimation of the thickness  $W = L_0 + L_1$  when initializing the boundary conditions for computing  $L_0$  and  $L_1$  at 0. The real thickness value is equal to 6 while the estimated thickness value is 7.

$p$  and the inner boundary  $B_{in}$ , and  $L_1$  between  $p$  and the outer boundary  $B_{out}$ . This step consists of solving the following pair of PDEs (Eq 4.5 and Eq 4.6):

$$\nabla L_0 \cdot \vec{N} = 1 \quad ; \quad \text{initialized with } L_0 = L_1 = -\frac{(dx + dy + dz)}{6} \quad (4.5)$$

$$-\nabla L_1 \cdot \vec{N} = 1 \quad ; \quad \text{initialized with } L_0 = L_1 = -\frac{(dx + dy + dz)}{6} \quad (4.6)$$

where:  $\vec{v}_1 \cdot \vec{v}_2$  is the usual dot product or the Euclidean inner product between  $\vec{v}_1$  and  $\vec{v}_2$ . Note that this setting of boundary conditions [2] gives more accurate thickness values when compared to the one used by *Yezzi et al.* [145], in which  $L_0$  and  $L_1$  are both fixed to 0 at all grid points before solving PDEs (4.5) and (4.6) over  $R$ , under the assumption that the boundaries coincide with the center of the grid points, which leads to an overestimation of the thickness as illustrated in Figure 4.2. To reduce this estimation bias, *Diep et al.* [41] proposed this new initialization of  $L_0$  and  $L_1$  (as in Eqs (4.5) and (4.6) in such a way that the boundaries coincide with voxel borders. Note that this new initialization yields more accurate results and it can produce the exact thickness in the ideal cases (*i.e.*, for isotropic images as illustrated in Figure 4.3).

A parallel iterative relaxation method is used for solving this pair of PDEs, so that  $L_0$  and  $L_1$  are *updated simultaneously* inside  $R$  using Gauss-Seidel method [145], which is one of the most sophisticated relaxation methods as it converges twice as

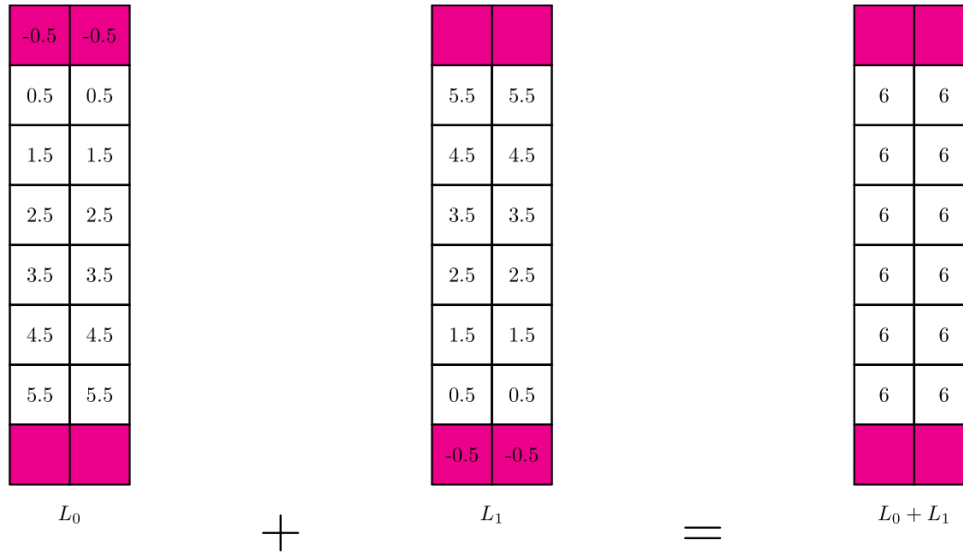


Figure 4.3: Estimation of the thickness  $W = L_0 + L_1$ , in the case of isotropic resolution (voxel size of  $1 \times 1 \times 1mm$ ), when initializing the boundary conditions for computing  $L_0$  and  $L_1$  according to [41].

fast as Jacobi [58], according to Equations (4.7) and (4.8):

$$L_0^{i+1}[x, y, z] = \frac{1 + |N_x| L_0^i[x \mp 1, y, z] + |N_y| L_0^i[x, y \mp 1, z] + |N_z| L_0^i[x, y, z \mp 1]}{|N_x| + |N_y| + |N_z|} \quad (4.7)$$

$$L_1^{i+1}[x, y, z] = \frac{1 + |N_x| L_1^i[x \pm 1, y, z] + |N_y| L_1^i[x, y \pm 1, z] + |N_z| L_1^i[x, y, z \pm 1]}{|N_x| + |N_y| + |N_z|} \quad (4.8)$$

$$\text{where: } \begin{cases} x \pm 1 = x + \text{sgn}(N_x) & ; & x \mp 1 = x - \text{sgn}(N_x) \\ y \pm 1 = y + \text{sgn}(N_y) & ; & y \mp 1 = y - \text{sgn}(N_y) \\ z \pm 1 = z + \text{sgn}(N_z) & ; & z \mp 1 = z - \text{sgn}(N_z) \end{cases}$$

with:  $\text{sgn}(a)$  is the sign function in  $\mathbb{R}^*$ .  $\text{sgn}(a) = \begin{cases} +1 & \text{if } a > 0 \\ -1 & \text{if } a < 0 \end{cases}$ , and  $i$  is the iteration index.

**Explication of the PDE formulation:**

Let's take the first equation  $\nabla L_0 \cdot \vec{N} = 1$  as example, this PDE suggests that the elementary displacement of the optimal path between each point  $p \in R$  and the outer boundary coincides with the normalized tangent vector to the harmonic

interpolant at this point.

Let  $\vec{u}$  and  $\vec{v}$  be two Euclidean vectors, then their dot product that we note  $\vec{u} \cdot \vec{v}$  is defined by:

$$\vec{u} \cdot \vec{v} = \|\vec{u}\| \cdot \|\vec{v}\| \cdot \cos(\theta) \quad (4.9)$$

where  $\theta$  is the angle between  $\vec{u}$  and  $\vec{v}$ .

$$if \left\{ \begin{array}{l} \vec{u} \cdot \vec{v} = 1 \\ \theta = 0 \\ \|\vec{v}\| = 1 \end{array} \right. \quad then \quad \vec{u} = \vec{v}$$

If we replace now  $\vec{u}$  with  $\nabla L_0$  and  $\vec{v}$  with  $\vec{N}$ , we can directly prove the coincidence between  $\nabla L_0$  and  $\vec{N}$  (*i.e.*  $\nabla L_0 = \vec{N}$ ), if  $\nabla L_0 \cdot \vec{N} = 1$ .

Idem for integrating the optimal path between each point  $p \in R$  and the inner boundary:  $\nabla L_1 \cdot \vec{N} = -1$  is satisfied if  $\theta = \pi$  in Eq (4.9).

Since  $L_0$  and  $L_1$  may never intersect (as they start from opposite endpoints in opposite boundaries), the thickness  $W(p)$  inside  $R$  can be computed from the tangent field  $\vec{N}$  by adding these two correspondence trajectories yielding a unique value at each voxel  $p$  inside  $R$  as follows:

$$W(p) = L_0(p) + L_1(p) \quad (4.10)$$

As an extension of this described Eulerian Framework, *Rocha et al.* have presented an hybrid Eulerian-Lagrangian approach [117] for measuring soft tissue thickness in which the speed of the Eulerian PDE approach is complemented by the accuracy of the Lagrangian approach.

### 4.3.2 Experiments

We have implemented the Eulerian PDE approach and then we have applied it to different applications, including both simulated synthetic and real MR images as entries. Satisfactory results are achieved in terms of accuracies and computation times across applications:

- **Simulation 1:** Measuring thickness inside a synthetic circular annulus.
- **Simulation 2:** Measuring thickness inside a synthetic 3D sphere.
- **Application 1:** Estimation of 3D bone width.
- **Application 2:** Computation of joint space width (JSW) by combining static MRI with dynamic MRI (main application in this thesis, section 4.4.2).

- **Application 3:** Estimation of 3D cortical thickness from MRI scans (Appendix A).

**Simulation 1:** In this experience, we have simulated a circular annulus  $C_a$  with inner radius of 50 voxels, and outer radius of 65 voxels. Inner and outer boundaries are fixed to  $10^4$  and 0, respectively. Figure 4.4 shows the obtained thickness results between the two boundaries. This setting is motivated by the fact that normal tibiotalar joint space area varies from 10 to 17 voxels in the static MRI image. The obtained thickness values using the Eulerian computational framework are around  $15.2 \pm 0.4$  voxels (after only 100 iterations for the Jacobi iterative relaxation method and 50 iterations for the Gauss-Seidel relaxation method). Compared to  $15.1 \pm 0.2$  voxels (after 200 iterations for the Jacobi iterative relaxation method and 100 iterations for the Gauss-Seidel relaxation method).

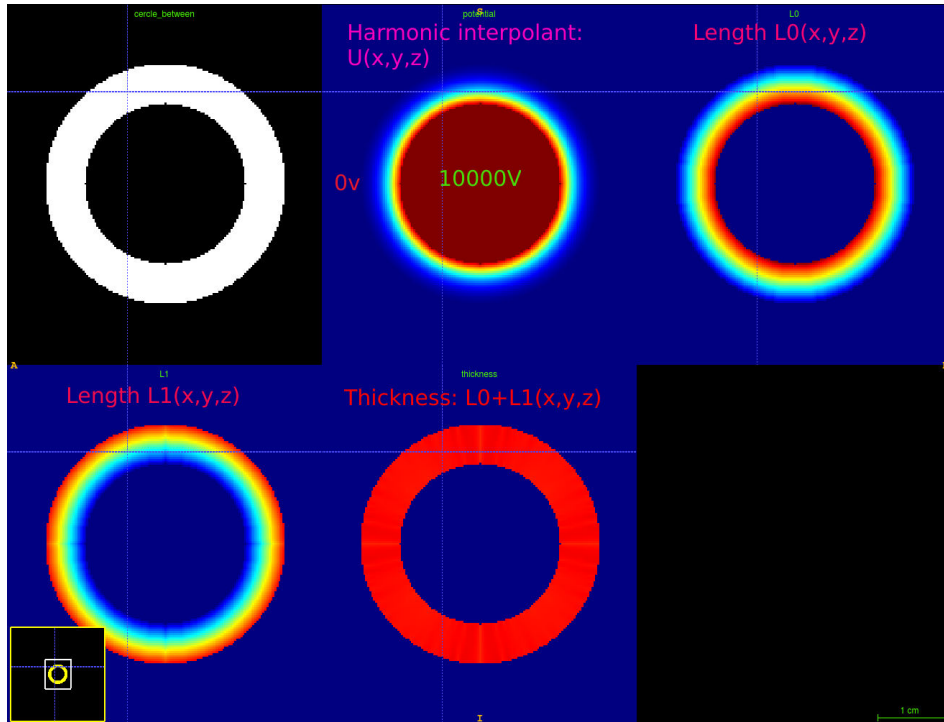


Figure 4.4: Computation of thickness for a circular annulus  $C_a$  (white region in the top left) with inner radius of 50 voxels, and outer radius of 65 voxels. The theoretical thickness value should be equal to 15 inside  $C_a$  (*i.e.* the difference between the two radius). The obtained values using the Eulerian computational framework are effectively around  $15.1 \pm 0.2$  voxels.

**Simulation 2:** The aim of this experience is to test our algorithm on three dimensional synthetic data. Let's consider a sphere  $S$  with center  $c$  at  $(x_0, x_1, x_2)$  and a radius  $r$  voxels, then the general equation of  $S$  is:  $(x - x_0)^2 + (y - y_0)^2 + (z - z_0)^2 = r^2$ . The underlying assumption is that the thickness values should be equal

to the radius over the sphere voxels.

We propose, then, to measure the sphere thickness using the Eulerian approach by first solving the Laplace equation between the sphere center  $c$  (inner boundary) and the sphere edges (*i.e.* by considering  $\bar{S}$  as outer boundary). To do this, we have generated a sphere  $S$  with center  $c = (64, 64, 64)$  and radius  $r = 50$  in a regular grid of  $128 \times 128 \times 128$  voxels and with an isotropic resolution (voxel size of  $1 \times 1 \times 1mm$ ), according to:

$$S(x, y, z) = \begin{cases} 1, & \text{if } (x - 64)^2 + (y - 64)^2 + (z - 64)^2 \leq 50^2 \\ 0, & \text{otherwise.} \end{cases} \quad (4.11)$$

Figure 4.5 shows that the solution of Laplace’s equation  $\Delta u = 0$  inside  $S$  divides the sphere into a set of equivalued sub-layer volumes; while Figure 4.6 shows the corresponding tangent vector field; and Figure 4.7 shows the resulting thickness map inside the simulated sphere. The obtained thickness values inside  $S$  using our implementation are effectively around  $49 \pm 1mm$  (as shown in Figure 4.7) because the inner boundary (*i.e.*, the sphere center) is dilated by one voxel in each direction. Furthermore, the thickness map can be smoothed (by smoothing the simulated sphere shape). However, we preferred to estimate the thickness map under realistic conditions since the smoothing of bone masks can affect the bone shapes in the context of our main application which is the estimation of JSW.

**Application 1:** Quantification of bone width: this application can be helpful in studying bone development and growth during a large period of time (in developing children MRI data), or for performing statistical analysis of bone shape across subjects by taking into account this interesting morphological feature. In this context, we represent the 3D bone width as the distance map between its center of mass  $G$  (*i.e.* the centroid of bone shape) and each surface point (*i.e.* the bone edges).  $G$  is defined as the arithmetic mean of all the points  $p_1 \dots p_n$  in the bone shape, then the bone centroid is given by:

$$G = \frac{1}{n} \sum_{i=1}^n p_i \quad (4.12)$$

To do this, we consider the center  $G$  as inner Dirichlet boundary and the complementary binary mask  $\bar{B} = \max\{B\} - B$  (with  $B$  is the binary mask of the bone) as outer Dirichlet boundary. And then we compute the thickness using the proposed Eulerian Framework. The resulting distance map is presented in Figure 4.8. Note that the quantification of bone width is beyond the scope of this work but it can be targeted in future works to detect the morphological deformities for children with spastic equinus.

#### 4.4 Spatio-temporal evolution of the JSW

The proposed approach for measuring JSW consists in three steps which are described in the next sections: 1) estimating spatio-temporal bone rigid transforma-

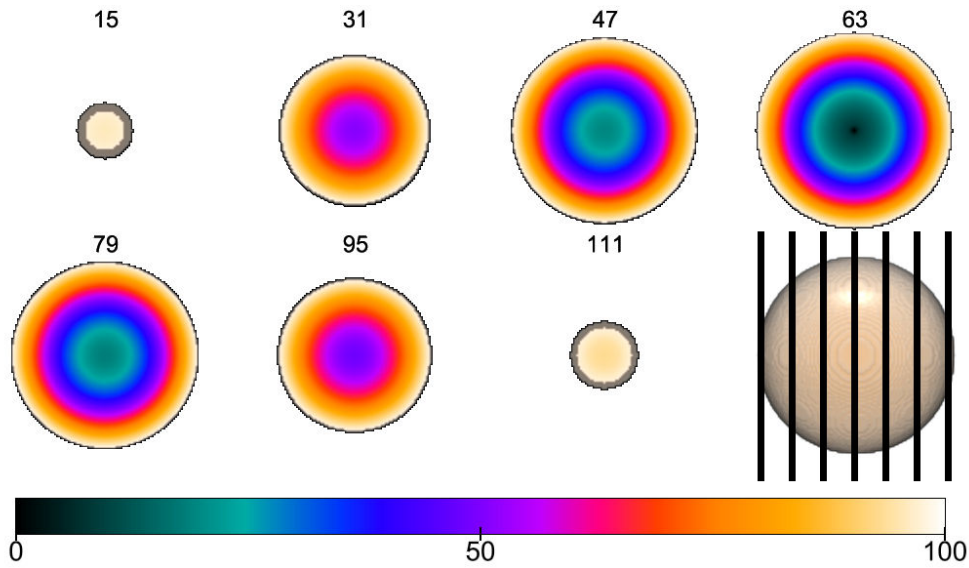


Figure 4.5: Three-dimensional solution of Laplace's equation (that gives the *harmonic interpolant*) inside the synthetic sphere  $S$  ( *i.e.* between its center  $c$  and its surfaces) using the Jacobi iterative method (1000 iterations within  $37sec$ ). The initial Dirichlet boundary conditions are set as follows:  $u(c) = 0$  and  $u(\bar{S}) = 100$ . This experience aims to verify later, that the thickness value at each point  $p = (x_p, y_p, z_p)$  inside the sphere is exactly equal to the sphere radius  $r$ . Seven cross slices (between 15 and 111) are presented in this figure showing the solution of the Laplace equation inside  $S$ .

tions (this step is detailed in our previous works [88, 90]), 2) computing spatio-temporal non-rigid deformations of the entire joint space area, localized between the two bones composing the joint of interest (Section 4.4.1), 3) computing the JSW using the above-described Eulerian PDE approach where bones are considered as Dirichlet boundaries (Section 4.4.2). Steps 2 and 3 are repeated for each time frame to quantify the temporal JSW in the high-resolution space.

#### 4.4.1 Temporal tracking of joint space area

Since articular cartilages undergo non-linear deformations during motion, we propose to smoothly track the entire joint space area using diffeomorphic registration, instead of rigidly track each of the two cartilage layers separately.

Following previous works [53, 65], we define the tibiotalar joint space (the area inside which the thickness will be measured) in healthy feet as the space between the upper surface of the talus and the inferior articular surface of the tibia. The joint space area is manually segmented in the static image and then automatically tracked throughout the dynamic sequence using non-rigid registration. Tracking the joint space area throughout the ankle trajectory is a challenging task because articular cartilages are soft tissues that undergo non-linear deformations contrary to the rigid

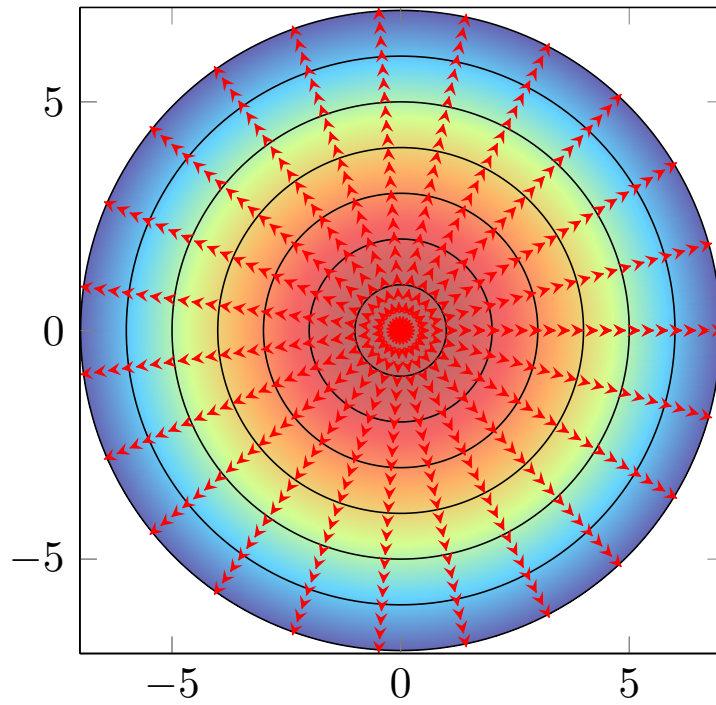


Figure 4.6: The harmonic function  $u$  and the corresponding *smooth* tangent field  $\vec{N} = \frac{\nabla u}{\|\nabla u\|}$  inside a synthetic sphere. The harmonic function is obtained by solving the Laplace equation inside the sphere. Note that we have inverted the two boundaries here. So that the initial Dirichlet boundary conditions are set as follows:  $u(c) = 100$  and  $u(\bar{S}) = 0$ . This experience shows the heat propagation from the sphere center or nucleus to its external surfaces.

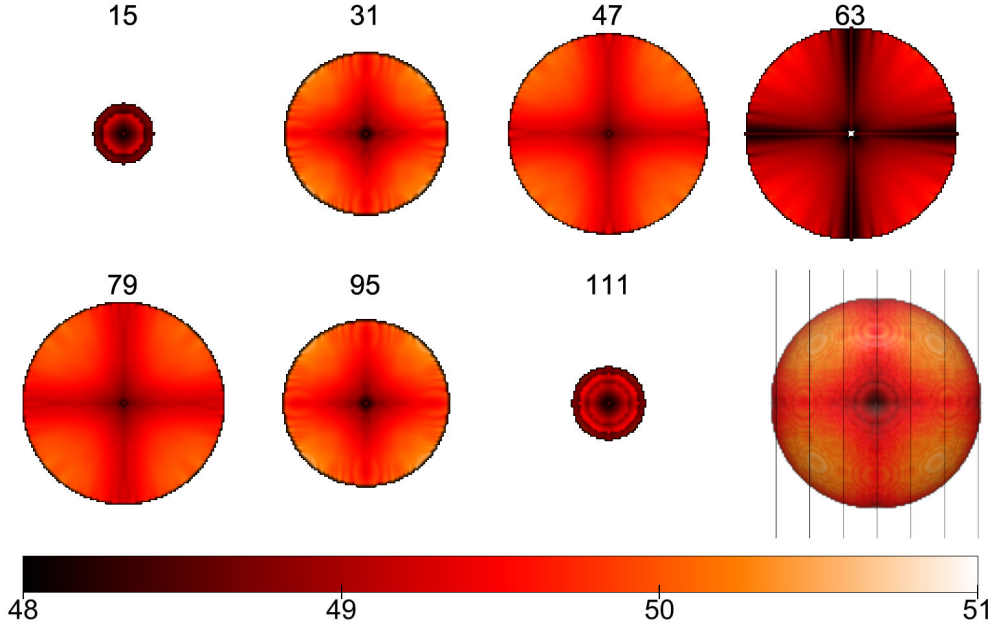


Figure 4.7: 3D thickness map inside the simulated sphere (in  $mm$ ).

bones. In this work, we propose to compute the local spatio-temporal deformations of this area using the LEPF. The segmentations of the two bones, composing the joint of interest, are used to compute the spatial weighting functions  $\{w^i(x)\}_{i \in \{1,2\}}$ .

#### 4.4.2 Computation of temporal joint space width

Given the position of each bone and each joint space area  $(R_k)_{k \in \{1 \dots K\}}$  at each time frame  $D_k$ , the time-dependent width of the entire joint space separating two neighboring bones can be computed with high accuracy using the presented Eulerian framework [145]. The JSW is computed by first solving the Laplace's equation ( $\Delta u_k = 0$ ) inside the surface between two bones ( $R_k$ ) using the Jacobi iterative method. Bones are considered as Dirichlet boundaries so that they are set to fixed potentials ( $u_k = 0V$  for the inner boundary and  $u_k = 100V$  for the outer boundary). The potential is set to zero at all grid points outside the joint segmentation (including the joint space area) to connect the two boundaries as shown in Figure 4.10.a in such a way that these values will serve as inner boundary condition. Solving this second order PDE gives the harmonic interpolant  $u_k$  which divides the joint space area into a set of equipotential sub-layers as illustrated in Figure 4.10.a.

In this application,  $L_0$  and  $L_1$  are first initialized to  $-\frac{(dx+dy+dz)}{6}$  at all grid points and then iteratively *updated* only over  $R_k$  using the Gauss-Seidel method [145] according to Equations (4.7) and (4.8):

Since  $L_0$  and  $L_1$  may never intersect (as they start from opposite endpoints in

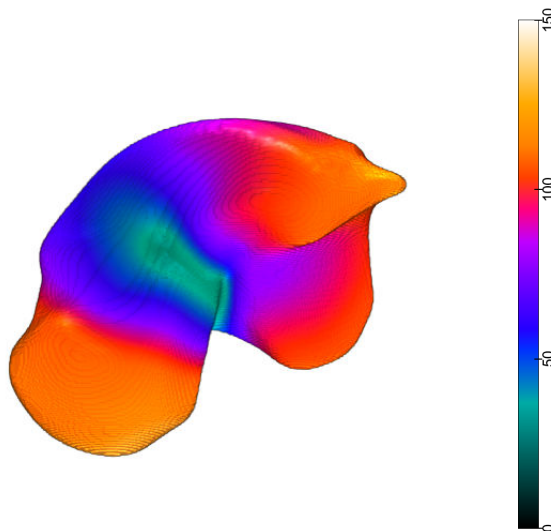


Figure 4.8: Talar width in voxels

opposite bones), the thickness  $W_k(p)$  inside  $R_k$  is computed from the tangent field by adding these two correspondence trajectories yielding a unique value at each voxel  $p$  inside  $R_k$  as follows:

$$W_k(p) = L_0(p) + L_1(p) \quad (4.13)$$

The width computation scheme is detailed in Algorithm 3, with the following notations:  $B_k^1$  and  $B_k^2$  are the two neighboring bones composing the joint of interest (the inner and outer boundaries) at time frame  $D_k$ ;  $\vec{N}_k$  is the normalized gradient of the Laplace solution  $u_k$ ;  $L_{0_k}$  gives the arclength of the correspondence trajectory between the bone  $B_k^1$  and  $p$ , while  $L_{1_k}$  gives the arclength of the correspondence trajectory between the bone  $B_k^2$  and  $p$ , for each voxel  $p$  inside the joint space area ( $R_k$ );  $dx$ ,  $dy$  and  $dz$  are the voxel spacing values in the  $x$ ,  $y$  and  $z$  directions, respectively.

## 4.5 Validation

The accuracies of bone motion estimation have been presented in [90] using DICE score. In this work, we have also quantified the accuracy of joint space area tracking. To do this, we have computed the overlap between automatic (or propagated) and ground-truth (or manual) segmentations of the joint space section at each time frame using the Dice coefficient. The temporal Dice scores across all subjects was around  $0.9 \pm 0.03$ , indicating that the joint space area is accurately tracked over the entire ankle trajectory.

<sup>1</sup>The source code is available on GitHub: <https://github.com/rousseau/dynMRI>.

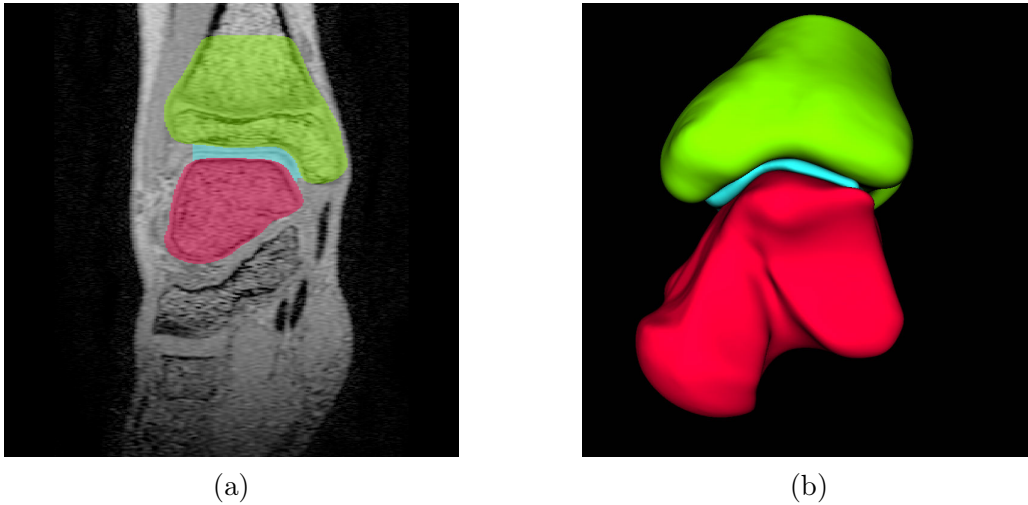


Figure 4.9: Segmentation of the tibiotalar joint. Regions of interest are: tibia (green), talus (red), tibiotalar joint space (cyan). (a): Mid-coronal image from the high-resolution static image; (b) Three dimensional rendering of the joint.

## 4.6 Results

The volume of the tracked joint space area increased in the order of maximum dorsiflexion ( $183 \pm 10 \text{cm}^3$ ), neutral position ( $190 \pm 12 \text{cm}^3$ ), and maximum plantar flexion ( $196 \pm 13 \text{cm}^3$ ). The tibiotalar JSW is computed in  $22 \text{sec}$  on an Intel<sup>®</sup>.Xeon<sup>®</sup> Processor E3-1271 v3 3.60 GHz on a  $576 \times 576 \times 210$  grid (where the tracked joint space section contains  $12 \cdot 10^4$  points) using our optimized implementation of the Eulerian framework (figure 4.10). Figure 4.12 shows the estimated JSW values projected on bone contact surfaces (the second column corresponds to the tibial plafond while the third column corresponds to the talar superior contact surface) for several time frames for one healthy subject. It illustrates the temporal evolution of the three-dimensional JSW during passive motion for this subject. This Eulerian framework yields width values in a bijective way, as illustrated in columns 2 and 3 in Figure 4.12 and this is also illustrated in Figure 4.3, showing two mirror-symmetric temporal width maps which confirms the uniqueness of width value at each voxel between the two bones. From these temporal maps, we can extract temporal features for each subject to provide an average behavior of the JSW. Assuming the central area to be the center of rotation for the tibiotalar joint in healthy feet [65], we define the landmark  $P_1$  shown in figure 4.11 as the centroid of the joint-space-mesh. For each time-frame for each subject, we then compute the mean average of the JSW inside a sphere centered at  $P_1$  (with radius  $r = 20 \text{voxels} \simeq 5 \text{mm}$  and by taking into account only the voxels inside the joint space area).

All subjects followed consistent patterns of displacement (continuous passive motion). The medial JSW was around  $2.7 \pm 0.60 \text{mm}$  across all healthy ankles

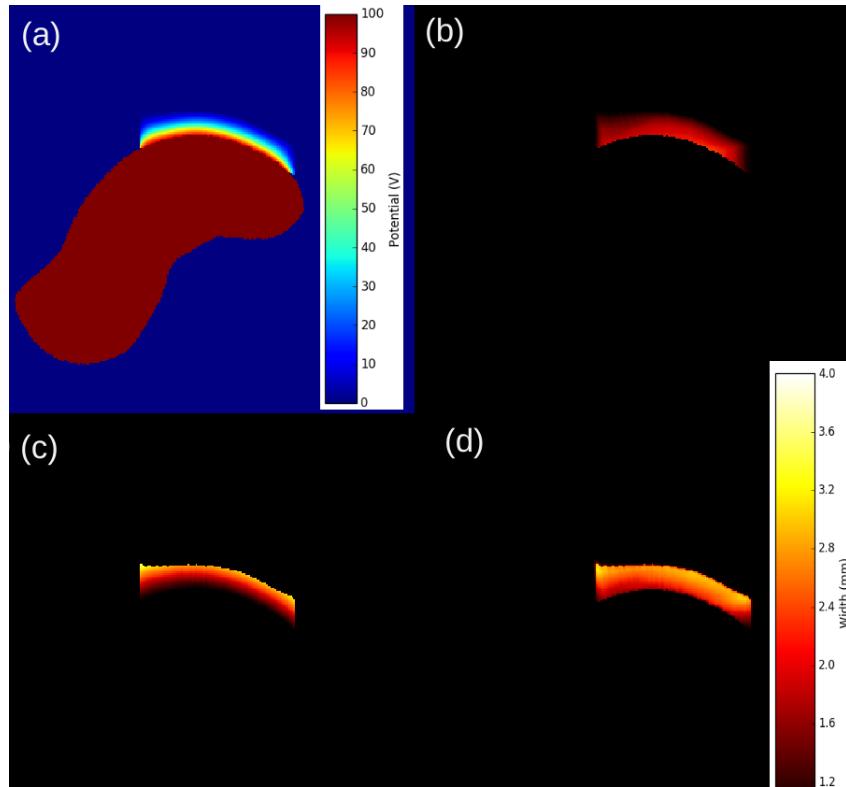


Figure 4.10: Calculation of 3-D width of the tibiotalar joint space. (a) Harmonic function  $u_1$ . (b) Length  $L_0$ . (c) Length  $L_1$ . (d) width  $(L_0 + L_1)$ : expressed in  $mm$  from one sagittal slice of the first reconstructed time frame (*i.e.* for  $k = 1$ ).

throughout the whole motion cycle. The lateral JSW was around  $3 \pm 0.60mm$ . Obtained measures demonstrate correspondance with the JSW measures presented in [65] for 10 healthy adults from stationary scans. In this work, the authors did not provide any details about the techniques they have used to measure the JSW making it difficult to perform objective comparisons in terms of measurement errors. Figure 4.11 shows the temporal mean feature of the JSW for all children during the whole ankle trajectory. Results demonstrate that the temporal evolution of contact area volume and the JSW around the centroid of the joint space section are highly correlated.

In our study, the JSW in the central part (area centred around point  $P1$ ) was not significantly different in any of the positions of the ankle joint while the normal ankle is moving (see Figure 4.12, thinner orange-yellow areas). In accordance with these results, the ankle moves in this middle position as a centre of rotation for the tibiotalar joint in healthy subjects. This also confirms the results of *Imai et al.* [65] for healthy adults, after dividing the tibial plafond into nine areas. Furthermore, previous works of *Borotikar et al.* [20, 19] were concentrated to only the highest stressed regions from the moving joint space section (*i.e.*, only overlapped

**Algorithm 3** Joint space width<sup>1</sup>1: **Inputs:**

- Bone segmentations  $B_k^1$  and  $B_k^2$ .
- Joint space area segmentation  $R_k$ .

2: **Iteratively solve the Laplace equation** ( $\Delta u_k = 0$ ) **over** ( $R_k$ ), **using Equation 4.2:** with the Dirichlet boundary conditions:  $u_k(B_k^1) = 0$  and  $u_k(B_k^2) = m$ , where  $m \in \mathbb{N}^*$ .

3: **Compute the normalized gradient vector flow field:**  $\vec{N}_k = \frac{\nabla u_k}{\|\nabla u_k\|_2}$ .

4: **Set**  $L_{0_k} = L_{1_k} = -\frac{(dx+dy+dz)}{6}$  **at all grid points (values outside**  $R_k$  **will serve as boundary conditions).**

5: **Iteratively update**  $L_{0_k}$  **and**  $L_{1_k}$  **via a parallel** *Iterative Relaxation* **method, according to Equations (4.7) and (4.8).**

6: **Compute the joint space width**  $\forall p$  **inside** ( $R_k$ ) :  $W_k(p) = L_{0_k}(p) + L_{1_k}(p)$ .

regions are highlighted). Hence, we propose a more complete framework in which the width information is provided over the entire joint space section (*i.e.* we propose a framework with enhanced spatio-temporal information).

## 4.7 Conclusion

In this chapter, we have presented a complete pipeline for measuring spatio-temporal JSW, providing qualitative visual supports and allowing quantitative data analysis. As shown in Figure 1.6, dynamic MRI comes with its own challenges such as low spatial resolution and anisotropy. This is the reason why we have combined spatial information provided by static MRI with temporal resolution of dynamic MRI sequences. The proposed approach relying on HR reconstructed dynamic sequences can provide 3D+t morphometric information throughout the whole motion. This work is the first attempt to track the entire joint space area and to evaluate JSWs without having to perform time-consuming manual segmentations. The proposed method provides a fast way to combine high-resolution spatial information with temporal dynamics of joints in order to establish normative contact mechanics. The Eulerian PDE approach provides an efficient and fast solution for quantifying widths of segmented areas, bounded by two bone masks. The results of this study are consistent with previous works reporting discrete data at specific locations of the tibiotalar joint, which is the primary joint responsible for dorsi-plantar flexion of the ankle. In future works, the proposed approach will be applied to a larger dataset to compare spatio-temporal evolution of the JSW of children with CP with age-matched healthy children.

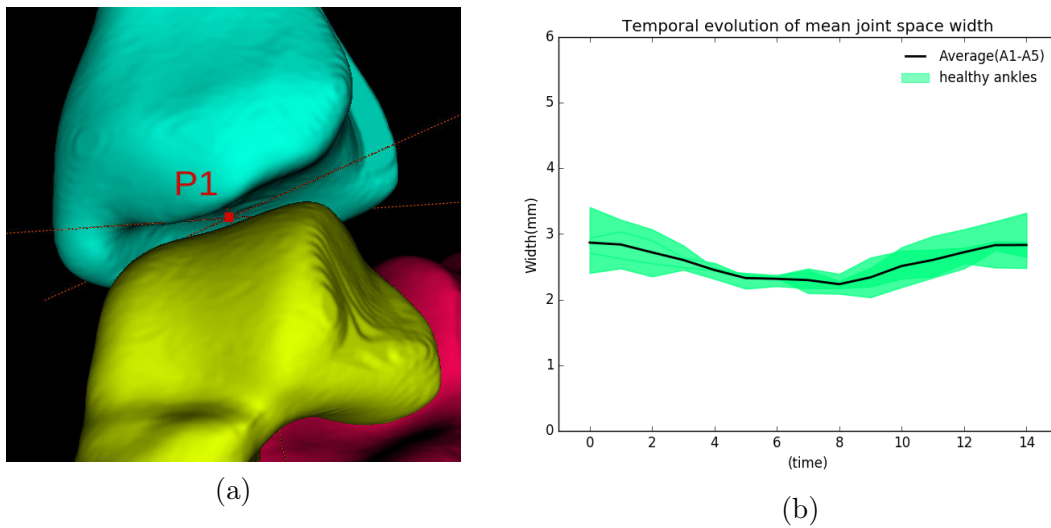


Figure 4.11: Temporal evolution of the JSW: (a) Location of the centroid of the joint space mesh points ( $P_1$ ); (b) temporal evolution of the JSW around  $P_1$ . The average across healthy subjects is shown as a solid line with one standard deviation above and below this line (grey shaded area).

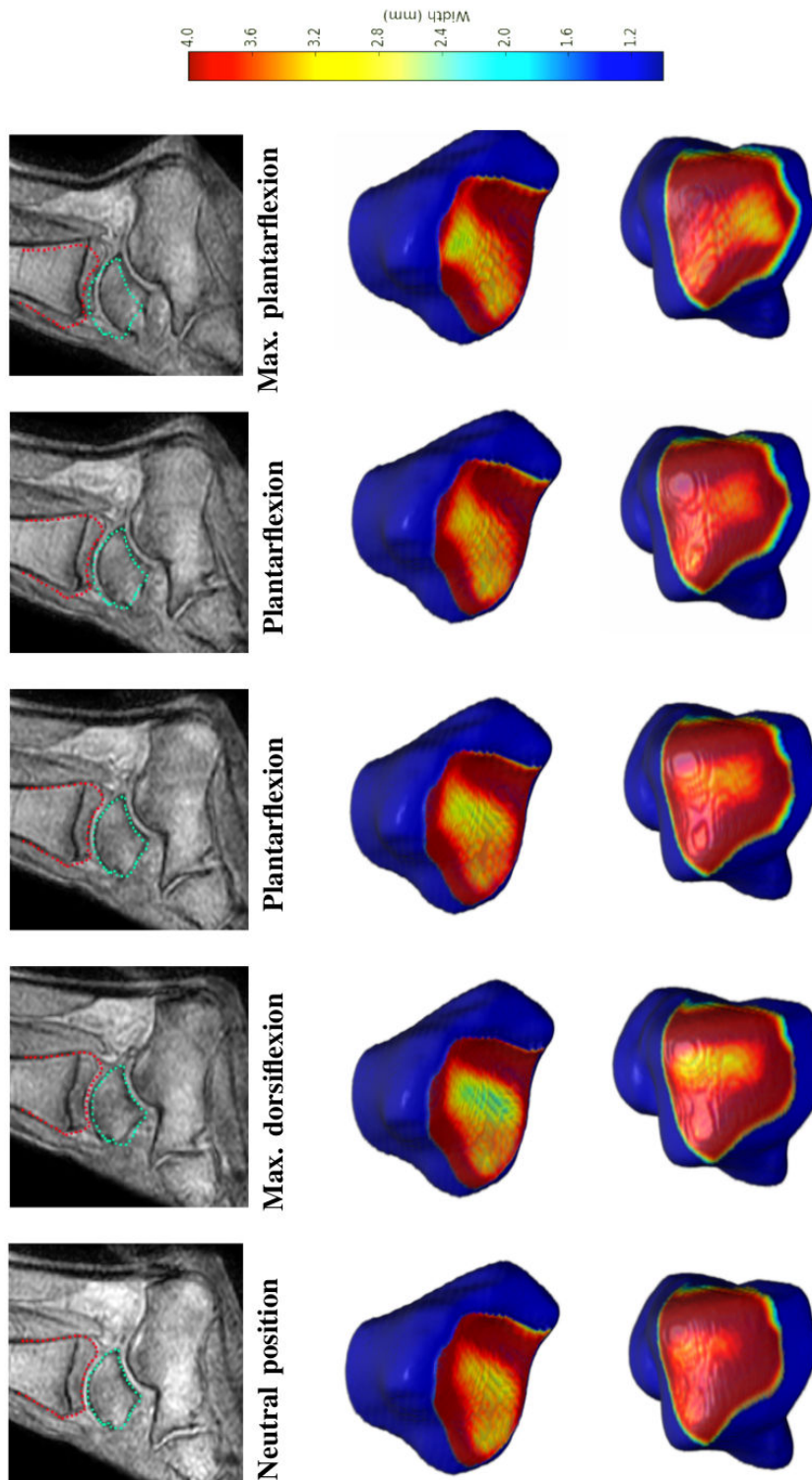


Figure 4.12: Spatio-temporal evolution of the tibiotalar JSW during motion. The first row is composed of a set of dynamic anatomical images from one healthy subject: bone contours in neutral position show the joint motion across time. Width values were projected on each bone contact surface (the second row corresponds to the tibial plafond while the third row corresponds to the talar superior contact surface).



# Conclusions & Perspectives

---

## Conclusions

Fast acquisition time, no need of repeated motions, and good soft tissue contrast are the key features that makes the proposed methods suitable for real-time evaluation of joint motion in vivo in normal and pathological conditions.

In the context of dynamic imaging, designing robust tracking methods is still an open issue. The principal difficulty encountered in the current work was the misregistrations happend when mapping estimation from the High-resolution static image to the dynamic sequence within a multi-resolution framework. this step is very important and it aims to find a link between the high-resolution static image and **at least** one low-resolution time frame from the corresponding dynamic sequence. The straightforward approach for doing that is to directly register the static image against each time frame using bone segmentations as weights. Unfortunately, this simple multi-resolution approach was not always sufficient for avoiding misregistrations caused by local minima in the cost function. For more technical details about the local minima problems, the reader is referred to Jenkinson's paper [66].

To overcome this difficulty, these multi-resolution registrations were carried out in two steps as detailed in Chapter 2.

The proposed method is robust to motion artifacts as well as image noise (see Figure 5.1).

One advantage of using FFE sequences is that they are more robust against motion artifacts. Contrary to the ICP algorithm proposed in [33], our algorithm is still robust despite reduced number of sagittal slices (only 6 compared to more than 8 in [33]).

One advantage of the log-euclidean polyrigid framework is that it ensures the invertibility of the final transformations, allowing us to go both forward and backward in time.

**FLIRT** (FMRIB's Linear Image Registration Tool) is a fully automated robust and accurate tool for linear (affine/rigid) intra- and inter-modal brain image registration. In this work, we have extended this tool to deal with non-linear image registration in the context of articulated structures. Although there exist different tools for non-linear or diffeomorphic image registration such as ANTs (Advanced Normalization Tools), they did not necessarily preserve bone shapes after the alignment process. So we have preferred to fuse the flirt transformations by the log

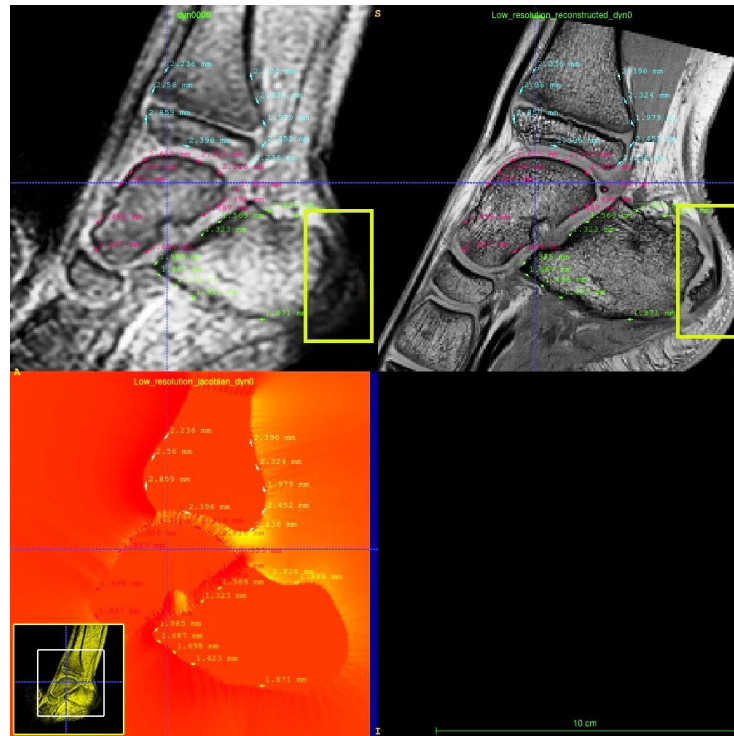


Figure 5.1: High-resolution reconstruction of one time frame using the proposed method. From up to down, from left to right: low-resolution time frame; reconstructed time frame; jacobian map of the deformation field from the static image to the acquired time frame.

euclidean polyrigid framework. As detailed in previous chapters, we proposed to compute a dense deformation field using matrix eigendecomposition. This technique is different from the scaling and squaring method used in previous works of Arsigny et al. [5] and Commowick et al [35]. The advantage of this technique is that it allows an **exact** computation of the matrix exponential contrary to the scaling and squaring method which **approximates** the matrix exponential with a certain level of accuracy. The algorithm that we propose in the current work improves both the speed and the accuracy of the log-euclidean fusion of multiple rigid transforms.

The main limitation of our method is the mis-registration of the bone when it is not wholly contained within the image FOV.

## Perspectives

This study provides crucial data for future studies of spastic equinus and cerebral palsy. Since spastic equinus was typically defined as the inability to dorsiflex the foot above plantigrade with the hindfoot in neutral position and the knee in extended position [72], we are interested in ankle joint kinematics during the dorsi-plantar flexion motion cycle and this is the reason why we constrain the foot

to a specific path using the fixture. The proposed approach will be further applied to a larger dataset to compare ankle joint kinematics of children with CP with age-matched healthy children.

We will also the method to other joints (shoulder/finger). Real-time dynamic MRI is a valid and reliable technique to evaluate joint motion with a good contrast between structures for T1-FFE sequence at the finger as shown in figure 5.2. This imaging modality allows an *in vivo* quantification of joint kinematics and an estimation of flexor digitorum profundus (FDP) tendon moment arm.

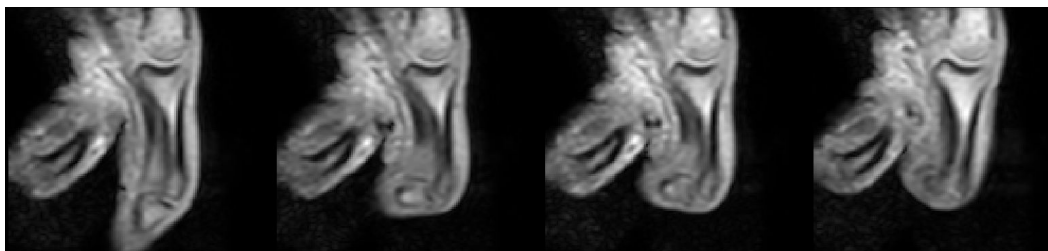


Figure 5.2: T1-FFE sequence of the finger joint during motion.

Another perspective will consist in automatically segmenting the bones of interest in the static data with the help of deep learning.

For better understanding of the joint mechanics and the interactions and dependencies between rigid and non rigid structures. A quantification of the temporal evolution of non rigid structures such as muscles and tendons is envisageable. A parametric diffeomorphic mapping between deformable shapes (points, curves, surfaces) is possible using the registration approach proposed in [42], which outputs: a set of control points near the most variable regions of the tracked organ, with a set of attached vectors parameterizing the deformations of the ambient space. These diffeomorphic mappings has been successfully employed to study the high morphological variability of organs such as those of the pelvic floor from 2D+t MRI sequences [115]. Similarly to the bones for which a continuous trajectory is estimated, a continuous-time trajectories for muscles and tendons can be also estimated.

## Acknowledgment

The research leading to these results has received funding from Région Bretagne, Chaire INSERM-IMT Atlantique, Fondation de l’Avenir, Fondation Motrice.

The author would like to thank François Rousseau and Douraid Ben Salem , who accepted me for this project in his research team. Thanks are also due to Marc Garetier and Hassen Affes for prolific discussions on the subject. Special thanks are also due to Bhushan Borotikar and Sylvain Brochard for sharing MRI data.



# Cortical thickness estimation

## A.1 Computation of neonatal cortical thickness

In the context of developing neonatal brain MRI segmentation, researchers proposed some robust algorithms such as the Expectation-maximization (EM) which is a statistic-based algorithm [91], and the iterative multi-atlas patch-based approach (IMAPA) [138]. However, the accuracy of the obtained cortical segmentations is limited due to the lower SNR, the partial volume effects, in addition to the large changes in brain shape in developing infants. In order to correct the MR brain image segmentation, a deformable model is presented in [schuh2017deformable]. Therefore, accurate cortical thickness estimation may help for segmentation correction with the use of this prior knowledge to constrain the deformation.

The computation of thickness inside the cortex (CX) is performed using the Eulerian PDE approach presented in chapter 4 ; white matter (WM) segmentation is considered as inner boundary while the complementary segmentation ( $\overline{CX + WM}$ ) is considered as outer Dirichlet boundary. Figure A.1 illustrates the definition of regions of interest (tissue region and Dirichlet boundaries) in a T2w axial MRI slice. The corresponding cortical thickness map is presented in Figure A.2.

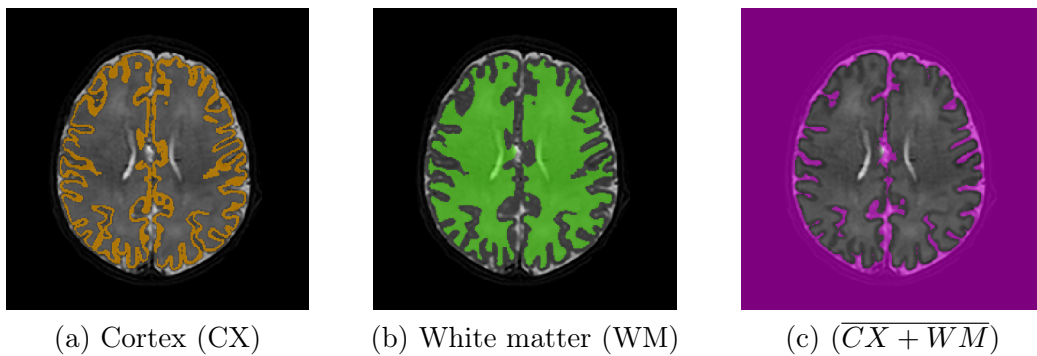


Figure A.1: Computation of 3D neonatal cortical thickness: (a) cortical gray matter segment (orange label, inside which the thickness will be computed); (b) white matter segment (green label, which will be considered as Dirichlet inner boundary); (c) complementary segment (purple label, which will be considered as Dirichlet outer boundary). Segmentations of cortex and white matter are performed using a fully automated processing pipeline [91], from a T2-weighted neonatal brain MRI. The voxel size of the image is  $0.5 \times 0.5 \times 0.5mm$ .

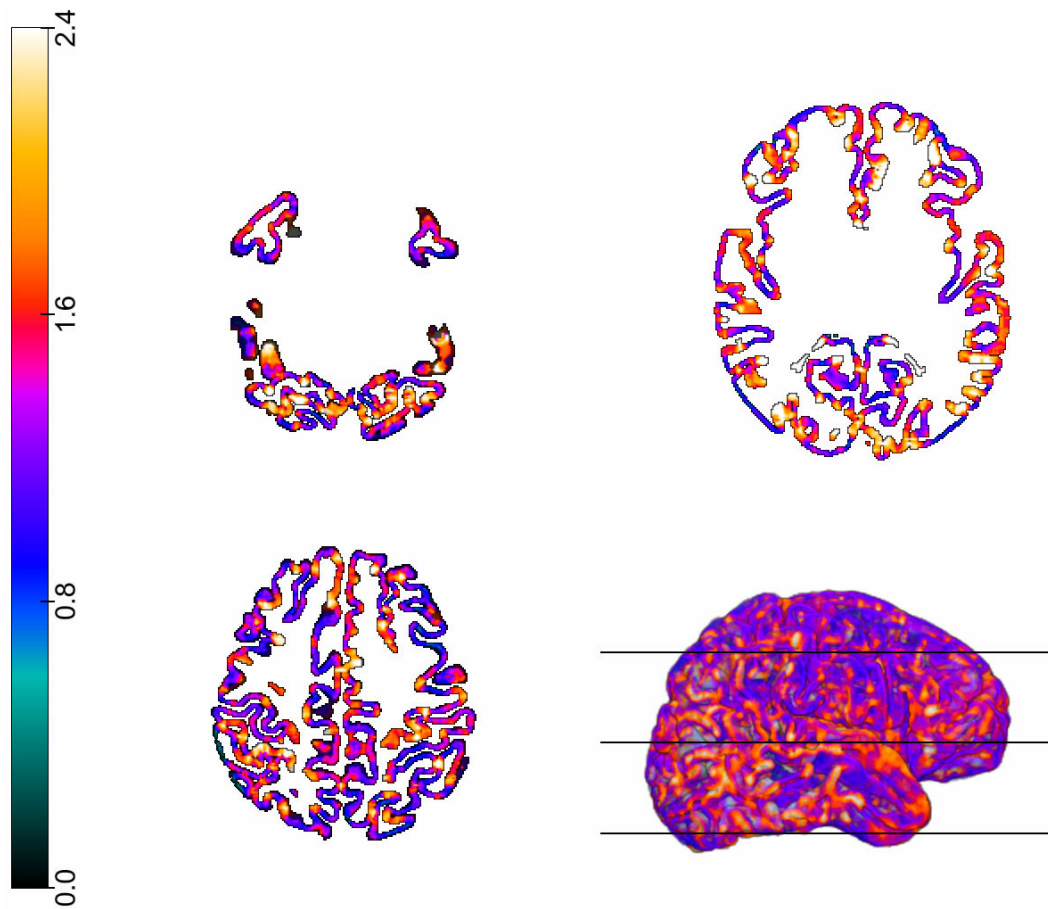


Figure A.2: Three-dimensional cortical thickness estimation. Thickness values are expressed in  $mm$ . As recommended in [70] for data with  $0.5 \times 0.5 \times 0.5 mm$  resolution, the total number of iterations for solving Laplace's equation is set to 200 (performed within 36sec on a regular grid of  $290 \times 290 \times 203$ ), giving very accurate thickness values inside the cortex in a bijective fashion. Three axial slices are shown to display the hidden information.

As a perspective, we can use this method to investigate the differences in cortical thickness between children with and without cerebral palsy using MRI data.

# Bibliography

- [1] B. Abbas, J. Fishbaugh, C. Petchprapa, R. Lattanzi, and G. Gerig, “Analysis of the kinematic motion of the wrist from 4d magnetic resonance imaging”, in *Medical Imaging 2019: Image Processing*, International Society for Optics and Photonics, vol. 10949, 2019, 109491E.
- [2] O. Acosta, P. Bourgeat, M. A. Zuluaga, J. Fripp, O. Salvado, S. Ourselin, A. D. N. Initiative, *et al.*, “Automated voxel-based 3d cortical thickness measurement in a combined lagrangian–eulerian pde approach using partial volume maps”, *Medical image analysis*, vol. 13, no. 5, pp. 730–743, 2009.
- [3] J. T. Alanen, J. V. Levola, H. Y. Helenius, and M. H. Kvist, “Ankle joint complex mobility of children 7 to 14 years old”, *Journal of Pediatric Orthopaedics*, vol. 21, no. 6, pp. 731–737, 2001.
- [4] E. Anderson, Z. Bai, J. Dongarra, A. Greenbaum, A. McKenney, J. Du Croz, S. Hammarling, J. Demmel, C. Bischof, and D. Sorensen, “Lapack: a portable linear algebra library for high-performance computers”, in *Proceedings of the 1990 ACM/IEEE conference on Supercomputing*, IEEE Computer Society Press, 1990, pp. 2–11.
- [5] V. Arsigny, O. Commowick, N. Ayache, and X. Pennec, “A fast and log-euclidean polyaffine framework for locally linear registration”, *Journal of Mathematical Imaging and Vision*, vol. 33, no. 2, pp. 222–238, 2009.
- [6] V. Arsigny, P. Fillard, X. Pennec, and N. Ayache, “Log-euclidean metrics for fast and simple calculus on diffusion tensors”, *Magnetic Resonance in Medicine: An Official Journal of the International Society for Magnetic Resonance in Medicine*, vol. 56, no. 2, pp. 411–421, 2006.
- [7] V. Arsigny, X. Pennec, and N. Ayache, “Polyrigid and polyaffine transformations: a novel geometrical tool to deal with non-rigid deformations—application to the registration of histological slices”, *Medical image analysis*, vol. 9, no. 6, pp. 507–523, 2005.
- [8] B. B. Avants, N. Tustison, and G. Song, “Advanced normalization tools (ants)”, *Insight j*, vol. 2, pp. 1–35, 2009.
- [9] F. S. Azar, D. N. Metaxas, and M. D. Schnall, “A deformable finite element model of the breast for predicting mechanical deformations under external perturbations”, *Academic Radiology*, vol. 8, no. 10, pp. 965–975, 2001.
- [10] W. C. Bae, T. Ruangchajjatuporn, and C. B. Chung, “New techniques in MR imaging of the ankle and foot”, *Magnetic Resonance Imaging Clinics*, vol. 25, no. 1, pp. 211–225, 2017.
- [11] H. H. Banks, “Equinus and cerebral palsyâits management”, *Foot & ankle*, vol. 4, no. 3, pp. 149–159, 1983.

- [12] M. F. Beg, M. I. Miller, A. Trouvé, and L. Younes, “Computing large deformation metric mappings via geodesic flows of diffeomorphisms”, *International journal of computer vision*, vol. 61, no. 2, pp. 139–157, 2005.
- [13] A. J. Behnam, D. A. Herzka, and F. T. Sheehan, “Assessing the accuracy and precision of musculoskeletal motion tracking using Cine-PC MRI on a 3.0 Tesla platform”, *Journal of biomechanics*, vol. 44, no. 1, p. 193, 2011.
- [14] C. Belta and V. Kumar, “New metrics for trajectory generation and interpolation on  $se(3)$ ”,
- [15] J. Bert and G. Wagner Michael, “Computer-aided design with spatial rational b-spline motions”, *ASME Journal of Mechanical Design*, vol. 118, pp. 118–93, 1996.
- [16] W. H. Beyer, *Standard mathematical tables and formulae*. CRC press, 1991.
- [17] J.-L. Blanco, “A tutorial on  $se(3)$  transformation parameterizations and on-manifold optimization”, *University of Malaga, Tech. Rep.*, vol. 3, 2010.
- [18] B. Borotikar, M. Lempereur, M. Lelievre, V. Burdin, D. Ben Salem, and S. Brochard, “Dynamic MRI to quantify musculoskeletal motion: a systematic review of concurrent validity and reliability, and perspectives for evaluation of musculoskeletal disorders”, *PLoS One*, vol. 12, no. 12, e0189587, 2017.
- [19] B. S. Borotikar and F. T. Sheehan, “In vivo patellofemoral contact mechanics during active extension using a novel dynamic MRI-based methodology”, *Osteoarthritis and cartilage*, vol. 21, no. 12, pp. 1886–1894, 2013.
- [20] B. S. Borotikar, W. H. Sipprell III, E. E. Wible, and F. T. Sheehan, “A methodology to accurately quantify patellofemoral cartilage contact kinematics by combining 3D image shape registration and cine-PC MRI velocity data”, *Journal of biomechanics*, vol. 45, no. 6, pp. 1117–1122, 2012.
- [21] D. Borton, K. Walker, M. Pirpiris, G. Natrass, and H. Graham, “Isolated calf lengthening in cerebral palsy: outcome analysis of risk factors”, *The Journal of bone and joint surgery. British volume*, vol. 83, no. 3, pp. 364–370, 2001.
- [22] S. Boyd, J. Ronsky, D. Lichti, D. Salkauskas, and M. Chapman, “Joint surface modeling with thin-plate splines”, *Journal of Biomechanical Engineering*, vol. 121, no. 5, pp. 525–532, 1999.
- [23] C. L. Brockett and G. J. Chapman, “Biomechanics of the ankle”, *Orthopaedics and trauma*, vol. 30, no. 3, pp. 232–238, 2016.
- [24] C. Broit, “Optimal registration of deformed images”, 1981.
- [25] L. G. Brown, “A survey of image registration techniques”, *ACM computing surveys (CSUR)*, vol. 24, no. 4, pp. 325–376, 1992.
- [26] A. Burghardt, C. Lee, D. Kuo, S. Majumdar, J. Imboden, T. Link, and X. Li, “Quantitative in vivo HR-pQCT imaging of 3D wrist and metacarpophalangeal joint space width in rheumatoid arthritis”, *Annals of Biomedical Engineering*, vol. 41, no. 12, pp. 2553–2564, 2013.

- [27] J. R. Cardoso and F. S. Leite, "On computing real logarithms for matrices in the lie group of special euclidean motions in  $\mathbb{R}^n$ ", 1999.
- [28] N. Cedilnik, J. Duchateau, R. Dubois, P. Jaïs, H. Cochet, and M. Sermesant, "Vt scan: towards an efficient pipeline from computed tomography images to ventricular tachycardia ablation", in *International Conference on Functional Imaging and Modeling of the Heart*, Springer, 2017, pp. 271–279.
- [29] S. H. CHENG, N. J. HIGHAM, C. S. KENNEY, and A. J. LAUB, "Approximating the logarithm of a matrix to specified accuracy",
- [30] G. E. Christensen and H. J. Johnson, "Consistent image registration", *IEEE transactions on medical imaging*, vol. 20, no. 7, pp. 568–582, 2001.
- [31] G. E. Christensen, R. D. Rabbitt, and M. I. Miller, "Deformable templates using large deformation kinematics", *IEEE transactions on image processing*, vol. 5, no. 10, pp. 1435–1447, 1996.
- [32] C. Y. Chung, K. H. Sung, K. M. Lee, S. Y. Lee, I. H. Choi, T.-J. Cho, W. J. Yoo, and M. S. Park, "Recurrence of equinus foot deformity after tendo-achilles lengthening in patients with cerebral palsy", *Journal of Pediatric Orthopaedics*, vol. 35, no. 4, pp. 419–425, 2015.
- [33] E. Clarke, J. Martin, A. d'Entremont, M. Pandya, D. Wilson, and R. Herbert, "A non-invasive, 3d, dynamic MRI method for measuring muscle moment arms in vivo: demonstration in the human ankle joint and achilles tendon", *Medical Engineering & Physics*, vol. 37, no. 1, pp. 93–99, 2015.
- [34] O. Commowick, V. Arsigny, J. Costa, N. Ayache, and G. Malandain, "An efficient locally affine framework for the registration of anatomical structures", in *Biomedical Imaging: Nano to Macro, 2006. 3rd IEEE International Symposium on*, IEEE, 2006, pp. 478–481.
- [35] O. Commowick, V. Arsigny, A. Isambert, J. Costa, F. Dhermain, F. Bidault, P.-Y. Bondiau, N. Ayache, and G. Malandain, "An efficient locally affine framework for the smooth registration of anatomical structures", *Medical Image Analysis*, vol. 12, no. 4, pp. 427–441, 2008.
- [36] T. F. Cootes, C. J. Taylor, D. H. Cooper, and J. Graham, "Active shape models-their training and application", *Computer vision and image understanding*, vol. 61, no. 1, pp. 38–59, 1995.
- [37] W. R. Crum, T. Hartkens, and D. Hill, "Non-rigid image registration: theory and practice", *The British journal of radiology*, vol. 77, no. suppl\_2, S140–S153, 2004.
- [38] R. B. Davis III, S. Ounpuu, D. Tyburski, and J. R. Gage, "A gait analysis data collection and reduction technique", *Human movement science*, vol. 10, no. 5, pp. 575–587, 1991.
- [39] M. H. Davis, A. Khotanzad, D. P. Flamig, and S. E. Harms, "A physics-based coordinate transformation for 3-d image matching", *IEEE transactions on medical imaging*, vol. 16, no. 3, pp. 317–328, 1997.

- [40] L. E. DeFrate, S. Y. Kim-Wang, Z. A. Englander, and A. L. McNulty, "Osteoarthritis year in review 2018: mechanics", *Osteoarthritis and cartilage*, 2018.
- [41] T. Diep, P. Bourgeat, and S. Ourselin, "Efficient use of cerebral cortical thickness to correct brain MR segmentation.", in *IEEE ISBI*, 2007, pp. 592–595.
- [42] S. Durrleman, M. Prastawa, N. Charon, J. R. Korenberg, S. Joshi, G. Gerig, and A. Trounev, "Morphometry of anatomical shape complexes with dense deformations and sparse parameters", *NeuroImage*, vol. 101, pp. 35–49, 2014.
- [43] L. Feng, L. Axel, H. Chandarana, K. T. Block, D. K. Sodickson, and R. Otazo, "Xd-grasp: golden-angle radial mri with reconstruction of extra motion-state dimensions using compressed sensing", *Magnetic resonance in medicine*, vol. 75, no. 2, pp. 775–788, 2016.
- [44] G. B. Firth, E. Passmore, M. Sangeux, P. Thomason, J. Rodda, S. Donath, P. Selber, and H. K. Graham, "Multilevel surgery for equinus gait in children with spastic diplegic cerebral palsy: medium-term follow-up with gait analysis", *JBJS*, vol. 95, no. 10, pp. 931–938, 2013.
- [45] B. Fischer and J. Modersitzki, "Ill-posed medicine—an introduction to image registration", *Inverse Problems*, vol. 24, no. 3, p. 034008, 2008.
- [46] T. Flash and N. Hogan, "The coordination of arm movements: an experimentally confirmed mathematical model", *Journal of neuroscience*, vol. 5, no. 7, pp. 1688–1703, 1985.
- [47] J. Fripp, S. Crozier, S. Warfield, and S. Ourselin, "Automatic segmentation and quantitative analysis of the articular cartilages from magnetic resonance images of the knee", *IEEE Transactions on Medical Imaging*, vol. 29, no. 1, pp. 55–64, 2010.
- [48] J. R. GAGE, "A commitment to excellence and a willingness to change", *Developmental Medicine & Child Neurology*, vol. 33, no. 9, pp. 753–754, 1991.
- [49] U. Gamper, P. Boesiger, and S. Kozerke, "Compressed sensing in dynamic MRI", *Magnetic Resonance in Medicine: An Official Journal of the International Society for Magnetic Resonance in Medicine*, vol. 59, no. 2, pp. 365–373, 2008.
- [50] Q. Ge and B. Ravani, "Computer aided geometric design of motion interpolants", *Journal of Mechanical Design*, vol. 116, no. 3, pp. 756–762, 1994.
- [51] A. Ghosal *et al.*, "A note on the diagonalizability and the jordan form of the  $4 \times 4$  homogeneous transformation matrix", *Journal of Mechanical Design*, vol. 128, no. 6, pp. 1343–1348, 2006.
- [52] B. Glocker, N. Komodakis, N. Paragios, and N. Navab, "Approximated curvature penalty in non-rigid registration using pairwise mrfs", in *International Symposium on Visual Computing*, Springer, 2009, pp. 1101–1109.

- [53] B. Goker, E. Gonen, M. Demirag, and J. Block, “Quantification of the radiographic joint space width of the ankle”, *Clinical Orthopaedics and Related Research*®, vol. 467, no. 8, pp. 2083–2089, 2009.
- [54] M. Goldstein and D. C. Harper, “Management of cerebral palsy: equinus gait”, *Developmental Medicine and Child Neurology*, vol. 43, no. 8, pp. 563–569, 2001.
- [55] M. C. Gourdine-Shaw, B. M. Lamm, J. E. Herzenberg, and A. Bhave, “Equinus deformity in the pediatric patient: causes, evaluation, and management”, *Clinics in podiatric medicine and surgery*, vol. 27, no. 1, pp. 25–42, 2010.
- [56] R. Guillin, A. Marchand, A. Roux, E. Niederberger, and R. Duvauferrier, “Imaging of snapping phenomena”, *The British journal of radiology*, vol. 85, no. 1018, pp. 1343–1353, 2012.
- [57] W. R. Hamilton, *Elements of quaternions*. Longmans, Green, and Company, 1899, vol. 1.
- [58] P. B. Hansen, “Numerical solution of laplace’s equation”, 1992.
- [59] N. Haouchine, J. Dequidt, I. Peterlik, E. Kerrien, M.-O. Berger, and S. Cotin, “Image-guided simulation of heterogeneous tissue deformation for augmented reality during hepatic surgery”, in *2013 IEEE international symposium on mixed and augmented reality (ISMAR)*, IEEE, 2013, pp. 199–208.
- [60] J. E. Herzenberg, B. M. Lamm, C. Corwin, and J. Sekel, “Isolated recession of the gastrocnemius muscle: the baumann procedure”, *Foot & ankle international*, vol. 28, no. 11, pp. 1154–1159, 2007.
- [61] N. J. Higham, “The scaling and squaring method for the matrix exponential revisited”, *SIAM Journal on Matrix Analysis and Applications*, vol. 26, no. 4, pp. 1179–1193, 2005.
- [62] I. A. Hosny and H. S. Elghawabi, “Ultrafast mri of the fetus: an increasingly important tool in prenatal diagnosis of congenital anomalies”, *Magnetic resonance imaging*, vol. 28, no. 10, pp. 1431–1439, 2010.
- [63] L. Houx, M. Lempereur, O. Rémy-Néris, and S. Brochard, “Threshold of equinus which alters biomechanical gait parameters in children”, *Gait & posture*, vol. 38, no. 4, pp. 582–589, 2013.
- [64] D. Hunter, Y. Zhang, X. Tu, M. Lavalley, J. Niu, S. Amin, A. Guermazi, H. Genant, D. Gale, and D. Felson, “Change in joint space width: hyaline articular cartilage loss or alteration in meniscus?”, *Arthritis & Rheumatism: Official Journal of the American College of Rheumatology*, vol. 54, no. 8, pp. 2488–2495, 2006.
- [65] K. Imai, K. Ikoma, M. Kido, M. Maki, H. Fujiwara, Y. Arai, R. Oda, D. Tokunaga, N. Inoue, and T. Kubo, “Joint space width of the tibiotalar joint in the healthy foot”, *Journal of Foot and Ankle Research*, vol. 8, no. 1, p. 26, 2015.

- [66] M. Jenkinson, P. Bannister, M. Brady, and S. Smith, “Improved optimization for the robust and accurate linear registration and motion correction of brain images”, *Neuroimage*, vol. 17, no. 2, pp. 825–841, 2002.
- [67] M. Jenkinson, C. F. Beckmann, T. E. Behrens, M. W. Woolrich, and S. M. Smith, “Fsl”, *Neuroimage*, vol. 62, no. 2, pp. 782–790, 2012.
- [68] L. Jones, H. Yang, T. J. Pennycook, M. S. Marshall, S. Van Aert, N. D. Browning, M. R. Castell, and P. D. Nellist, “Smart align: a new tool for robust non-rigid registration of scanning microscope data”, *Advanced Structural and Chemical Imaging*, vol. 1, no. 1, p. 8, 2015.
- [69] R. Jones, O. Haraldseth, T. Müller, P. Rinck, and A. Øksendal, “K-space substitution: a novel dynamic imaging technique”, *Magnetic resonance in medicine*, vol. 29, no. 6, pp. 830–834, 1993.
- [70] S. E. Jones, B. R. Buchbinder, and I. Aharon, “Three-dimensional mapping of cortical thickness using laplace’s equation”, *Human brain mapping*, vol. 11, no. 1, pp. 12–32, 2000.
- [71] S. Y. Joo, D. N. Knowtharapu, K. J. Rogers, L. Holmes Jr, and F. Miller, “Recurrence after surgery for equinus foot deformity in children with cerebral palsy: assessment of predisposing factors for recurrence in a long-term follow-up study”, *Journal of children’s orthopaedics*, vol. 5, no. 4, pp. 289–296, 2011.
- [72] R. M. Kay, S. A. Rethlefsen, J. A. Ryan, and T. A. Wren, “Outcome of gastrocnemius recession and tendo-achilles lengthening in ambulatory children with cerebral palsy”, *Journal of Pediatric Orthopaedics B*, vol. 13, no. 2, pp. 92–98, 2004.
- [73] P. Kedem and D. M. Scher, “Foot deformities in children with cerebral palsy”, *Current opinion in pediatrics*, vol. 27, no. 1, pp. 67–74, 2015.
- [74] A. A. Kirillov, *An introduction to Lie groups and Lie algebras*. Cambridge University Press, 2008, vol. 113.
- [75] L. Koman, B. Smith, and R. Barron, “Recurrence of equinus foot deformity in cerebral palsy patients following surgery: a review.”, *Journal of the Southern Orthopaedic Association*, vol. 12, no. 3, pp. 125–33, 2003.
- [76] S. Kralik, M. Yasrebi, N. Supakul, C. Lin, L. Netter, R. Hicks, R. Hibbard, L. Ackerman, M. Harris, and C. Ho, “Diagnostic performance of ultrafast brain mri for evaluation of abusive head trauma”, *American Journal of Neuroradiology*, vol. 38, no. 4, pp. 807–813, 2017.
- [77] S. J. Leon, I. Bica, and T. Hohn, *Linear algebra with applications*. Macmillan New York, 1980.
- [78] C. Li, X. Zhu, and C. Gu, “Matrix padé-type method for computing the matrix exponential”, *Applied Mathematics*, vol. 2, no. 02, p. 247, 2011.

- [79] G. Li, S. E. Park, L. E. DeFrate, M. E. Schutzer, L. Ji, T. J. Gill, and H. E. Rubash, “The cartilage thickness distribution in the tibiofemoral joint and its correlation with cartilage-to-cartilage contact”, *Clinical biomechanics*, vol. 20, no. 7, pp. 736–744, 2005.
- [80] G. Li, S. K. Van de Velde, and J. T. Bingham, “Validation of a non-invasive fluoroscopic imaging technique for the measurement of dynamic knee joint motion”, *Journal of biomechanics*, vol. 41, no. 7, pp. 1616–1622, 2008.
- [81] S. Li, Y. Zhu, Y. Xie, and S. Gao, “Dynamic magnetic resonance imaging method based on golden-ratio cartesian sampling and compressed sensing”, *PLoS one*, vol. 13, no. 1, e0191569, 2018.
- [82] D. Loeckx, F. Maes, D. Vandermeulen, and P. Suetens, “Nonrigid image registration using free-form deformations with a local rigidity constraint”, in *International Conference on Medical Image Computing and Computer-Assisted Intervention*, Springer, 2004, pp. 639–646.
- [83] B. Lusch, J. N. Kutz, and S. L. Brunton, “Deep learning for universal linear embeddings of nonlinear dynamics”, *Nature communications*, vol. 9, no. 1, p. 4950, 2018.
- [84] J. C. Maas, A. J. Dallmeijer, P. A. Huijing, J. E. Brunstrom-Hernandez, P. J. van Kampen, R. T. Jaspers, and J. G. Becher, “Splint: the efficacy of orthotic management in rest to prevent equinus in children with cerebral palsy, a randomised controlled trial”, *BMC pediatrics*, vol. 12, no. 1, p. 38, 2012.
- [85] D. MacDonald, N. Kabani, D. Avis, and A. C. Evans, “Automated 3-d extraction of inner and outer surfaces of cerebral cortex from mri”, *NeuroImage*, vol. 12, no. 3, pp. 340–356, 2000.
- [86] J. A. Maintz and M. A. Viergever, “A survey of medical image registration”, *Medical image analysis*, vol. 2, no. 1, pp. 1–36, 1998.
- [87] K. Makki, B. Borotikar, M. Garetier, O. Acosta, S. Brochard, D. B. Salem, and F. Rousseau, “4D in vivo quantification of ankle joint space width using dynamic mri”, in *2019 IEEE 41st International Engineering in Medicine and Biology Conference (EMBC 2019)*, IEEE, 2019.
- [88] K. Makki, B. Borotikar, M. Garetier, S. Brochard, D. B. Salem, and F. Rousseau, “High-resolution temporal reconstruction of ankle joint from dynamic mri”, in *2018 IEEE 15th International Symposium on Biomedical Imaging (ISBI 2018)*, IEEE, 2018, pp. 1297–1300.
- [89] —, “Temporal resolution enhancement of dynamic MRI sequences within a motion-based framework”, in *2019 IEEE 41st International Engineering in Medicine and Biology Conference (EMBC 2019)*, IEEE, 2019.

- [90] K. Makki, B. Borotikar, M. Garetier, S. Brochard, D. B. Salem, and F. Rousseau, “In vivo ankle joint kinematics from dynamic magnetic resonance imaging using a registration-based framework”, *Journal of Biomechanics*, 2019.
- [91] A. Makropoulos, E. C. Robinson, A. Schuh, R. Wright, S. Fitzgibbon, J. Bozek, S. J. Counsell, J. Steinweg, K. Vecchiato, J. Passerat-Palmbach, *et al.*, “The developing human connectome project: a minimal processing pipeline for neonatal cortical surface reconstruction”, *Neuroimage*, vol. 173, pp. 88–112, 2018.
- [92] M. Martín-Fernández, M. Martín-Fernández, and C. Alberola-López, “A log-euclidean polyaffine registration for articulated structures in medical images”, in *MICCAI*, Springer, 2009, pp. 156–164.
- [93] D. Metaxiotis, A. Siebel, and L. Doederlein, “Repeated botulinum toxin a injections in the treatment of spastic equinus foot.”, *Clinical Orthopaedics and Related Research (1976-2007)*, vol. 394, pp. 177–185, 2002.
- [94] M. I. Miller, A. B. Massie, J. T. Ratnanather, K. N. Botteron, and J. G. Csernansky, “Bayesian construction of geometrically based cortical thickness metrics”, *NeuroImage*, vol. 12, no. 6, pp. 676–687, 2000.
- [95] J. Modersitzki, *FAIR: flexible algorithms for image registration*. Siam, 2009, vol. 6.
- [96] —, *Numerical methods for image registration*. Oxford University Press on Demand, 2004.
- [97] A. Mohamed, C. Davatzikos, and R. Taylor, “A combined statistical and biomechanical model for estimation of intra-operative prostate deformation”, in *International Conference on Medical Image Computing and Computer-Assisted Intervention*, Springer, 2002, pp. 452–460.
- [98] A. H. Al-Mohy and N. J. Higham, “A new scaling and squaring algorithm for the matrix exponential”, *SIAM Journal on Matrix Analysis and Applications*, vol. 31, no. 3, pp. 970–989, 2009.
- [99] C. Moler and C. Van Loan, “Nineteen dubious ways to compute the exponential of a matrix”, *SIAM review*, vol. 20, no. 4, pp. 801–836, 1978.
- [100] —, “Nineteen dubious ways to compute the exponential of a matrix, twenty-five years later”, *SIAM review*, vol. 45, no. 1, pp. 3–49, 2003.
- [101] R. Mukundan, “Quaternions: from classical mechanics to computer graphics, and beyond”, in *Proceedings of the 7th Asian Technology conference in Mathematics*, 2002, (2002) 97–105.
- [102] V. Noblet, “Recalage non rigide d’images cérébrales 3D avec contrainte de conservation de la topologie”, PhD thesis, Ph. D Thesis, 2006.

- [103] V. Noblet, C. Heinrich, F. Heitz, and J.-P. Armspach, “Symmetric non-rigid image registration: application to average brain templates construction”, in *International Conference on Medical Image Computing and Computer-Assisted Intervention*, Springer, 2008, pp. 897–904.
- [104] X. Papademetris, D. Dione, L. Dobrucki, L. Staib, and A. Sinusas, “Articulated rigid registration for serial lower-limb mouse imaging”, in *MICCAI*, Springer, 2005, pp. 919–926.
- [105] T. S. Parker and L. Chua, *Practical numerical algorithms for chaotic systems*. Springer Science & Business Media, 2012.
- [106] N. J. Pelc, R. J. Herfkens, A. Shimakawa, D. R. Enzmann, *et al.*, “Phase contrast cine magnetic resonance imaging”, *Magnetic resonance quarterly*, vol. 7, no. 4, pp. 229–254, 1991.
- [107] X. Pennec, P. Cachier, and N. Ayache, “Understanding the âdemonâs algorithmâ: 3d non-rigid registration by gradient descent”, in *International Conference on Medical Image Computing and Computer-Assisted Intervention*, Springer, 1999, pp. 597–605.
- [108] J. Perry, J. M. Burnfield, J. K. Gronley, and S. J. Mulroy, “Toe walking: muscular demands at the ankle and knee”, *Archives of physical medicine and rehabilitation*, vol. 84, no. 1, pp. 7–16, 2003.
- [109] J. PERRY, M. M. HOFFER, P. GIOVAN, D. ANTONELLI, and R. GREENBERG, “Gait analysis of the triceps surae in cerebral palsy: a preoperative and postoperative clinical and electromyographic study”, *JBJS*, vol. 56, no. 3, pp. 511–520, 1974.
- [110] R. Pettigrew, “Dynamic cardiac MR imaging. Techniques and applications.”, *Radiologic Clinics of North America*, vol. 27, no. 6, pp. 1183–1203, 1989.
- [111] D. Piccini, L. Feng, G. Bonanno, S. Coppo, J. Yerly, R. P. Lim, J. Schwitter, D. K. Sodickson, R. Otazo, and M. Stuber, “Four-dimensional respiratory motion-resolved whole heart coronary mr angiography”, *Magnetic resonance in medicine*, vol. 77, no. 4, pp. 1473–1484, 2017.
- [112] F. Piludu, S. Marzi, A. Pace, V. Villani, A. Fabi, C. M. Carapella, I. Terrenato, A. Antenucci, and A. Vidiri, “Early biomarkers from dynamic contrast-enhanced magnetic resonance imaging to predict the response to antiangiogenic therapy in high-grade gliomas”, *Neuroradiology*, vol. 57, no. 12, pp. 1269–1280, 2015.
- [113] A. R. Porras, B. Paniagua, S. Ensel, R. Keating, G. F. Rogers, A. Enquobahrie, and M. G. Linguraru, “Locally affine diffeomorphic surface registration and its application to surgical planning of fronto-orbital advancement”, *IEEE transactions on medical imaging*, vol. 37, no. 7, pp. 1690–1700, 2018.

- [114] C. Qin, J. Schlemper, J. Caballero, A. N. Price, J. V. Hajnal, and D. Rueckert, “Convolutional recurrent neural networks for dynamic mr image reconstruction”, *IEEE transactions on medical imaging*, vol. 38, no. 1, pp. 280–290, 2019.
- [115] M. Rahim, M.-E. Bellemare, R. Bulot, and N. Pirró, “A diffeomorphic mapping based characterization of temporal sequences: application to the pelvic organ dynamics assessment”, *Journal of mathematical imaging and vision*, vol. 47, no. 1-2, pp. 151–164, 2013.
- [116] A. J. Reibman and F. T. Sheehan, “Precise 3D skeletal kinematics using fast phase contrast magnetic resonance imaging”, *Journal of Magnetic Resonance Imaging*, vol. 17, no. 2, pp. 206–213, 2003.
- [117] K. R. Rocha, A. J. Yezzi, and J. L. Prince, “A hybrid eulerian–lagrangian approach for thickness, correspondence, and gridding of annular tissues”, *IEEE Transactions on Image Processing*, vol. 16, no. 3, pp. 636–648, 2007.
- [118] D. Rueckert, P. Aljabar, R. A. Heckemann, J. V. Hajnal, and A. Hammers, “Diffeomorphic registration using b-splines”, in *International Conference on Medical Image Computing and Computer-Assisted Intervention*, Springer, 2006, pp. 702–709.
- [119] Y. Saad, *Iterative methods for sparse linear systems*. siam, 2003, vol. 82.
- [120] T. Schaeffter, S. Weiss, H. Eggers, and V. Rasche, “Projection reconstruction balanced fast field echo for interactive real-time cardiac imaging”, *Magnetic Resonance in Medicine: An Official Journal of the International Society for Magnetic Resonance in Medicine*, vol. 46, no. 6, pp. 1238–1241, 2001.
- [121] H.-P. Schröcker, “From a to b: new methods to interpolate two poses”, *arXiv preprint arXiv:1706.04539*, 2017.
- [122] C. Seiler, X. Pennec, and M. Reyes, “Capturing the multiscale anatomical shape variability with polyaffine transformation trees”, *Medical Image Analysis*, vol. 16, no. 7, pp. 1371–1384, 2012.
- [123] L. M. Shapiro and G. E. Gold, “Mri of weight bearing and movement”, *Osteoarthritis and cartilage*, vol. 20, no. 2, pp. 69–78, 2012.
- [124] F. T. Sheehan, “The 3D in vivo Achille’s tendon moment arm, quantified during active muscle control and compared across sexes”, *Journal of biomechanics*, vol. 45, no. 2, pp. 225–230, 2012.
- [125] —, “The instantaneous helical axis of the subtalar and talocrural joints: a non-invasive in vivo dynamic study”, *Journal of foot and ankle research*, vol. 3, no. 1, p. 13, 2010.
- [126] F. T. Sheehan, A. Babushkina, and K. E. Alter, “Kinematic determinants of anterior knee pain in cerebral palsy: a case-control study”, *Archives of physical medicine and rehabilitation*, vol. 93, no. 8, pp. 1431–1440, 2012.

- [127] F. T. Sheehan and J. E. Drace, “Quantitative MR measures of three-dimensional patellar kinematics as a research and diagnostic tool.”, *Medicine and science in sports and exercise*, vol. 31, no. 10, pp. 1399–1405, 1999.
- [128] F. T. Sheehan, A. R. Seisler, and K. E. Alter, “Three-dimensional in vivo quantification of knee kinematics in cerebral palsy”, *Clinical orthopaedics and related research*, vol. 466, no. 2, pp. 450–458, 2008.
- [129] F. T. Sheehan, A. R. Seisler, and K. L. Siegel, “In vivo talocrural and subtalar kinematics: a non-invasive 3d dynamic mri study”, *Foot & ankle international*, vol. 28, no. 3, pp. 323–335, 2007.
- [130] F. T. Sheehan and R. M. Smith, “3D musculoskeletal kinematics using dynamic MRI”, *Handbook of Human Motion*, pp. 1–17, 2017.
- [131] F. T. Sheehan, F. E. Zajac, and J. E. Drace, “Using cine phase contrast magnetic resonance imaging to non-invasively study in vivo knee dynamics”, *Journal of biomechanics*, vol. 31, no. 1, pp. 21–26, 1997.
- [132] B. J. Shore, N. White, and H. Kerr Graham, “Surgical correction of equinus deformity in children with cerebral palsy: a systematic review”, *Journal of children’s orthopaedics*, vol. 4, no. 4, pp. 277–290, 2010.
- [133] A. Sotiras, C. Davatzikos, and N. Paragios, “Deformable medical image registration: a survey”, *IEEE transactions on medical imaging*, vol. 32, no. 7, p. 1153, 2013.
- [134] C. Stehning, P. Börnert, K. Nehrke, H. Eggers, and O. Dössel, “Fast isotropic volumetric coronary MR angiography using free-breathing 3D radial balanced FFE acquisition”, *Magnetic Resonance in Medicine: An Official Journal of the International Society for Magnetic Resonance in Medicine*, vol. 52, no. 1, pp. 197–203, 2004.
- [135] W. B. Strecker, M. W. Via, S. K. Oliver, and P. L. Schoenecker, “Heel cord advancement for treatment of equinus deformity in cerebral palsy.”, *Journal of pediatric orthopedics*, vol. 10, no. 1, pp. 105–108, 1990.
- [136] S. Tang, Y. Fan, G. Wu, M. Kim, and D. Shen, “Rabbit: rapid alignment of brains by building intermediate templates”, *NeuroImage*, vol. 47, no. 4, pp. 1277–1287, 2009.
- [137] P. A. G. Teixeira, A. Gervaise, M. Louis, A. Raymond, A.-S. Formery, S. Lecocq, and A. Blum, “Musculoskeletal wide-detector ct kinematic evaluation: from motion to image”, in *Seminars in musculoskeletal radiology*, Thieme Medical Publishers, vol. 19, 2015, pp. 456–462.
- [138] C. Tor-Díez, N. Passat, I. Bloch, S. Faisan, N. Bednarek, and F. Rousseau, “An iterative multi-atlas patch-based approach for cortex segmentation from neonatal mri”, *Computerized Medical Imaging and Graphics*, vol. 70, pp. 73–82, 2018.

- [139] J. Tsao, P. Boesiger, and K. P. Pruessmann, “K-t BLAST and k-t SENSE: dynamic MRI with high frame rate exploiting spatiotemporal correlations”, *Magnetic resonance in medicine*, vol. 50, no. 5, pp. 1031–1042, 2003.
- [140] R. Vemulapalli, F. Arrate, and R. Chellappa, “Human action recognition by representing 3d skeletons as points in a lie group”, in *Proceedings of the IEEE conference on computer vision and pattern recognition*, 2014, pp. 588–595.
- [141] M. F. Vignos, J. M. Kaiser, G. S. Baer, R. Kijowski, and D. G. Thelen, “American society of biomechanics clinical biomechanics award 2017: non-anatomic graft geometry is linked with asymmetric tibiofemoral kinematics and cartilage contact following anterior cruciate ligament reconstruction”, *Clinical Biomechanics*, vol. 56, pp. 75–83, 2018.
- [142] L. Wan, R. J. de Asla, H. E. Rubash, and G. Li, “In vivo cartilage contact deformation of human ankle joints under full body weight”, *Journal of orthopaedic research*, vol. 26, no. 8, pp. 1081–1089, 2008.
- [143] G. Wu, S. Siegler, P. Allard, C. Kirtley, A. Leardini, D. Rosenbaum, M. Whittle, D. D DâLima, L. Cristofolini, H. Witte, *et al.*, “ISB recommendation on definitions of joint coordinate system of various joints for the reporting of human joint motionâpart i: ankle, hip, and spine”, *Journal of biomechanics*, vol. 35, no. 4, pp. 543–548, 2002.
- [144] X. Yang, Z. Xue, X. Liu, and D. Xiong, “Topology preservation evaluation of compact-support radial basis functions for image registration”, *Pattern Recognition Letters*, vol. 32, no. 8, pp. 1162–1177, 2011.
- [145] A. J. Yezzi and J. L. Prince, “An eulerian pde approach for computing tissue thickness”, *IEEE transactions on medical imaging*, vol. 22, no. 10, pp. 1332–1339, 2003.
- [146] M. Zefran and V. Kumar, “Planning of smooth motions on  $se(3)$ ”, in *Proceedings of IEEE International Conference on Robotics and Automation*, IEEE, vol. 1, 1996, pp. 121–126.
- [147] ———, “Two methods for interpolating rigid body motions”, in *Proceedings. 1998 IEEE International Conference on Robotics and Automation (Cat. No. 98CH36146)*, IEEE, vol. 4, 1998, pp. 2922–2927.
- [148] M. Zefran, V. Kumar, and C. Croke, “Choice of riemannian metrics for rigid body kinematics”, in *ASME 24th Biennial Mechanisms Conference*, vol. 2, 1996.
- [149] T. Zhang, B. Fang, Y. Y. Tang, Z. Shang, and B. Xu, “Generalized discriminant analysis: a matrix exponential approach”, *IEEE Transactions on Systems, Man, and Cybernetics, Part B (Cybernetics)*, vol. 40, no. 1, pp. 186–197, 2009.

- 
- [150] Y. Zhu and N. J. Pelc, “Three-dimensional motion tracking with volumetric phase contrast MR velocity imaging”, *Journal of Magnetic Resonance Imaging: An Official Journal of the International Society for Magnetic Resonance in Medicine*, vol. 9, no. 1, pp. 111–118, 1999.
- [151] J. Zimmermann, R. Goebel, F. De Martino, P.-F. Van de Moortele, D. Feinberg, G. Adriany, D. Chaimow, A. Shmuel, K. Uğurbil, and E. Yacoub, “Mapping the organization of axis of motion selective features in human area mt using high-field fmri”, *PloS one*, vol. 6, no. 12, e28716, 2011.



---

**Analysis of the kinematic motion of the ankle from 4D magnetic  
resonance imaging**

**Abstract:**

Cerebral Palsy (CP) is a common birth pathology in children leading to ankle joint deformity, also known as the Spastic Equinus (SE) deformity, and thus leads to abnormal function of the joint. While the management of ankle disorders focuses on restoring the joint functions, the underlying pathomechanics is not clearly understood yet. To better understand the biomechanics of the pediatric ankle joint, it is crucial to establish *in vivo* normative joint biomechanics before focusing on pathomechanics studies. Dynamic MRI has made it possible to non-invasively capture the ankle joint during a complete motion cycle. However, dynamic MRI comes with its own set of unique challenges such as low resolution, anisotropy, and motion artifacts. This motivates our choice for combining spatial information of conventional static MRI with temporal information of dynamic MRI sequences. The global aim of this research work is to build computational frameworks and to develop robust intensity-based approaches for estimating the joint motion and deformations from 3D+t MRI data, and thus for deriving the joint kinematics and the joint contact mechanics during a single cycle of dorsi-plantarflexion. Due to a lack of sufficient imaging data in the pediatric cohort, the proposed algorithms are applied on dynamic MRI data (portraying both passive and active ankle motions) from 6 healthy children.

**Keywords:**

Dynamic MRI, motion estimation, motion interpolation, contact mechanics, PDE(s), diffeomorphic registration, intensity-based registration.

**Résumé:**

La paralysie cérébrale (PC) est la première cause de l'handicap moteur de l'enfant en France (2 naissances pour 1000). Il s'agit d'une pathologie causée par des atteintes non progressives survenues lors du développement du cerveau chez le fœtus ou le nourrisson. L'équin de la cheville est la déformation musculo-squelettique la plus fréquente chez les enfants atteints par la PC. Malgré des thérapies médico-chirurgicales multiples, le taux de récurrence post-opératoire demeure très élevé (48%). Une des principales raisons des échecs des thérapies est le manque de connaissance de la biomécanique articulaire et musculaire. Les techniques d'imagerie en IRM dynamique permettent aujourd'hui d'explorer l'appareil musculosquelettique au cours du mouvement dans les 3 dimensions de l'espace avec une grande précision (<1mm). Cependant, ces techniques viennent avec leur propre liste de problèmes tels que la résolution réduite, l'anisotropie et les artefacts de mouvement. Dans cette thèse, nous abordons ces problèmes en combinant l'information spatiale de l'IRM conventionnel avec l'information temporelle fournie par les séquences IRM dynamique. Nous avons réussi à atteindre l'objectif principal de ces travaux de recherche en développant des algorithmes robustes combinant des aspects informatiques et mathématiques (dont le recalage d'images basé sur l'intensité était le facteur clé) qui nous ont permis de reconstruire les mouvements articulaires et donc d'établir une analyse biomécanique de la cheville en plus de la reconstruction spatio-temporelle de la séquence dynamique en utilisant une approche log-euclidienne. Les algorithmes proposés ont

# Résumé étendu

---

---

## Résumé

La paralysie cérébrale (PC) est la première cause de l'handicap moteur de l'enfant en France (2 naissances pour 1000). Il s'agit d'une pathologie causée par des atteintes non progressives survenues lors du développement du cerveau chez le fœtus ou le nourrisson. L'équin de la cheville est la déformation musculo-squelettique la plus fréquente chez les enfants atteints par la PC. Malgré des thérapies médico-chirurgicales multiples, le taux de récurrence post-opératoire demeure très élevé (48%). Une des principales raisons des échecs des thérapies est le manque de connaissance de la biomécanique articulaire et musculaire. Les techniques d'imagerie en IRM dynamique permettent aujourd'hui d'explorer l'appareil musculosquelettique au cours du mouvement dans les 3 dimensions de l'espace avec une grande précision ( $< 1mm$ ). Cependant, ces techniques viennent avec leur propre liste de problèmes tels que la résolution réduite, l'anisotropie et les artefacts de mouvement. Dans cette thèse, nous abordons ces problèmes en combinant l'information spatiale de l'IRM conventionnel avec l'information temporelle fournie par les séquences IRM dynamique. Nous avons réussi à atteindre l'objectif principal de ces travaux de recherche en développant des algorithmes robustes combinant des aspects informatiques et mathématiques (dont le recalage d'images basé sur l'intensité était le facteur clé) qui nous ont permis de reconstruire les mouvements articulaires et donc d'établir une analyse biomécanique de la cheville en plus de la reconstruction spatio-temporelle de la séquence dynamique en utilisant une approche log-euclidienne. Les algorithmes proposés ont été appliqués sur la base de données actuellement disponible (contenant 6 sujets normaux) et devraient être également appliqués sur une base plus large contenant des sujets pathologiques de la même tranche d'âges afin de comparer les deux populations et de caractériser la pathologie.

**Mots-clés :** IRM dynamique, estimation de mouvement, interpolation de mouvement, biomécanique du cartilage articulaire, équations aux dérivées partielles EDP(s), recalage difféomorphique, recalage basé-intensité.

## 1. Description générale

Ce travail est une contribution à l'étude de l'appareil musculo-squelettique en mouvement et prend son origine clinique dans le traitement de l'équin de cheville chez les enfants entre 7 et 14 ans. Le manque de consensus sur le traitement de ces pathologies et les échecs relativement fréquents des traitements sont dus dans une large mesure au manque de connaissances sur la biomécanique articulaire et musculaire de l'articulation lésée.

Face à une pathologie dynamique, il est essentiel de comprendre l'effet in vivo de la faiblesse des muscles de la cheville sur les paramètres biomécaniques articulaires et sur la déformation osseuse qui en résulte. Cependant, cela n'a pas été fait à ce jour dans la littérature.

Les travaux proposés dans cette thèse visent donc à développer l'usage de l'IRM dynamique, connue comme technique non-invasive, pour l'étude de la cheville en particulier, et plus généralement de l'appareil musculo-squelettique en mouvement, et à fournir des outils permettant l'analyse spatio-temporelle de ces données.

Ce rapport, écrit en anglais, se présente sous la forme d'un document de plus d'une centaine de pages organisé en quatre chapitres décrits par la suite.

## 2. Acquisition de données IRM

Toutes les acquisitions IRM ont été faites au CHRU de Brest (centre de radiologie de la cavale blanche). L'enregistrement IRM(3T Philips Achieva scanner) est composé d'un premier temps dynamique, et d'un second temps statique, selon un protocole identique pour les deux cohortes (sains et pathologiques). Le côté étudié correspond au côté non dominant pour l'enfant sain, et au côté pathologique pour l'enfant avec équin. Concernant la première partie, dynamique, le sujet est placé en décubitus dorsal dans l'IRM, avec la cheville placée dans une orthèse en plastique articulée spécialement conçue pour l'étude et IRM compatible. Deux antennes circulaires de détection en réseau phasé (dS Flex M, Philips Achieva) sont placées de part et d'autre de l'orthèse de cheville. Le genou est en extension complète et l'arrière pied est en position neutre dans le plan frontal. Cette orthèse permet des mouvements passifs, à l'aide de cordelettes tirées par l'examineur, puis des mouvements actifs de flexions plantaire et dorsale. Le sujet effectue donc des séquences de mouvements passifs, puis de mouvements actifs. Tous les mouvements sont standardisés, partant de la position de flexion plantaire maximale, puis un

mouvement de flexion dorsale lent et régulier pendant 9 secondes jusqu'à atteindre la position de flexion dorsale maximale, avant de revenir sans arrêt vers la position initiale de flexion plantaire maximale en 9 secondes. Concernant la partie passive, les cordelettes de l'orthèse sont tirées alternativement pour chaque mouvement, dans une direction strictement parallèle à celle de l'orthèse et avec la même force de traction afin de minimiser les différences entre les mouvements et les sujets, et d'homogénéiser la direction des forces extérieures s'appliquant au pied en mouvement. Concernant la partie active, le temps est décompté auprès de l'enfant, lui permettant de réaliser un mouvement suffisamment ample et progressif pour réduire les artefacts d'acquisition.

### 3. Chapitre introductif

Un premier chapitre introductif regroupe un ensemble d'éléments cliniques, bibliographiques et méthodologiques. Le contexte clinique des travaux est d'abord présenté avec des rappels anatomiques sur l'articulation de la cheville et une revue des traitements actuels de l'équin de cheville. Cette étude met en évidence le manque de consensus sur les traitements à mener en raison notamment d'un déficit de connaissances fonctionnelles sur l'articulation en mouvement. Une revue des méthodes permettant l'acquisition de données IRM dynamique est ensuite proposée.

Si les méthodes utilisant l'acquisition basée sur la répétition d'un grand nombre de cycles de mouvement sont exclues dans le cas de la cheville dans un contexte pédiatrique, les séquences de type T1 fast field echo (FFE) peuvent être utilisées mais présentent toutefois une résolution faible avec la présence d'artefacts de mouvement. L'objectif de cette thèse est donc d'utiliser d'une part une image statique à très haute résolution, et d'autre part des séquences IRM dynamiques, pour obtenir une reconstruction spatio-temporelle haute résolution permettant de quantifier *in vivo* la biomécanique de la cheville par des méthodes de suivi. A ce jour et à notre connaissance, on est les premiers à produire cette reconstruction haute résolution des séquences IRM dynamiques.

Un état de l'art sur le recalage est ensuite proposé. Le fait d'avoir des structures rigides et des structures molles dans l'articulation nous a amené à privilégier un recalage de type poly-rigide fusionnant de multiples transformations rigide correspondant à chaque os.

Ce schéma polyrigide, initialement défini par Arsigny en 2006 [1], vise à définir une transformation inversible avec un comportement rigide local. Ceci va permettre d'estimer un champ dense de déformation de l'articulation avec les propriétés d'un difféomorphisme tels que l'inversibilité et la différentiabilité. Plutôt que de moyenniser les déplacements, ce qui conduit généralement à une transformation non-inversible, l'idée de la méthode Log Euclidienne est de moyenniser le champ de vitesse, construit à partir du logarithme des transformations, la solution globale fusionnant les diverses composantes étant obtenue par résolution d'une équation différentielle ordinaire (EDO). De plus, la solution d'une EDO permet d'estimer une trajectoire lisse et continue de chaque os et puis de toute l'articulation dans l'espace tangent (le champ de vitesse). En d'autres, il s'agit d'une approche paramétrique (dont le temps est le paramètre) qui permet à la fois de suivre l'évolution temporelle d'un système articulaire et de réduire le nombre de paramètres géométriques nécessaires pour l'estimation des transformations non-rigides. La fin du chapitre introductif est consacrée à la description de méthodes mathématiques intervenant dans la méthode Log-Euclidienne (équations différentielles ordinaires, logarithme et exponentielle des matrices, etc...).

#### **4. Contribution biomécanique à l'analyse cinématique in vivo des mouvements de la cheville**

Le second chapitre propose une méthode pour mesurer la cinématique de l'articulation de la cheville en combinant l'information spatiale d'une acquisition statique haute résolution avec l'information temporelle de la séquence dynamique. Ceci a permis de suivre le mouvement de tout l'os au lieu de suivre des points sur ses contours [2], dont la reproductibilité n'est pas nécessairement garantie vu les variations morphologiques des formes osseuses d'un sujet à l'autre. La méthode que nous proposons nécessite le détournement de trois os dans l'IRM haute résolution (calcaneus, talus, et tibia), comme initialisation. La segmentation est ensuite propagée dans les images basse résolution, d'abord via un recalage rigide global, puis par un recalage rigide propre à chaque os en utilisant les segmentations pour contraindre l'optimisation de la fonction coût durant le processus de recalage. Les déplacements relatifs rigides de chaque os dans la séquence temporelle en sont ensuite déduits. Le choix automatique d'une image de référence la plus proche de l'image statique comme point de départ de la propagation dans la séquence dynamique permet a priori de diminuer les erreurs de recalage. En effet, un algorithme

de recalage est basé sur un processus d'optimisation qui converge plus facilement pour des transformations géométriques qui sont proches de l'*identité*. Dans un second temps, un champ dense de déformation est calculé entre l'IRM statique et chaque image basse résolution en fusionnant les transformations rigides des os grâce à la méthode Log Euclidienne, permettant ainsi d'estimer des déformations non-rigides de la cheville.

La méthode a été évaluée sur 6 patients sains avec des mouvements passifs ou actifs. Les évaluations portent essentiellement sur la cinématique 3D de chacun des 3 os. La précision des transformations rigides est évaluée sur la base d'un détournage manuel des os dans la séquence dynamique et mesurée via le coefficient de DICE (mesurant le recouvrement entre masques binaires), et l'erreur RMSE sur les contours. Ces résultats montrent un recalage satisfaisant avec un coefficient de DICE 3D supérieur à 0.8 et une erreur RMSE inférieure à 0.6 voxels. L'utilisation de la diagonalisation de la matrice de transformation dans les calculs des exponentielles, en lieu et place de la méthode *scaling and squaring* est mise en avant dans le document à la fois pour accélérer le calcul et en améliorer la précision avec les moindres coûts.

## **5. Estimation d'une trajectoire continue de l'articulation à partir d'une séquence discrète d'images IRM**

Le troisième chapitre a pour objectif d'améliorer la résolution temporelle de la séquence dynamique via la conception d'un algorithme Log-Euclidien polyrigide spatio-temporel fonctionnant en mode hors ligne. Ici encore, les os sont traités indépendamment et la transformation globale est obtenue ensuite par fusion. Deux méthodes d'interpolation des déplacements rigides sont proposées, toutes les deux basées sur une représentation exponentielle des rotations, celle retenue garantie une complexité moindre.

La pondération permettant la fusion est usuellement définie comme une fonction inversement proportionnelle à la distance entre chaque voxel et l'os. Le choix de ces fonctions est connu pour avoir un impact notable sur la transformation globale, obtenue après fusion. Une nouvelle fonction est proposée dans ce travail avec l'idée d'avoir des fonctions plus piquées lorsque plusieurs os sont présents au voisinage d'un point d'une part, et de favoriser l'impact direct de la transformation de l'os sur son voisinage quand on s'éloigne des

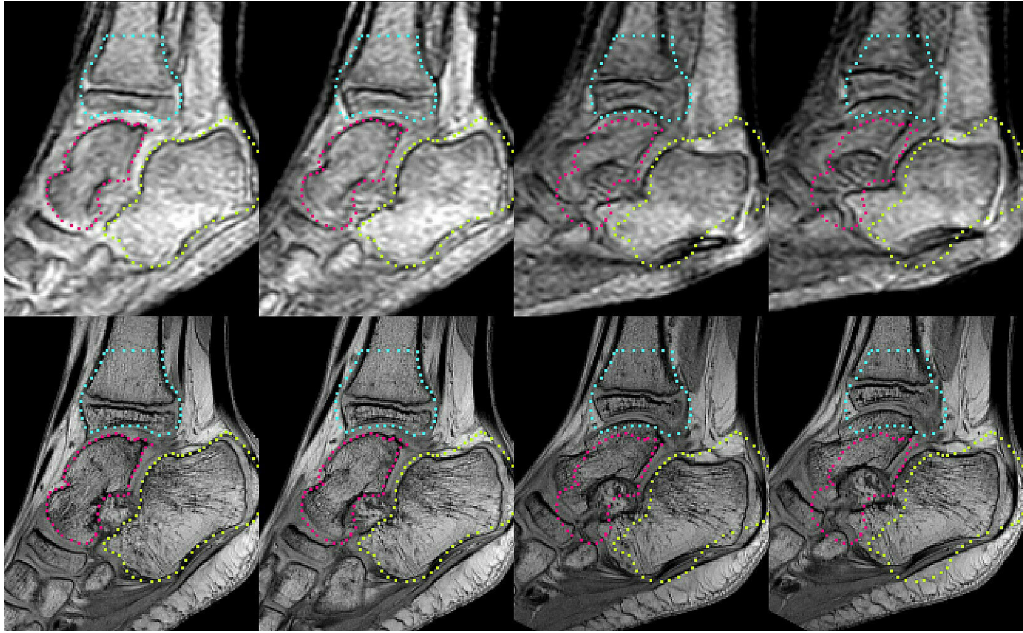


FIGURE 1: Reconstruction haute résolution de la cheville pour un sujet (sujet 6 : mouvement passif). Première ligne : images dynamiques acquises, Deuxième ligne : les reconstructions correspondantes, sous-échantillonnées à la résolution basse des images dynamiques afin de valider la précision de la reconstruction. Chaque colonne correspond à une image dans la séquence. Les contours ont été détournés manuellement sur la première image de la séquence pour montrer à la fois la précision de reconstruction (première colonne), et le mouvement en fonction du temps (colonnes de 2 à 4).

régions articulaires d'autre part, soit donc d'obtenir un comportement physiquement plausible en dehors de la squelette. La méthode est validée par exemple sur le suivi des mouvements du tendon d'Achille ainsi que par une méthode de validation croisée visant à reconstruire chacune des images acquises par interpolation des images l'encadrants. Ces nouvelles fonctions de pondération améliorent fortement les le recalage par rapport aux poids classiques.

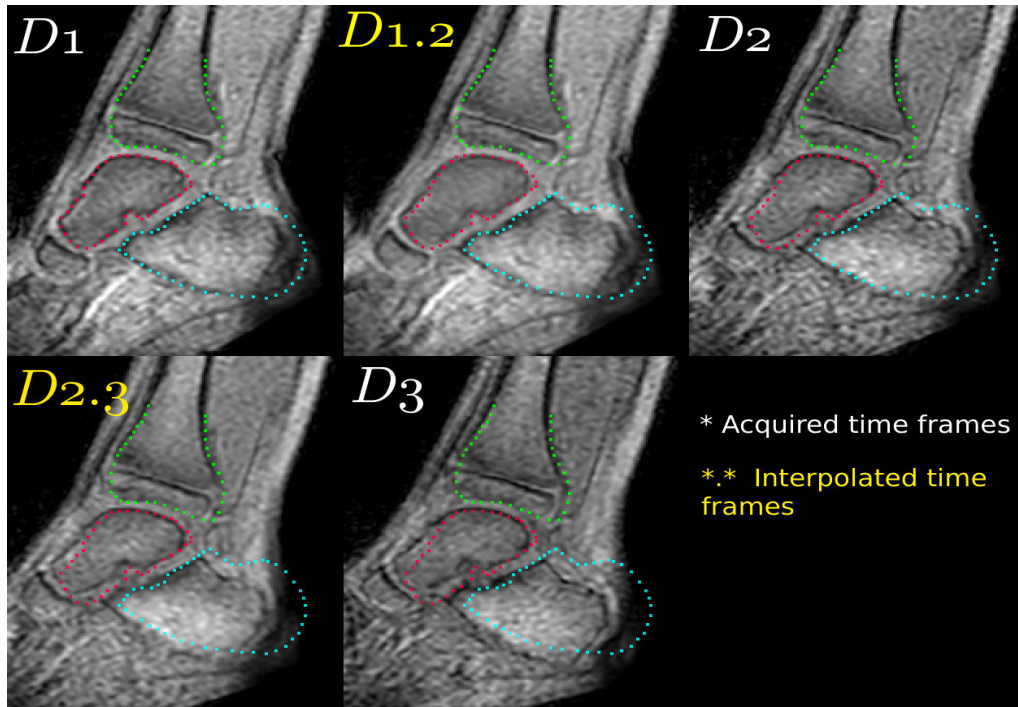


FIGURE 2: Amélioration de la résolution temporelle d’une séquence IRM dynamique en utilisant l’interpolation temporelle basée sur la diagonalisation des matrices de transformations. Les images acquises  $\{D_k\}$  sont indexées en blanc tandis que les images interpolées sont indexées en jaune  $\{D_{k.k+1}\}$ .

## 6. Quantification de l’inconfort articulaire lors du mouvement de la cheville

Le chapitre 4 aborde le problème de l’évaluation spatio-temporelle de la largeur de l’interligne articulaire et donc de quantifier la mécanique de contact pendant un cycle de mouvement continu. En permettant d’identifier les phases critiques d’un cycle de mouvement. L’automatisation de ce processus aurait un impact clinique important pour le traitement des maladies dégénératives du cartilage pour évaluer l’impact des déformations musculo-squelettiques sur les cartilages. Aucune correspondance ne pouvant être établie entre deux surfaces lisses et exposées à des fortes déformations durant le mouvement, le calcul de l’épaisseur s’appuie assez classiquement sur un schéma Eulérien maintenant éprouvé visant à déterminer des trajectoires de corres-

pondance solutions de l'équation Laplacienne, l'épaisseur étant définie comme la somme de largeur des deux trajectoires [3]. Cette technique est utilisée pour calculer la largeur de l'interligne tibio-talienne (surface 3D entre tibia et talus). Les mesures étant effectuées sur les images dynamiques haute résolution produites à l'issue du chapitre 2. Les carilages subissent des une déformation non-linéaire durant le mouvement, le suivi de l'espace articulaire utilise la méthode diffeomorphique Log Euclidienne. Pour valider les résultats de ce chapitre, une confrontation est réalisée entre les segmentation produites automatiquement avec l'espace intra-articulaire segmenté à la main sur chaque image dans la séquence dynamique, avec un indice de recouvrement de l'ordre de 0.9.

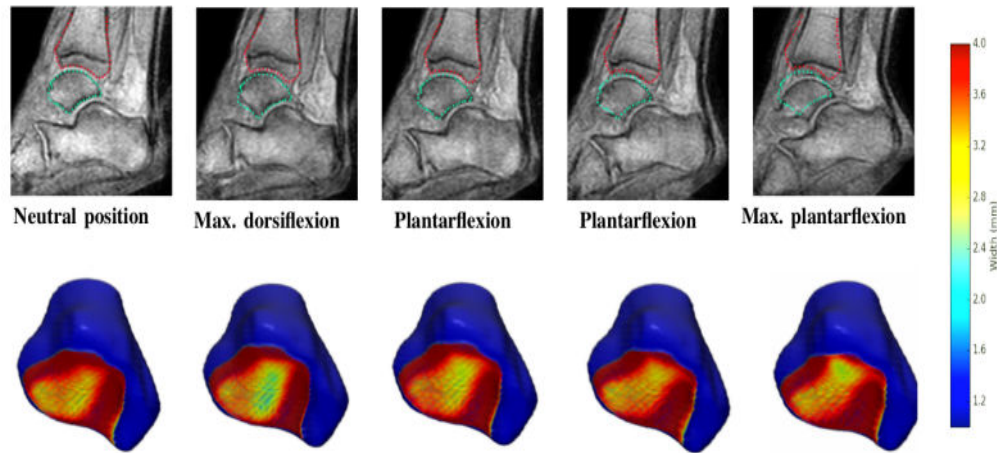


FIGURE 3: Évaluation spatio-temporelle (4D) de la largeur de l'interligne articulaire. Première ligne : images IRM anatomiques. Deuxième ligne : Les valeurs de la largeur de l'interligne articulaire projetées sur la surface de contact du tibia.

## 7. Conclusion

Cette thèse propose un ensemble de méthodes visant à étendre les techniques d'IRM pour permettre l'analyse dynamique de la cheville et plus généralement de l'appareil musculo-squelettique en mouvement. Ce travail développe des méthodes de vision par ordinateur couplant IRM conventionnelle (statique) et séquences dynamiques utilisées en clinique pour obtenir

des séquences haute résolution et les utiliser pour la détermination de caractéristiques dynamiques de l'articulation. L'obtention de caractéristiques temporelles est un des points forts de cette thèse tout comme l'est la volonté de mettre oeuvre des procédés d'acquisition minimisant les contraintes pour le patient, en ne nécessitant aucune répétition de mouvement. L'obtention automatisée de ces indicateurs dynamiques va impacter sans aucune doute dans le futur la compréhension, le diagnostic et le traitement des déformations musculo-squelettiques. Des travaux supplémentaires de validation sont évidemment nécessaires, notamment sur des sujets pathologiques non intégrés dans cette étude, afin de mieux cerner le potentiel de ces travaux. Finalement, l'objectif clinique de ses travaux consiste à améliorer la fonctionnalité de l'articulation par rééducation ou correction chirurgicale avec prédiction du résultat moteur à partir de ces nouvelles informations 3D+t.

## Références

- [1] V. Arsigny, O. Commowick, X. Pennec, N. Ayache, A log-euclidean framework for statistics on diffeomorphisms, in : International Conference on Medical Image Computing and Computer-Assisted Intervention, Springer, 2006, pp. 924–931.
- [2] F. T. Sheehan, A. R. Seisler, K. L. Siegel, In vivo talocrural and subtalar kinematics : a non-invasive 3d dynamic mri study, *Foot & ankle international* 28 (2007) 323–335.
- [3] A. J. Yezzi, J. L. Prince, An eulerian pde approach for computing tissue thickness, *IEEE transactions on medical imaging* 22 (2003) 1332–1339.

**Titre :** Développement de l'IRM dynamique pour l'étude de l'appareil musculo-squelettique en mouvement.

**Mots clés :** IRM dynamique, recalage basé intensité, estimation de mouvement, interpolation de mouvement, mécanique des contacts, biomécanique de la cheville.

**Résumé :** La paralysie cérébrale (PC) est la première cause de l'handicap moteur de l'enfant en France (2 naissances pour 1000). Il s'agit d'une pathologie causée par des atteintes non progressives survenues lors du développement du cerveau chez le fœtus ou le nourrisson. L'équin de la cheville est la déformation musculo-squelettique la plus fréquente chez les enfants atteints par la PC. Malgré des thérapies médico-chirurgicales multiples, le taux de récurrence post-opératoire demeure très élevé (48%). Une des principales raisons des échecs des thérapies est le manque de connaissance de la biomécanique articulaire et musculaire. Les techniques d'imagerie en IRM dynamique permettent aujourd'hui d'explorer l'appareil musculo-squelettique au cours du mouvement dans les 3 dimensions de l'espace avec une grande précision (<1mm). Cependant, ces techniques viennent avec leur propre liste de problèmes tels que la résolution réduite, l'anisotropie et les artefacts de mouvement.

Dans cette thèse, nous abordons ces problèmes en combinant l'information spatiale de l'IRM conventionnel avec l'information temporelle fournie par les séquences IRM dynamique. Nous avons réussi à atteindre l'objectif principal de ces travaux de recherche en développant des algorithmes robustes combinant des aspects informatiques et mathématiques (dont le recalage d'images basé sur l'intensité était le facteur clé) qui nous ont permis de reconstruire les mouvements articulaires et donc d'établir une analyse biomécanique de la cheville en plus de la reconstruction spatio-temporelle de la séquence dynamique en utilisant une approche log-euclidienne. Les algorithmes proposés ont été appliqués sur la base de données actuellement disponible (contenant 6 sujets normaux) et devraient être également appliqués sur une base plus large contenant des sujets pathologiques de la même tranche d'âges afin de comparer les deux populations et de caractériser la pathologie.

**Title :** Development of dynamic MRI to study the musculoskeletal system during motion.

**Keywords :** Dynamic MRI, intensity-based registration, motion estimation, motion interpolation, contact mechanics, ankle biomechanics.

**Abstract :** Cerebral Palsy (CP) is a common birth pathology in children leading to ankle joint deformity, also known as the Spastic Equinus (SE) deformity, which causes abnormal function of the joint. While the management of ankle disorders focuses on restoring the joint functions, the underlying pathomechanics is not clearly understood yet. To better understand the biomechanics of the pediatric ankle joint, it is crucial to establish *in vivo* normative joint biomechanics before focusing on pathomechanics studies. Dynamic MRI has made it possible to non-invasively capture the ankle joint during a complete motion cycle. However, dynamic MRI comes with its own set of unique challenges such as low resolution, anisotropy, and motion artifacts.

This motivates our choice for combining spatial information of conventional static MRI with temporal information of dynamic MRI sequences. The global aim of this research work is to build computational frameworks and to develop robust intensity-based approaches for estimating the joint motion and deformations from 3D+t MRI data, and thus for deriving the joint kinematics and the joint contact mechanics during a single cycle of dorsiflexion-plantarflexion. Due to a lack of sufficient imaging data in the pediatric cohort, the proposed algorithms are applied on dynamic MRI data (portraying both passive and active ankle motions) from 6 healthy children.